Network Optimisation for Robotic Aerial Base Stations

Liao, Yuan

Awarding institution:
King's College London

Network Optimisation for Robotic Aerial Base Stations

Yuan Liao

Centre for Telecommunication Research
Department of Engineering
King's College London

This dissertation is submitted for the degree of
Doctor of Philosophy

March 2024

Acknowledgements

As I embark on writing this thesis, I am filled with a sense of nostalgia, as if my PhD journey had just begun yesterday, and yet, it also feels like an eternity has passed. I am profoundly grateful for the opportunity to express my sincere appreciation to the individuals who have generously supported and brought joy to my life throughout these past few years.

I am deeply indebted to my supervisor, Dr. Vasilis Friderikos, whose guidance not only resulted in numerous published papers but, more importantly, transformed me into a capable and proficient researcher. His influence transcends the realm of my PhD degree, extending into every facet of my future endeavours. I would also like to express my sincere appreciation to another esteemed supervisor, Prof. Halim Yanikomeroglu, from Carleton University, Canada, whose mentorship broadened my research horizons, encompassing a trajectory that spans decades to come. Furthermore, I extend my heartfelt thanks to several researchers who graciously offered invaluable suggestions during my PhD journey: Dr. Yansha Deng, Dr. Simon Saunders, Prof. Zoran Cvetkovic, and Prof. Mohammad Shikh-Bahaei. I would like to express my sincere gratitude to my examiners, Prof. Pei Xiao and Prof. Yue Chen, for organising my PhD viva and providing numerous insightful feedback.

I wish to express my thanks to all my colleagues in the Centre for Telecommunications Research, Dr. Jongyul Lee, Wen Shang, Yijing Ren, Dadi Bi and Jingxin Li. I sincerely thank for the inspiring discussions and I will never forget the time we spent together in the Strand Building. I would also thank my close friends Zhouyue Xia, Jiaxin Gao, Kaihong Wang, Jiwei Li, Yibing Wang and Lina Wu. Wherever I will be in the future, their lovely smiling faces will be present in all my memories of London, along with countless nights accompanied by unforgettable food and beer.

I want to thank my dearest Ran Mao. Her forever lovely smile is the most precious jewel in my life. I would like also to give special thanks to my parents Hongtao Liao and Mingjuan Guo. Their unconditional gave me the greatest support to complete my PhD studies. I am also grateful to my grandparents and all my relatives who have cared for me and supported my academic pursuits.

Abstract

One attractive application of unmanned aerial vehicles (UAVs) is to provide wireless coverage when acting as aerial base stations (ABSs). Compared to terrestrial small cells, ABSs have the benefit of flexible deployment, controllable mobility, and dominant line-of-sight channels, so they are expected to play a significant role in next-generation cellular networks. However, introducing this novel non-terrestrial communication device would also bring new challenges, such as requiring different evaluation criteria and being restricted by unexpected resource constraints. With this in mind, this thesis mainly focuses on the network optimisation problems of ABS-assisted networks.

Specifically, we first investigate two contradictory metrics, i.e., the information freshness and energy consumption, when an ABS is employed to collect data from ground terminals. A novel multi-return-allowed serving mode is proposed to explore the Pareto optimal trade-off between these two metrics. Secondly, to overcome the functional endurance issue of conventional ABSs, we propose a novel prototype named robotic aerial base stations (RABSs) with grasping capabilities, which can attach autonomously in lampposts or land on other tall urban landforms to serve as small cells with prolonged endurance. By employing this novel ABS prototype, we first study the optimal deployment and operation strategy for RABSs when the mobile traffic demand shows heterogeneity in both spatial and temporal domains. Afterwards, to further explore the use of RABSs in the upcoming 6G era, we investigate two novel application scenarios, that is, an RABS-assisted integrated sensing and communication (ISAC) system and an RABS-aided millimetre-wave (mmWave) backhaul network.

The proposed scenarios are formulated as various non-convex problems. By analyzing their constructions, we propose a variety of algorithms to solve them in a reasonable time. A wide set of simulation results shows that the proposed novel prototypes and serving schemes have immense potential in future cellular networks.

Table of Contents

List of Figures

List of Tables

Acronyms

6G 6th Generation

ABS Aerial Base Station

AoI Age of Information

B5G Beyond 5th Generation

BPO Binary Polynomial Optimization

BS Base Station

CAPEX Capital Expenditure

CNN Convolutional Neural Network

DP Dynamic Programming

FSO Free Space Optics

GNSS Global Navigation Satellite System

GT Game Theory

HAPS High Altitude Platform Station

HetNet Heterogeneous Network

IAB Integrated Access and Backhaul

ILP Integer Linear Programming

IoT Internet of things

ISAC Integrated Sensing and Communication

KKT Karush-Kuhn-Tucker

LoS Line of Sight

LTE Long Term Evolution

MBS Macro Base Station

MEC Mobile Edge Computing

MILP Mixed Integer Linear Programming

MIMO Multiple-Input Multiple-Output

NLoS None Line of Sight

NOMA Non-orthogonal Multiple Access

NTN Non-Terrestrial Network

OPEX Operating Expenditure

QCQP Quadratically Constrained Quadratic Programming

QoE Quality of Experience

QoS Quality of Service

RABS Robotic Aerial Base Station

RIS Reconfigurable Intelligent Surfaces

RSU Road Side Unit

SCA Successive Convex Approximation

SDR Semidefinite Relaxation

SINR Signal to Interference plus Noise Ratio

SNR Signal to Noise Ratio

SN Sensor Node

SR Satisfaction Rate

TSP Traveling Salesman Problem

TU Totally Unimodular

UAV Unmanned Aerial Vehicle

WPT Wireless Power Transfer

WSN Wireless Sensor Network

Chapter 1

Introduction

1.1 Research Motivations

Unmanned aerial vehicles (UAVs), commonly known as drones, are remotely controlled aircraft that operate without onboard pilots. Thanks to the advancements in manufacturing technologies, UAVs have shown a significant expansion in their classifications based on various criteria, such as payload capacity, size and weight, wing configuration, operational altitude, flying speed, and energy supply methods. This expansion aims to accommodate a broader range of applications and meet diverse environmental requirements. With increased flexibility and cost reduction, UAVs are now extensively employed beyond military domains and finding new applications in wider areas, i.e., remote monitoring, contamination detection, emergency rescue operations, and cargo delivery. Notably, one particularly appealing use of UAVs is employing them as aerial base stations (ABSs) to construct three-dimensional (3D) cellular networks. Compared to traditional terrestrial networks, aerial networks offer numerous advantages, such as enhanced flexibility, predominant line-of-sight (LoS) channel conditions, cost-effective deployment, and 3D manoeuvrability.

Several ABS prototypes have been showcased to the public at exhibitions and commercial events. For instance, the Zephyr project is a solar-powered stratospheric ABS developed by Airbus [1]. The key component of this system is an unmanned aerial system with a wingspan of 25m and a weight of 75kg, which operates at an altitude of 20 km above the ground and is powered by solar energy. Utilizing a dual rechargeable battery design, Zephyr can provide theoretically uninterrupted wireless service from the air. In the test flight conducted in 2018, Zephyr achieved a remarkable endurance of 25 days, 23 hours, and 57 minutes without being recharged. Thanks to the high operating altitude and long battery life, Zephyr has the potential

(a) Airbus Zephyr project [1]. (b) AT&T Flying COW project [2].

Fig. 1.1 Different prototypes of ABS.

to offer uninterrupted wireless coverage to previously unconnected areas. It is calculated that the coverage provided by Zephyr is equivalent to that of 250 terrestrial cell towers. Besides, AT&T has developed an ABS project known as the Flying Cell on wings (COW), which operates at a much lower altitude, i.e., approximately 100 meters [2]. The Flying COW is designed to provide 5G coverage to an area of approximately 25 km^2. Its intended applications include offering wireless service to ground users during disasters and boosting capacity during major events. A detailed survey of the ABS prototypes can be found in [3], which covers a wider range of commercial ABS projects such as Facebook Aquila, Google Loon, Nokia F-Cell, Eurecom Perfume and Huawei Digital Sky.

Thanks to the flexibility and wide coverage, ABSs have been effectively applied to provide emergency wireless service in the aftermath of natural disasters. A notable example occurred in July 2021 when Henan province, located in central China, experienced abrupt and extensive heavy rainfall, resulting in floods in this area. Consequently, the telecommunication infrastructures in Mihe county of Henan province were severely disrupted, leaving over 20,000 residents stranded. To address this critical situation, the Wing Loong UAV, equipped with an ABS, was deployed to establish emergency connections in the disaster-affected region [4]. Specifically, Wing Loong UAV took off from Guizhou province and completed a journey of approximately 1,200 kilometres in 4.5 hours to reach the mission area. It operated for a total of 8 hours in the affected zone. Within the initial two hours of operation, it facilitated connectivity for 2,572 users, resulting in 1,089.89 MB of data traffic. During the peak hour, there were at most 648 users connecting with the ABS simultaneously. In the following days, Wing Loong UAV continued to provide wireless connections to the Fuwai Central China Cardiovascular Hospital, which was among the hardest-hit medical facilities requiring emergency rescue operations.

This exemplary use case clearly demonstrates the significant potential of ABSs in fulfilling urgent communication requirements after natural disasters.

The study of ABSs has attracted significant attention from both academia and industry in recent years and has already been employed in recovering communication networks after natural disasters. However, this emerging field still presents numerous challenges that require further research and exploration. Firstly, due to the different service modes of ABSs compared to traditional terrestrial base stations, new performance metrics, such as propulsion energy consumption and air-to-ground path loss depending on their three-dimensional positioning, need to be introduced to evaluate aerial networks. Accordingly, how to achieve a balanced design among these different performance metrics remains a challenge for researchers. Secondly, while UAV communication has been utilised for emergency network reconstruction after natural disasters, employing ABSs to provide daily network services in urban areas still faces several challenges. For instance, the operational duration of ABSs is constrained by onboard battery capacity, the high mobility poses new safety risks in urban environments, and they would introduce new sources of noise pollution. Consequently, designing novel ABS prototypes that could provide aerial access to urban users safely and sustainably remains a valuable open problem.

1.2 Thesis Outcomes

This thesis aims to address the two key challenges raised in the above paragraph. Firstly, the competitive performance metrics in ABS-assisted networks are studied. As later discussed in Section 2.2, various metrics are employed to evaluate aerial network performance, and some of these metrics are contradictory. In other words, optimizing the network along certain dimensions may come at the cost of lowering other metrics. Therefore, it is crucial to design ABS-assisted networks in alignment with practical service requirements. Secondly, primarily constrained by the onboard battery capacity, the limited endurance of ABSs presents a practical implementation barrier, especially when they are involved in daily cellular networks rather than providing service to sporadic emergency communications. With this in mind, a novel ABS prototype called robotic aerial base station (RABS) is proposed to address this endurance issue, following which several fundamental use cases are proposed to demonstrate its advantages over other types of ABS. Specifically, the key contributions of this thesis are summarised as follows:

- A UAV-assisted wireless sensor network is studied in Chapter 3 where a UAV is dispatched to gather information from ground sensor nodes (SN) and transfer the collected data to a depot. The information freshness is captured by the age of information (AoI) metric, whilst the energy consumption of the UAV is seen as another performance criterion. Most importantly, the AoI and energy efficiency are inherently competing metrics, since decreasing the AoI requires the UAV to return to the depot more frequently, leading to higher energy consumption. To this end, UAV paths are designed to optimise these two competing metrics jointly and reveal the Pareto frontier. To formulate this problem, a multi-objective mixed integer linear programming (MILP) is proposed with a flow-based constraint set and solved by Bender's decomposition algorithm. Numerical results show that the proposed method allows for deriving non-dominated solutions among two competing metrics when designing the UAV path.

- To overcome the endurance issue of ABSs, in Chapter 4, a novel ABS prototype named robotic aerial base station (RABS) with grasping end-effectors is proposed, which can autonomously perch at tall urban landforms. Thanks to the energy-efficient grasping operation, RABSs are expected to offer seamless wireless connectivity in an energy-efficient manner. Specifically, the key components of such aerial platforms including both hardware and communication designs are discussed. By comparing with other types of non-terrestrial communication infrastructure such as hovering-based, tethered and laser-powered ABSs, RABSs show several advantages such as energy efficiency, flexible deployment, low noise pollution and adaptability to working on hash weather. A case study shows that RABSs can improve the minimum data rate of cellular networks significantly thanks to their flexibility and agility.

- In Chapter 5, the optimal deployment (fly to another grasping location or remain in the same one) and operation (active or sleep mode at an epoch) of a swarm of RABSs is studied based on the spatial-temporal distribution of underlying traffic load, which is formulated as an integer linear programming (ILP) aiming to maximise the volume of served traffic load under the on-board energy constraints. To tackle the curse of dimensionality of this ILP formulation, a special case with a single RABS in the system is first studied and solved by the proposed Lagrangian heuristic algorithm by exploiting the totally unimodularity structure. A polynomial-time method is then proposed to decompose the multi-RABS problem into several single-RABS

cases based on the Hungarian algorithm. In terms of aggregated traffic that can be supported, numerical results reveal that a single RABS outperforms four (4) fixed micro cells when the serving duration ranges from 12 to 24 hours, allowing in that sense efficient network densification. The traffic loaded in an RABSis 3.2 times higher than a fixed small cell when the traffic distribution is highly heterogeneous. Finally, the efficiency and performance of the proposed algorithms are also detailed.

- In Chapter 6, two novel application scenarios are studied to show the potential of RABSs in the upcoming 6G era. Firstly, an RABS is employed to bring further flexibility to integrated sensing and communication (ISAC) systems. Specifically, characterizing the spatial traffic distribution on a grid-based model, the RABS-assisted ISAC system is formulated as a robust optimisation problem to maximise the minimum satisfaction rate (SR) under a cardinality-constrained uncertainty set. The problem is reformulated as a mixed-integer linear programming (MILP) and solved approximately by the iterative linear programming rounding algorithm. Numerical investigations show that the minimum SR can be improved by 28.61% on average compared to fixed small cells. Secondly, a swarm of RABSs are expected to construct a flexible millimetre-wave (mmWave) multi-hop backhaul network according to the traffic spatial distribution and relocate their positions in subsequent time epochs according to the traffic temporal dynamic. The overall energy efficiency of the proposed framework is maximised by determining the RABS deployment, relocation and route formation under the channel capacity and hop constraints. The problem is formulated as a mixed-integer linear fractional programming (MILFP) and a two-stage method is developed to overcome the computational complexity. A wide set of numerical investigations reveals that compared to fixed small cells, only half as many RABSs are required to cover the same volume of traffic demand.

Fig. 1.2 clarifies the thesis organisation and emphasises the coherence between chapters. Through a review of existing ABS research in Section 2.2, two main research gaps are identified and studied in this thesis. Firstly, Chapter 3 presents a novel trajectory design framework to explore the trade-off between conflicting metrics. Secondly, in order to prolong the serving time of ABS, Chapter 4 proposes a novel ABS prototype named RABS, and the fundamental network operations are discussed in Chapter 5. Furthermore, in Chapter 6, RABS is introduced to

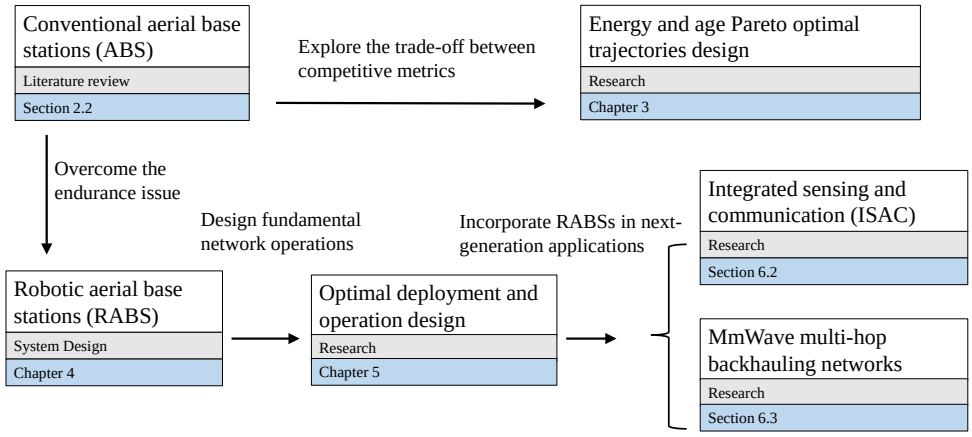

Fig. 1.2 Thesis organisation and main contributions.

next-generation network applications to further explore the potential and more possibilities.

During my PhD programme, the published papers are listed below:

1. **Yuan Liao** and Vasilis Friderikos, "Energy and Age Pareto Optimal Trajectories in UAV-Assisted Wireless Data Collection", *IEEE Transactions on Vehicular Technology*, vol. 71, no. 8, pp. 9101-9106, Aug. 2022.

2. **Yuan Liao** and Vasilis Friderikos, "Optimal Deployment and Operation of Robotic Aerial 6G Small Cells with Grasping End Effectors", *IEEE Transactions on Vehicular Technology*, vol. 72, no. 9, pp. 12248-12260, Sept. 2023.

3. **Yuan Liao**, Vasilis Friderikos and Halim Yanikomeroglu, "Robust Deployment and Resource Allocation for Robotic Aerial Base Station Enabled OFDM Integrated Sensing and Communication," *IEEE Wireless Communications Letters*, vol. 12, no. 10, pp. 1766-1770, Oct. 2023.

4. **Yuan Liao**, Vasilis Friderikos and Halim Yanikomeroglu, "Swarm of Robotic Aerial Base Stations for mmWave Multi-Hop Backhauling," *IEEE Wireless Communications Letters*, vol. 13, no. 3, pp. 666-670, March 2024,

5. **Yuan Liao** and Vasilis Friderikos, "Optimal Deployment and Operation of Robotic Aerial 6G Small Cells with Grasping End Effectors", *ICC 2022 - IEEE International Conference on Communications*, pp. 1-6, 2022.

6. **Yuan Liao** and Vasilis Friderikos, "Max-min Rate Deployment Optimisation for Backhaul-limited Robotic Aerial 6G Small Cells", *GLOBECOM 2022 - 2022 IEEE Global Communications Conference*, pp. 2963-2968, 2022.

The following manuscript has been submitted during the redaction of this thesis,

7. **Yuan Liao**, Vasilis Friderikos and Simon Saunders, "Robotic Aerial Base Stations with Grasping Capabilities: Network Densification without Densifying the Infrastructure", submitted to *IEEE Vehicular Technology Magazine*, 2022.

The relevance between the above-mentioned publications and chapters is presented in Table 1.1.

Table 1.1 Papers Related to Individual Chapters.

Chapter	Journal	Conference
Chapter 3	1	-
Chapter 4	7	6
Chapter 5	2	5
Chapter 6	3,4	-

Chapter 2

Background Study

2.1 Introduction

This chapter provides a comprehensive background study for this thesis, encompassing the following two main components. In the first Section 2.2, several state-of-the-art works in the area of ABS-assisted networks are reviewed to build up a high-level background for this thesis. The literature review aims to answer the following two questions. Firstly, compared to conventional terrestrial networks, which advantages and research opportunities of aerial base stations (ABSs) have attracted researchers focusing on this field. The second one is about how interdisciplinary advances, such as new radio technologies, artificial intelligence, and robotics research, have cross-fertilized the progress of research on ABS. In the second Section 2.3, a preliminary introduction of the mathematical theories and methods in integer linear programming would be provided, which will cover most of the mathematical tools used in the following chapters.

2.2 Literature Review: Aerial Base Stations in 5G Networks

As mentioned in Chapter 1, although ABS has been utilised to satisfy a wide range of practical requirements, such as constructing emergency connections, balancing the traffic load and covering unconnected areas, the use of aerial communications would also introduce new challenges to the network configurations. For example, ABS-assisted communication is more sensitive to energy consumption because UAVs are powered by onboard batteries with limited capacity. The inter-cell interference

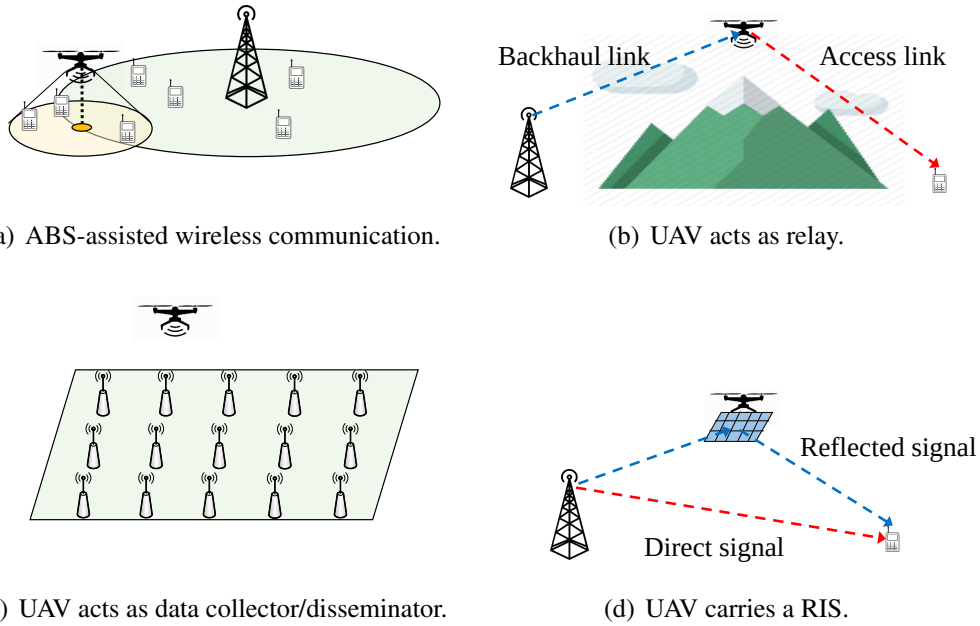

(a) ABS-assisted wireless communication.

(b) UAV acts as relay.

(c) UAV acts as data collector/disseminator.

(d) UAV carries a RIS.

Fig. 2.1 Typical use cases of UAV-assisted communication.

might be extremely large due to the dominant line of sight (LoS) channel conditions. A number of researchers started to contribute to this topic initially from the year of 2012 and a big wave has been shown since the year 2018 [5].

By exploring the inherent advantages of ABSs, the authors of [6, 7] envision different typical use cases of ABS-assisted networks shown in Fig. 2.1,

1) ABSs could be utilised to provide ubiquitous coverage when ground base stations (BSs) are damaged by natural disasters or overloaded in extremely crowded areas. The work [8] further studies this use case, in which an ABS flies cyclically with a ground BS as the centre when providing service to cell-edge users. The minimum throughput is maximised by optimizing the spectrum allocation, flying trajectory and user association.

2) ABSs could also act as relays to offer wireless connectivity between macro BSs and user clusters. In [9], an ABS is deployed as a two-way relay node to support multi-pair users.

3) ABSs are employed to disseminate and collect delay-tolerant to/from internet-of-things (IoT) devices. The work [10] continues to investigate this application scenario, in which an ABS is employed as a data collector to harvest information from sensor nodes.

4) ABSs are utilised as aerial platforms to carry reconfigurable intelligent surfaces (RIS). In [11], an RIS is carried by an ABS, in which system the worst-case signal-to-noise ratio (SNR) is maximised by optimizing the ABS placement, transmit beamforming as well as the 3D passive beamforming of the RIS.

Furthermore, considering the new radio requirements in future networks, ABSs are expected to play different roles in B5G/6G cellular networks, e.g., mobile edge computing (MEC) nodes [12], mobile cache devices [13], road side units (RSUs) in vehicular networks [14], and remote health monitoring [15]. In [16], a group of ABSs equipped with MEC devices cooperates to process computing tasks with the aim of optimizing the total energy consumption, job loss, and system delay jointly. The reinforcement learning algorithm is applied to determine the optimal offloading strategy and the proposed strategy is tested on a video surveillance system installed at the Catania University campus. The authors of [17] investigate a network including a swarm of ABSs with caching capability, in which the quality of experience is maximised by determining the ABS deployment, caching placement as well as user association. The high altitude platform station (HAPS) with computing, caching and communication capabilities is employed to assist intelligent transportation systems in [18].

Several metrics are used to evaluate the system performance of ABS-assisted networks. On the one hand, there are various metrics similar to conventional terrestrial communications, e.g., signal-to-interference-plus-noise ratio (SINR), communication throughput, delay, information freshness and energy efficiency. On the other hand, some new evaluation metrics are introduced to ABS systems for practical interests, such as the number of required ABSs, mission time and energy consumption. In [19], a group of ABSs is placed in a large-scale area where there are already several terrestrial BSs distributed, in which system the median SINR value (the SINR value that 50% of the users can achieve) is utilised as one of the performance metrics. The work in [20] studies a multi-ABS communication system. The aggregate throughput is maximised by determining the ABS trajectory and power allocation jointly. The authors of [21] investigate an ABS-assisted MEC network, in which the system latency is minimised by optimizing the ABS placement, user association and resource allocation. In [22, 23], an ABS is applied to collect data from a group of sensor nodes with the aim of minimizing the information freshness, which is captured by the age of information (AoI). The work [24] studies an ABS-enabled multicasting system. The completion time of this task is minimised by determining the ABS trajectory when ensuring the file recovery success probability. In [25], the number of ABSs

required in an IoT network is minimised, following which the optimal positions are determined. The energy-efficient trajectories for fixed-wing and rotary-wing UAVs are studied in [26] and [27], respectively. Notably, the aforementioned metrics are always inherently competing with each other, therefore, they are always included in a problem as objective functions and constraints to explore the trade-off. The following Table 2.1 investigates the fundamental trade-off in ABS-assisted networks.

To improve the aforementioned performance of ABS-assisted networks, a number of novel communication techniques are expanding from terrestrial to non-terrestrial networks, such as mmWave/THz communication, beamforming technique, non-orthogonal multiple access (NOMA), integrated access and backhaul (IAB) and cell-free massive multiple-input multiple-output (MIMO). The air-to-ground channel operating on mmWave frequencies is modelled in [28, 29], following which the authors of [30] study the 3D placement and orientation of ABSs to satisfy the LoS coverage. In [31], the user association and spectrum allocation problem for an mmWave-enabled ABS is solved via the machine learning method. Supposing an ABS is equipped with a multi-antenna array, the beamforming technique is employed to improve the communication performance in [32–34]. A survey of the beamforming-enabled ABS systems can be found in [35]. Furthermore, NOMA is a promising technique to improve spectrum efficiency and has presented huge potential in future wireless networks. Compared to orthogonal multiple access, NOMA shows significant benefits when users suffer from different channel conditions. The prototype design of NOMA-enabled ABS systems is proposed in [36] and the following works [37–40] study the deployment, trajectory design and power allocation problems, respectively. Besides, to overcome the limited capacity of the backhaul link when ABSs act as relays between mobile terminals and macro BSs, IAB is a promising technique to enhance the network capacity via allocating limited resources on both access and backhaul links [41], and firstly be introduced to ABS-assisted networks in [42]. In [43, 44], the placement and resource allocation problem of an in-band full-duplex enabled ABS is studied, and the following work [45] extends this model to multiple ABSs cases. To satisfy the extremely high wireless demands in B5G/6G networks, the cell-free massive MIMO technique is introduced to ABS-aided systems. The work in [46] studies the power allocation and user scheduling strategies for such a system and shows the benefit of the cell-free protocol compared to the conventional multi-cell configuration.

Furthermore, after formulating the mathematical models of the above problems, several interdisciplinary analytical frameworks are introduced to solve them efficiently, such as optimization algorithms, optimal transport theory, game theory and

machine learning methods. Although most of the problems in communications are non-convex, several efficient algorithms are developed to obtain an approximated solution in polynomial time. In [47], the UAV trajectory planning problem with interference consideration is formulated as non-convex programming and solved by successive convex approximation (SCA) method. The following work in [20] proposes a parallel algorithm based on the alternating direction method of multipliers method to make the problem implementable efficiently on multi-core CPUs. In [48], the penalty dual decomposition method is employed to achieve a near-optimal solution for the ABS-assisted NOMA system. The block successive upper-bound minimization algorithm is introduced to the ABS-assisted MEC system and shows a better computational efficiency than the conventional block coordinate descent algorithm. In [49], a cache-enable ABS system with a limited capacity of backhaul channel is investigated and solved by the semidefinite relaxation technique. However, due to the complexity and non-convex properties of the formulated problems, mathematical programming tools cannot always provide a satisfactory solution in a reasonable time. Therefore, a number of researchers have developed heuristic algorithms to handle these complex problems. In [22], a genetic algorithm is used to capture a trajectory when minimizing the AoI. In [44], an approximation method with a provable performance guarantee is proposed to obtain the optimal 3D positions of ABSs. Moreover, the optimal transport theory is a mathematical tool that can obtain an optimal mapping between two arbitrary probability measures. It is utilised in [50–52] to determine the ABS hovering time and user association, respectively. Game theory is also exploited to design the ABS-assisted networks. For instance, the authors of [53] propose a game-theoretic approach to deploy ABSs in hostile jamming environments. In [54], game theory is utilised to allocate limited spectrum resources in a task-driven network. Besides these conventional mathematical tools, several machine learning based methods are introduced to enable ABSs to operate in a more complex environment. For instance, since the ABS flight can be modelled as a Markov decision process naturally, reinforcement learning has been employed to determine the UAV trajectory to optimise the AoI [55–57], completion time [58], operating energy [59] and request satisfaction rate [60]. The deep learning method uses multi-layer neural networks to explore higher-level features from the raw input data. In [61], the users' distribution and ABS deployment are used as the input and output to train a convolutional neural network (CNN). Afterwards, the ABS deployment can be predicted by simply inputting users' location to this trained CNN. In [62], the deployment and user association problem for a swarm of ABSs with visible light communications is formulated as a non-convex problem, which is di-

rectly solved by a proposed machine learning framework. Moreover, learning-based methods are also utilised to determine the caching placement, MEC task offloading and resource allocation in [63–66], respectively. The following Table 2.2 compares different methods and clarifies their pros and cons.

To further evaluate the performance of ABSs in realistic scenarios, a number of ABS simulation platforms have been developed to simulate ABS operations in different environments and conditions. In [68], a multi-UAVs communication network simulation platform based on OPNET Modeler is developed to evaluate the network performance and verify real applications. The authors of [69] develop a simulator for integrated space-air-ground networks that supports various mobility traces and protocols. Furthermore, researchers also design and implement experiments for ABSs to verify the proposed protocol and algorithms. In [70], authors develop an ABS with a Raspberry Pi1 set with a static WiFi channel, employing a novel technique to localise and reposition itself closer to ground users to provide optimal connectivity. The authors of [71] employ a combination of simulations and measurements to quantify the impact of Long Term Evolution (LTE) enabled ABSs on an existing ground LTE network. The results show that ABSs have a significant impact on the coverage area and interference to macro cells, even with reduced transmit power. The work in [72] employs the Helikite, a combination of kite and balloon, to act as an ABS to provide wireless coverage when backhauling to a satellite. The authors of [73] employs the ABS as a relay between a ground user and a ground BS by using COTS Quad-Rotor carbon body frame, DJI propulsion system and open source PIXHAWK 2 flight controller. An optimal deployment algorithm is also developed to enhance the network capacity. In [74], an aerial relay carried by a Parrot Drone Mk2 UAV is tested in both rural and urban areas by using the decode-and-forward protocol. Besides, the works [75–79] measure the air-to-ground channel model and [80] validates the energy consumption model via flight experiments.

Besides, more comprehensive reviews in the area of ABS-aided networks can be further found in [81–83] and the specific literature reviews closely related to the research topics of this thesis can be found in the following Chapters 3-6 separately.

2.3 Integer Linear Programming

Integer programming focuses on maximizing or minimizing an objective function subject to a set of constraints and integer restrictions on some or all of the variables. A remarkable number of practical problems can be formulated as integer programming

Table 2.1 Fundamental tradeoffs in ABS-assisted networks

Paper	Objective function	Constraint	Method[1]
[8]	Minimum throughput	Spectrum resource	OPT
[9, 47, 48]	Minimum throughput	Transmission power	OPT
[10]	Energy consumption	Required volume of collected data	OPT
[16]	Energy consumption , job loss, delay	-	RL
[17]	Quality of experience	Caching capacity	OPT
[18]	Delay	Spectrum resource, computing capacity	RL, OPT
[11]	SNR	-	OPT
[20]	Sum rate	Interference	OPT
[21]	Latency	Computing capacity	OPT
[22, 23]	Maximum and average AoI	-	HEU
[24]	Completion time	Job loss	OPT
[25]	Number of covered users	Number of ABSs	HEU
[30]	SNR	Number of ABSs	HEU
[32]	Sum rate	Minimum throughput	OPT
[33]	Minimum throughput	Transmission power	OPT
[34]	Number of connected users	-	RL
[37]	Sum rate	Transmission power, quality of service (QoS)	OPT
[38]	Minimum throughput	Transmission power, spectrum resource	OPT
[40]	Minimum secure computing capacity	Communication and computation resource	OPT
[43]	Sum rate	Transmission power	HEU
[53]	Volume of collected data	-	GT
[55]	Average AoI	Onboard energy	RL
[57]	Average AoI, Energy consumption	Spectrum resource	RL
[58]	Completion time	Onboard energy	RL
[59]	Energy consumption	Time requirements	HEU, RL
[60]	Service success rate	Flight time	RL
[61]	Number of connected users	-	DL
[62]	Transmission power	Rate requirements	DL
[64]	Network utility	Communication and computation capacity	RL
[65]	Number of offloaded tasks	QoS	RL

[1] OPT, HEU, GT, RL and DL represent the optimization, heuristic, game theory, reinforcement learning and deep learning methods.

Table 2.2 Comparision of different methods

Method[1]		Advantages	Disadvantages
OPT	Exact algorithms for NP-hard problems (e.g. cutting plane, branch and bound)	Could achieve the global optimal solutions. Have been packaged by several commercial solvers such as gurobi [67].	Computational complexity is exponential.
	Approximation programming methods (e.g. SCA, difference of convex algorithm)	Low computational complexity. The quality of solutions can be guaranteed. (e.g. It is proven that the SCA can converge to the KKT point.)	Cannot achieve the global optimal solution. Solving large-scale problems is still time-consuming.
HEU	Approximation algorithms (e.g., greedy algorithm, random rounding method)	Computational complexity is polynomial so that they can solve problems efficiently. The quality of solutions can be guaranteed by approximation ratio.	There are no general methods so they are designed case by case. Some problems are proven to be inapproximatable which means that there is no algorithm with approximation ratio.
	Meta-heuristic algorithms (e.g. GA, simulated annealing)	They are general methods so that can be used for different problems. Especially powerful for combinatorial optimization problems.	The quality of solutions cannot be guaranteed.
ML	RL (including deep reinforcement learning)	No requirements on the properties of functions, such as monotonicity and convexity. Powerful for dynamic environments.	Some problems cannot be modelled as the MDP. The design of the reward functions is not as straightforward as objective functions.
	DL (e.g. CNN)	Can make decisions efficiently once the neural networks are trained.	Training neural networks is time-consuming. Needs a large number of data to ensure the training accuracy.
GT		Powerful for the problems with special structures, such as matching, association and allocation.	Some problems cannot be modelled as a game.

[1] OPT, HEU, GT, RL and DL represent the optimization, heuristic, game theory, reinforcement learning and deep learning methods.

due to its robustness, e.g., resource assignment, machine scheduling, transportation design, capital budgeting, and stock investment. Moreover, some other branches of mathematics are closely related to integer programming and mutually reinforce each

other. For example, several problems in graph theory, such as matching, colouring, and clique problems, can be formulated as equivalent integer programming problems. Some integer programming problems can be solved optimally or approximately via results in graph theory, such as the shortest-path problem and the max-flow min-cut theorem.

In this section, the integer linear programming (ILP) in which both the objective function and constraints are linear is investigated. It can be written as the following formulation,

$$\min\{c^T x + h^T y : Ax + Gy \leq b, x \in \mathbb{Z}_+^n, y \in \mathbb{R}_+^p\}, \tag{2.1}$$

where $\mathbb{Z}_+^n$ denotes the set of non-negative integer n-dimensional vectors and $\mathbb{R}_+^p$ indicates the set of non-negative real n-dimensional vectors. x and y are integer and continuous variables, respectively. Notably, because maximizing an objective function is equal to minimizing its negative and an equality constraint can be represented by two inequality constraints, (2.1) could normalise all of ILP problems.

2.3.1 Totally Unimodular Matrices

Most ILP problems are NP-hard, obtaining the global optimal solution in polynomial time is generally not possible unless P=NP. However, in this subsection, the special structure of a type of ILP that can be solved optimally in polynomial time is investigated. Hereafter, consider an ILP with only integer variables as,

$$\min\{c^T x : Ax \leq b, x \in \mathbb{Z}_+^n\}, \tag{2.2}$$

The linear relaxation of (2.2) is obtained by relaxing the integer variables into the real field and can be written as,

$$\min\{cx : Ax \leq b, x \in \mathbb{R}_+^n\}, \tag{2.3}$$

The following definition defines a special type of constraint matrix A.

Definition 2.1: *An integer $m \times n$ matrix A is totally unimodular (TU) if the determinant of each square submatrix of A is equal to 0, 1, or -1.*

The following proposition illustrates the property of a TU matrix, which could ease the solving process for (2.2).

Proposition 2.1: *If A is TU, then $P(b) = \{x \in \mathbb{R}_+^n : Ax \leq b\}$ is an integer polyhedron for all $b \in \mathbb{Z}^m$ for which it is not empty.*

The integer polyhedron means that all extreme points of a polyhedron take integer values. The proof and more extensions of Proposition 1 can be found in Section III.1.2 of [84]. Moreover, the fundamental theorem of linear programming indicates that if there is an optimal solution for linear programming, there must be at least one extreme point that achieves the optimal value [85]. Considering Proposition 1, it can be observed that if the linear programming (2.3) is feasible and A is TU matrix, there is at least one integer optimal solution for (2.3). In other words, if the ILP problem (2.2) has a TU constraint matrix A and $b \in \mathbb{Z}^m$, the optimal solution of which can be obtained by solving its linear relaxation (2.3) via polynomial-time algorithms, such as interior point method [85].

In order to check whether a matrix is TU conveniently, the following proposition is proposed to characterise the totally unimodularity derived from Definition 2.1 and a sufficient condition as the corollary. Note that the proof of them can be found in Section III.1.2 of [84].

Proposition 2.2: *The following statements are equivalent. 1) A is TU. 2) For every $J \subseteq N = \{1,2,...,n\}$, there exists a partition J_1, J_2 of J such that,*

$$\Big| \sum_{j \in J_1} a_{ij} - \sum_{j \in J_2} a_{ij} \Big| \leq 1, \quad \forall i \in \{1,...,m\}, \tag{2.4}$$

Corollary 2.1: *If the (0, 1, -1) matrix A has no more than two nonzero entries in each column, and if $\sum_i a_{ij} = 0$ if column j contains two nonzero coefficients, then A is TU.*

2.3.2 Lagrangian Relaxation, Duality and Subgradient Method

Assume that the constraints in (2.2) can be partitioned into two sets, one is the set of complicating constraints means that the ILP problem after removing these constraints can be solved easily, and the other is the set of nice constraints. Problem (2.2) can be written as,

$$z_{IP} = \min\ c^T x, \tag{2.5a}$$
$$s.t. \quad A_c x \leq b_c, \qquad \text{(complicating constraints)} \tag{2.5b}$$
$$A_n x \leq b_n, \qquad \text{(nice constraints)} \tag{2.5c}$$
$$x \in \mathbb{Z}_+^n, \tag{2.5d}$$

where (2.5b) are complicating constraints and (2.5c) are nice constraints. In other words, by dropping the constraints in (2.5b), the relaxed problem is easier to solve

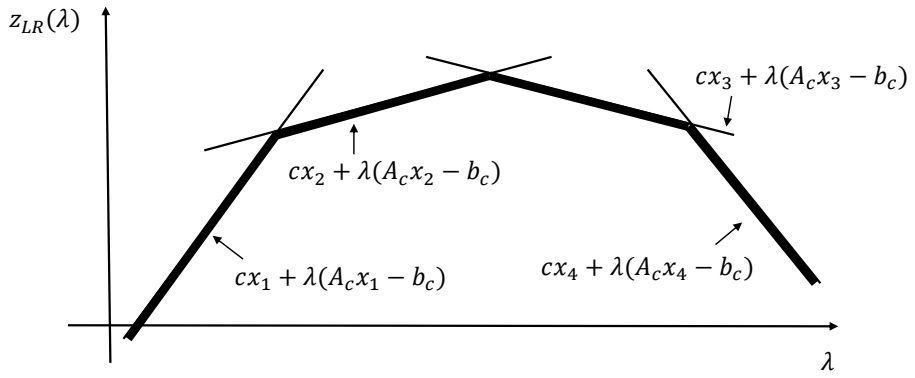

Fig. 2.2 The form of $z_{LR}(\lambda)$ in one-dimension case.

than the original problem (2.2). Notably, 'easy to solve' means the problem has been solvable in polynomial or pseudo-polynomial time for most applications [86].

The idea of Lagrangian relaxation is to drop the complicating constraints to the objective function by multiplying a non-negative Lagrangian multiplier λ, that is,

$$z_{LR}(\lambda) = \min\ c^T x + \lambda^T (A_c x - b_c), \tag{2.6a}$$

$$s.t. \quad A_n x \leq b_n, \tag{2.6b}$$

$$x \in \mathbb{Z}_+^n, \tag{2.6c}$$

where $z_{LR}(\lambda)$ denotes the Lagrangian relaxation. The relaxed problem (2.6) does not include the complicating constraints thus it is easy to solve. Moreover, observing that the constraint (2.5b) is introduced to the objective function as a penalty term and λ is required to be non-negative. It can be realised that violation of the constraints (2.5b) makes the penalty term positive, thus (2.5b) could be satisfied if λ is suitably large. Moreover, the Lagrangian relaxation problem (2.6) is certainly a lower-bound for (2.5) with any value of λ, that is, $z_{LR}(\lambda) \leq z_{IP}$. The Lagrangian dual problem calculating the largest lower-bound can be expressed as,

$$z_{LD} = \max_{\lambda \geq 0} z_{LR}(\lambda), \tag{2.7}$$

Subsequently, a key issue is to determine an appropriate value of λ such that the Lagrangian dual z_{LD} can be achieved. It can be observed from (2.6) is a piece-wise concave function as shown in Fig. 2.2, thus the problem (2.7) is a non-differential convex problem. There are several algorithms to solve the Lagrangian dual (2.7), e.g., subgradient method, outer-approximation method, and Bundle method. Here a brief introduction to the subgradient method is provided.

Definition 2.2: *A vector g is a subgradient for the function $f: \mathbb{R}^n \to \mathbb{R}$ at x_0 if $f(x) \leq f(x_0) + g^T(x - x_0)$, $\forall x \in \mathbb{R}^n$.*

It can be easily verified that the vector $(A_c x_\lambda - b_c)$ is a subgradient at any λ for which x_λ is optimal for the problem (2.6) because for any $\mu \in \mathbb{R}^m$, the following inequality always holds,

$$\begin{aligned} z_{LR}(\mu) &= \min_{x \in \mathbb{X}} \{c^T x + \mu^T (A_c x - b_c)\} \\ &\leq c^T x_\lambda + \mu^T (A_c x_\lambda - b_c) \\ &= c^T x_\lambda + \lambda^T (A_c x_\lambda - b_c) + (A_c x_\lambda - b_c)^T (\mu - \lambda) \\ &= z_{LR}(\lambda) + (A_c x_\lambda - b_c)^T (\mu - \lambda), \end{aligned} \tag{2.8}$$

where $\mathbb{X}$ is the feasible region defined by (2.6b) and (2.6c).

Generalizing from the conventional gradient method, the subgradient method can be adapted straightforwardly by replacing gradients with subgradients. Given an initial point λ^0, a sequence $\{\lambda^k\}$ is generated following the rule,

$$\lambda^{k+1} = \lambda^k + \alpha^k (A_c x_{\lambda^k} - b_c), \tag{2.9}$$

where x_{λ^k} is optimal by solving $z_{LR}(\lambda^k)$ in (2.6) and α^k is a positive scalar step size. Unlike the gradient method for differential functions, the subgradient may not be an ascent direction for non-differential functions. However, it is proved that $\{\lambda^k\}$ converges to the optimal solution λ^* for Lagrangian dual (2.7) if $\alpha^k \to 0$, $k \to \infty$ and $\sum_{k=0}^{\infty} \alpha^k = \infty$ [87]. Therefore, the step size $\{\alpha^k\}$ should be chosen carefully to guarantee the convergence.

2.3.3 Bender's Decomposition

Bender's decomposition is a promising technique for solving large-scale ILP problems, which could partition the original problem into a group of smaller sub-problems and solve them iteratively. Because Bender's decomposition decentralises the overall computation burden, it has been widely used in the design of large-scale communication systems [88].

Consider an ILP problem including both integer and real variables as follows,

$$\min \; c^T x + h^T y, \tag{2.10a}$$

$$s.t. \quad Ax = b, \tag{2.10b}$$

$$Cx + Dy = d, \tag{2.10c}$$

$$x \in \mathbb{Z}_+^n,\ y \in \mathbb{R}_+^p, \tag{2.10d}$$

where (2.10b) are the constraints containing only integer variables and (2.10c) are in terms of both integer and real variables. Notably, the inequality constraint can be rewritten as the equality form by adding slack variables. Bender's decomposition partitions the problem (2.10) into two smaller problems: a master problem contains integer variables and a primal sub-problem includes real variables. Firstly, write the problem (2.10) in terms of the x-variables as,

$$\min\ c^T x + g(x), \tag{2.11a}$$
$$s.t.\quad Ax = b, \tag{2.11b}$$
$$x \in \mathbb{Z}_+^n, \tag{2.11c}$$

where $g(x)$ is a function of x and defined by the following primal sub-problem,

$$\min\ h^T y, \tag{2.12a}$$
$$s.t.\quad Dy = d - Cx, \tag{2.12b}$$
$$y \in \mathbb{R}_+^p, \tag{2.12c}$$

Note that (2.12) contains only the real variable y once the value of x is given, thus it is linear programming. It can be observed that if (2.12) is unbounded for some x, the original problem (2.10) is also unbounded. Moreover, the dual problem of (2.12) can be written as the following (2.13) and the duality gap is 0 for linear programming, thus (2.12) and (2.13) have the same optimal value.

$$\max_{\pi}\ \pi^T (d - Cx), \tag{2.13a}$$
$$s.t.\quad \pi^T D \leq h, \tag{2.13b}$$

where π is the associated dual variable. The key observation is that the constraint (2.13b) is not related to the values of x. Furthermore, the feasible region defined by (2.13b) is not empty if and only if (2.12) is unbounded. Assuming the feasible region is not empty, all extreme points $(\beta_p^1, ..., \beta_p^I)$ and extreme rays $(\beta_r^1, ..., \beta_r^J)$ of this feasible region are enumerated, where I and J are the numbers of extreme points and extreme rays, respectively. Recalling the polyhedral theory in the Section I.4.4 of [84], for a given value of x, the dual problem (2.13) can be solved by checking 1) $(\beta_r^j)^T (d - Cx) > 0$ for an extreme ray β_r^j, in which case the dual problem (2.13) is unbounded and the primal formulation (2.12) is infeasible. 2) an extreme point β_p^i

Algorithm 1 Bender's Decomposition

1: Initialise the RMP without any cuts in (2.15b)-(2.15c). Set $k = 0$.
2: **repeat**
3: Solve the RMP. Denote the solution as x^k and θ^k.
4: Introduce x^k to the dual sub-problem (2.13). Solve (2.13) and denote the optimal objective value as $g(x^k)$.
5: **if** $g(x^k) < \infty$ **then**
6: Acquire an extreme point from the solution of (2.13) and add an optimality cut (2.15c) to RMP.
7: **else**
8: Acquire an extreme ray and add a feasibility cut (2.15b).
9: **end if**
10: $k = k + 1$.
11: **until** $g(x^k) = \theta^k$

maximises the value of $(\beta_p^i)^T(d - Cx)$, in which case both primal and dual problems have finite optimal solutions. Therefore, the dual problem (2.13) can be reformulated as,

$$\min_{\theta} \ \theta, \tag{2.14a}$$

$$s.t. \quad (\beta_r^j)^T(d - Cx) \leq 0, \quad j = 1, ..., J, \tag{2.14b}$$

$$(\beta_p^i)^T(d - Cx) \leq \theta, \quad i = 1, ..., I. \tag{2.14c}$$

Note that the constraints in (2.14b) and (2.14c) are always named as feasibility and optimality cuts, respectively. Introducing (2.14) into the master problem (2.11), the following equal reformulation for the original problem can be written as,

$$\min \ c^T x + \theta, \tag{2.15a}$$

$$s.t. \quad (\beta_r^j)^T(d - Cx) \leq 0, \quad j = 1, ..., J, \tag{2.15b}$$

$$(\beta_p^i)^T(d - Cx) \leq \theta, \quad i = 1, ..., I. \tag{2.15c}$$

$$Ax = b, \tag{2.15d}$$

$$x \in \mathbb{Z}_+^n. \tag{2.15e}$$

Although the above process shows the equality between (2.10) and (2.15), generating all of the constraints in (2.15b)-(2.15c) is not practical because of the exponential number of extreme points and extreme rays. To this end, a problem with a similar form as (2.15) but which does not consist of all the constraints in (2.15b)-(2.15c) is constructed and referred to as the relaxed master problem (RMP). According to the nominal use of Bender's decomposition, add the optimality and feasibility cuts

according to the solution of the dual sub-problem (2.13) to the RMP and solve it iteratively. The procedure of Bender's decomposition is summarised as Algorithm 1.

In [89], the following proposition is illustrated to prove the convergence of Algorithm 1.

Proposition 2.3: *The upper and lower bounds for the optimal solution of the original problem* (2.10) *can be obtained from the step 3 and* (4) *in Algorithm 1 as,*

$$\begin{cases} \mathsf{LB}^k = c^T x^k + \theta^k, & \text{(2.16a)} \\ \mathsf{UB}^k = c^T x^k + g(x^k), & \text{(2.16b)} \end{cases}$$

Therefore, when the gap between LB^k and UB^k is tightened to 0, the optimal solution for the original problem (2.10) is achieved, as shown by the stopping condition in the step (11) of Algorithm 1.

Chapter 3

Energy and Age Pareto Optimal Trajectories in UAV-assisted Wireless Data Collection

3.1 Introduction

In this chapter, an unmanned aerial vehicle (UAV) is dispatched to gather information from ground sensor nodes (SN) and transfer the collected data to a depot. To make real-time decisions and enable seamless operation in such networks, the freshness of received information, which is measured by the so-called age of information (AoI), is of critical significance and has received significant attention recently [90]. Besides, due to the limited capacity of onboard batteries, the aspect of energy consumption is seen as a key challenge in UAV-enabled wireless networks. Revealing the underlying trade-off between those two inherently competing metrics is the main focus of this chapter. The two extreme points in the Pareto curve are when only the AoI is minimised and when only the energy consumption is taken into account. In the first case, the UAV creates a star trajectory meaning that the UAV returns to the depot every time data are collected from a ground SN to minimise the AoI. On the other extreme, the trajectory will be a Hamiltonian path with minimal energy consumption. Between those two extreme scenarios are the cases where the UAV returns to the depot after serving a subset of SNs, as shown in Fig. 3.1. The focus of this work is to reveal the non-dominated operating points in the continuum between those two extreme points of operation.

As reviewed in Section 2.2, several existing works concentrated on information freshness, i.e., AoI, in UAV-aided wireless networks. In [22, 23], a UAV is applied to

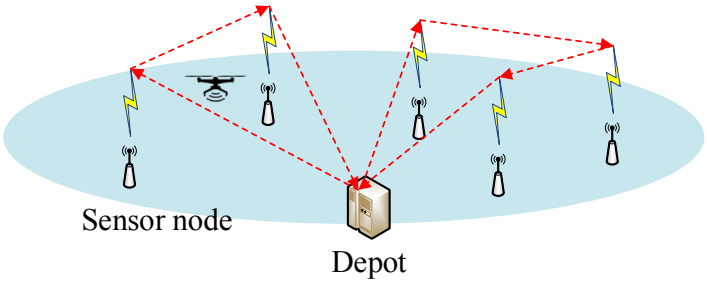

Fig. 3.1 Illustration of the proposed multi-return-allowed mode.

collect data from a group of SNs and then return to the depot for further processing with the aim of minimizing the AoI. The following work extends this model to a multi-UAV use case in [91], whereas [92] provides overarching architectural aspects of networked operation and connection of multiple UAVs. In [93], the UAV is deployed as a relay between a source node and a destination node, and the focus is to provide efficient trajectory design in order to minimise the peak AoI. An AoI-aware UAV trajectory is designed through a reinforcement learning based approach in [94]. Furthermore, the UAV is applied to sense information from the target area directly and the trade-off between the sensing and communication is investigated in [95].

In parallel, several existing research works investigated energy-efficient path planning since the onboard battery limitation is one of the key challenges in UAV-assisted networks. In [10, 50], the UAV is deployed to collect data from static SNs and moving ground devices, respectively, in which the energy is minimised by trajectory design. A UAV is deployed to cover most users with minimum transmit power in [96]. The energy-efficient trajectory of a rotary-wing UAV is designed with a guaranteed communication requirement in [27]. Furthermore, a closely relevant problem of energy trade-off between the UAV and ground terminals is studied in [97].

Considering the aforementioned competing nature between energy consumption and AoI, a multi-return-allowed serving mode is proposed to capture the balance between them, in which the UAV is allowed to return to the depot at any time during the serving cycle. Furthermore, although the AoI-aware path has been considered in [22, 23, 91], these works considered only Hamiltonian paths whereas this work allows several returns to the depot during a serving cycle. Therefore, these previous works can be considered as a special case of the proposed framework. Moreover, to obtain the UAV visiting order initially, a multi-objective mixed integer linear programming (MILP) based on a flow-based constraint set is formulated under the assumption that the UAV can only collect data when hovering, which is then solved

by Bender's decomposition in a decentralised manner. Afterwards, a more general trajectory in which the UAV can communicate while flying is studied to further improve both metrics. Numerical investigations show that the multi-return-allowed mode achieves the Pareto optimal trade-off between the two competing metrics.

3.2 System Model and Problem Formulation

Hereafter, consider a wireless sensor network with K SNs denoted by the set $\mathcal{K} = \{1, 2, ..., K\}$, the Cartesian coordinates of which are known and fixed at $\mathbf{w}_i \in \mathbb{R}^2, \forall i \in \mathcal{K}$. A rotary-wing UAV acts as a collector to gather information from all SNs and subsequently transmit/offload the data to the depot located at $\mathbf{w}_0 \in \mathbb{R}^2$. For notational convenience, the depot and SNs are combined as an extended set $\mathcal{K}^a = \{0\} \bigcup \mathcal{K}$, in which the depot is indexed by 0.

3.2.1 System Model and Age of Information

To obtain the UAV visiting order first, the fly-hover-communication protocol proposed by [27] is adopted in sections 3.2 and 3.3 for the communication between UAV and SNs, in which the UAV gather information only when hovering right above SNs. Afterwards, a more general solution in which the UAV can communicate while flying is studied in Section 3.4. Similar to [22, 93, 94], the UAV is assumed to fly at a constant altitude H corresponding to authority regulations and safety considerations.[1] Because the 3GPP specification [98] specifies that the air-to-ground channel can be well approximated by the free-space path loss model when the UAV altitude is higher than 40m and 100m in the rural and urban scenarios, respectively, the achievable rate R for the communication between UAV and SNs can be calculated as follows,

$$R = B \cdot \log_2 \left(1 + \frac{P^t \rho_0}{\sigma^2 H^2}\right), \tag{3.1}$$

where B is the available bandwidth, P^t is the transmission power of SNs and σ^2 is the power of channel noise. The reference channel power gain at 1 m distance is denoted by ρ_0 and can be calculated via Friis transmission equation, that is, $\rho_0(\text{dB}) = -20\log_{10}(4\pi f_c/c)$, where f_c is the carrier frequency and c is the speed of light [99]. Furthermore, the hovering duration when the UAV collects data from SN

[1] In the free-space channel model (3.1), it can be seen that R is monotonically decreasing with H. Thus, the UAV would fly at the lowest height corresponding to regulations and safety considerations to achieve the best R.

i can be calculated by $T_i^h = D_i/R$, where D_i is the data size to be uploaded from SN i. Accordingly, the energy consumption of the UAV when hovering and gathering data from SN i can be calculated by $E_i^h = P^h T_i^h$, where P^h is the hovering power of the UAV.

Similar to [22, 23, 91, 93], the UAV is assumed to keep a fixed speed V so that the flying time between two adjacent SNs can be calculated by $T_{ij}^f = \|\mathbf{w}_i - \mathbf{w}_j\|/V$, where $\|\cdot\|$ denotes the 2-norm for a vector [2]. The corresponding energy consumption is $E_{ij}^f = P^f T_{ij}^f$, where P^f is the propulsion power of the UAV and given by [27] as a function of V,

$$P^f(V) = P_0\Big(1+\frac{3V^2}{U_{tip}^2}\Big) + P_i\Big(\sqrt{1+\frac{V^4}{4v_0^4}} - \frac{V^2}{2v_0^2}\Big)^{1/2} + \frac{1}{2}d_0\rho sAV^3, \tag{3.2}$$

where P_0 and P_i represent blade profile power and induced power, respectively. U_{tip} is the tip speed of the rotor blade. v_0 denotes the mean rotor induced velocity when hovering. d_0 and s are the fuselage drag ratio and rotor solidity, respectively. Also, ρ and A denote the air density and rotor disc area, respectively. More details regarding the propulsion power can be found in Appendix A. Subsequently, define a graph $\mathcal{G} = (\mathcal{K}^a, \mathcal{E})$, where $\mathcal{E}$ denotes the set of edges, that is, $\mathcal{E} \triangleq \{(i,j)\big|\,\forall i,j \in \mathcal{K}^a, i \neq j\}$. For clarity of exposition, the hovering time and energy consumption at the depot is seen as zero, that is, $T_0^h = 0$ and $E_0^h = 0$. Accordingly, the time consumption to the edge (i,j) is defined as,

$$\begin{aligned} T_{ij} &= T_i^h + T_{ij}^f \\ &= \begin{cases} \frac{\|\mathbf{w}_i - \mathbf{w}_j\|}{V}, & \text{if } i = 0,\ (i,j) \in \mathcal{E}, \\ \frac{D_i}{B\log_2\left(1+\frac{P^t\rho_0}{\sigma^2 H^2}\right)} + \frac{\|\mathbf{w}_i - \mathbf{w}_j\|}{V}, & \text{if } i \neq 0,\ (i,j) \in \mathcal{E}. \end{cases} \end{aligned} \tag{3.3}$$

Similarly, the energy consumption for edge (i,j) is defined as,

$$\begin{aligned} E_{ij} &= E_i^h + E_{ij}^f \\ &= \begin{cases} \frac{P^f\|\mathbf{w}_i - \mathbf{w}_j\|}{V}, & \text{if } i = 0,\ (i,j) \in \mathcal{E}, \\ \frac{P^h D_i}{B\log_2\left(1+\frac{P^t\rho_0}{\sigma^2 H^2}\right)} + \frac{P^f\|\mathbf{w}_i - \mathbf{w}_j\|}{V}, & \text{if } i \neq 0,\ (i,j) \in \mathcal{E}. \end{cases} \end{aligned} \tag{3.4}$$

[2] Initially, the UAV speed is assumed as a constant to better focus on the visiting order, whilst it can be further optimized as the case in Section 3.4.

Note that both T_{ij} and E_{ij} can be seen as constants once the environment is given. The energy consumption for a given trajectory $\mathcal{Q}$ can be calculated as $E = \sum_{(i,j)\in\mathcal{Q}} E_{ij}$, where $(i,j) \in \mathcal{Q}$ means that the UAV travels from i to j adjacently; observe that E is a function of $\mathcal{Q}$.

The concept of AoI is used to measure the freshness of information for each SN and derive the average AoI among all SNs to evaluate the performance of the system. Similar to [22, 23, 91], the AoI of SN i is defined as the time interval from when the UAV starts collecting information from i to when it returns to the depot. Mathematically, given a cycle consisting of r SNs with the depot as the start (end) vertex, the UAV visits $i_0 \to i_1 \to i_2 ... \to i_r \to i_{r+1}$ in tandem, where $i_0 = i_{r+1} = 0$ and $i_k \in \mathcal{K}, k = 1,2,...,r$. Define the AoI of SNs visited by this cycle recursively, that is,

$$\begin{cases} A_{i_r} = T_{i_r i_{r+1}} = T_{i_r 0}, & \text{(3.5a)} \\ A_{i_k} = T_{i_k i_{k+1}} + A_{i_{k+1}}, \ k = 1,2,...,r-1, & \text{(3.5b)} \end{cases}$$

where (3.5a) defines the AoI of last visited SN i_r and (3.5b) calculates others.

Furthermore, the average AoI among all SNs, calculated by $\overline{A} = \sum_{i\in\mathcal{K}} A_i / K$, is adopted to evaluate the performance of the system. Observe that $\overline{A}$ is a function of the UAV trajectory. However, since the trajectory cannot be explicitly expressed, $\overline{A}$ is challenging to formulate. However, Lemma 3 in [22] provides an alternative expression of $\overline{A}$ when the trajectory $\mathcal{Q}$ is given, that is,

$$\overline{A} = \sum_{(i,j)\in\mathcal{Q}} \frac{f_{ij}}{K} T_{ij}, \tag{3.6}$$

where f_{ij} denotes the number of visited SNs during the period between the most recent departure from the depot and arrival at j. For instance, given a cycle as $i_0 \to i_1 \to i_2 ... \to i_r \to i_{r+1}$ where $i_0 = i_{r+1} = 0$, the values of f_{ij} can be obtained as $f_{i_0 i_1} = 0$, $f_{i_1 i_2} = 1$, ..., $f_{i_r i_{r+1}} = r$.

3.2.2 Flow-based Constraint Set and Problem Formulation

In this subsection, a multi-objective optimisation problem is formulated based on a flow-based constraint set [100] to achieve the trade-off between the average AoI and energy consumption by designing the UAV path.

$$\min_{\mathbf{X}} \sum_{(i,j)\in\mathcal{E}} E_{ij} x_{ij}, \tag{3.7a}$$

$$\min_{\mathbf{Y}} \sum_{(i,j)\in\mathcal{E}} T_{ij}\frac{y_{ij}}{K}, \tag{3.7b}$$

$$s.t. \quad \sum_{i\in\mathcal{K}} x_{0i} = \sum_{i\in\mathcal{K}} x_{i0}, \tag{3.7c}$$

$$\sum_{i\in\mathcal{K}^a} x_{ij} = 1,\ \forall j \in \mathcal{K}, \tag{3.7d}$$

$$\sum_{i\in\mathcal{K}^a} x_{ji} = 1,\ \forall j \in \mathcal{K}, \tag{3.7e}$$

$$\sum_{(i,j)\in\mathcal{E}} y_{ij} - \sum_{(j,i)\in\mathcal{E}} y_{ji} = 1,\ \forall i \in \mathcal{K}, \tag{3.7f}$$

$$y_{oi} = 0,\ \forall i \in \mathcal{K}, \tag{3.7g}$$

$$0 \le y_{ij} \le K x_{ij},\ \forall (i,j) \in \mathcal{E}, \tag{3.7h}$$

$$x_{ij} \in \{0,1\},\ \forall (i,j) \in \mathcal{E}, \tag{3.7i}$$

where x_{ij} are binary variables and $x_{ij}=1$ represents that the edge (i,j) is travelled by the UAV, y_{ij} are the flow variables associated to all edges, $\mathbf{X} \triangleq \{x_{ij} \,|\, (i,j)\in\mathcal{E}\}$ and $\mathbf{Y} \triangleq \{y_{ij} \,|\, (i,j)\in\mathcal{E}\}$ are the set of variables. Observe that (3.7c)-(3.7e) impose the degree constraints for all SNs and depots. Also, (3.7i) reflects the binary restriction for the variable x_{ij}. The following two Lemmas illustrate how the constraints (3.7f)-(3.7h) operate for the aforementioned multi-return-allowed mode.

Lemma 3.1: *The constraint* (3.7f) *guarantees that if a vertex set $\mathcal{K}' \subseteq \mathcal{K}^a$ constitutes a cycle, the depot must be included by $\mathcal{K}'$, i.e., $0 \in \mathcal{K}'$.*

Proof: Lemma 3.1 can be proven this by induction. Assume that there is a cycle without the depot, and choose an SN $i_1 \in \mathcal{K}'$ as the start (end) point. Thus, all SNs in this $\mathcal{K}'$ are visited in tandem and denote the path as $i_1 \to i_2 \to ... \to i_r \to i_1$. Now set $y_{i_1 i_2} = c$. According to (3.7f), it follows that $y_{i_2 i_3} = c+1$, ..., $y_{i_r i_1} = c+r-1$. Therefore, it can be easily seen that $\sum_{(i_1,j)\in\mathcal{E}} y_{i_1 j} - \sum_{(j,i_1)\in\mathcal{E}} y_{j i_1} = c-(c+r-1) = 1-r$, which contradicts with (3.7f). This completes the proof of Lemma 3.1. □

Lemma 3.2: *The constraints* (3.7f)-(3.7h) *guarantee that the following equation is achieved,*

$$y_{ij} = \begin{cases} f_{ij}, & \text{if } x_{ij} = 1, \\ 0, & \text{otherwise.} \end{cases} \tag{3.8}$$

Proof: Lemma 3.1 shows that a cycle generated by problem (3.7) must consist of the depot. Choosing the depot as the start (end) point, the UAV would fly along the trajectory $0 \to i_1 \to i_2 ... \to i_r \to 0$. (3.7h) guarantees that y_{ij} can achieve a nonzero value only when $x_{ij}=1$, otherwise, y_{ij} is forced to 0 when $x_{ij}=0$. Recalling the constraints (3.7f) and (3.7g), it follows that $y_{0 i_1}=0$, $y_{i_1 i_2}=1$, ..., $y_{i_r 0}=r$. Since the

inequality $r \leq K$ is satisfied, the constraints (3.7h) would not be broken when $x_{ij} = 1$. This completes the proof of Lemma 3.2. □

Lemma 3.1 illustrates that there is a feasible multi-return-allowed path generated by problem (3.7) and Lemma 3.2 shows that the second objective function (3.7b) calculates the average AoI. Thus, problem (3.7) solves the proposed multi-return-allowed serving mode with $\overline{A}$ and E as the objective functions. Also, the proposed flow-based formulation can be easily extended to characterise other AoI-aware path planning problems in the aforementioned existing papers. For example, the previous paper [22] limits the UAV back to the depot after all SNs have been visited, which mode can be formulated as a MILP by removing the energy objective (3.7a) and replacing the constraint (3.7c) by $\sum_{i\in\mathcal{K}} x_{0i} = 1$, $\sum_{i\in\mathcal{K}} x_{i0} = 1$.

3.3 Single Objective and Bender's decomposition

Hereafter Problem (3.7) is transformed to a single objective problem via the weighted linear combination technique and Bender's decomposition is applied to decentralise the overall computational burden when the problem scale is large.

3.3.1 Weighted Linear Combination

Various techniques are proposed to handle multi-objective optimisation problems, e.g., mathematical programming methods [101] and machine learning-based strategies [102]. In this chapter, a widely used method is utilised, i.e., associate the objective functions (3.7a) and (3.7b) with weighting coefficients and minimise the weighted sum after normalisation, that is,

$$\min_{\mathbf{X},\mathbf{Y}} \ \lambda \frac{\sum_{(i,j)\in\mathcal{E}} T_{ij}\frac{y_{ij}}{K} - \overline{A}_{min}}{\overline{A}_{max} - \overline{A}_{min}} + (1-\lambda)\frac{\sum_{(i,j)\in\mathcal{E}} E_{ij}x_{ij} - E_{min}}{E_{max} - E_{min}}, \tag{3.9a}$$

$$s.t. \quad (3.7c) - (3.7i), \tag{3.9b}$$

where $\overline{A}_{min}$ and $\overline{A}_{max}$ are the minimal and maximal achieved value of $\overline{A}$ respectively, E_{min} and E_{max} are the minimal and maximal energy consumption respectively, λ and $(1-\lambda)$ denote the weights of two matrices. Theorem 4 in [101] establishes that the solution of problem (3.9) is Pareto optimal if $\lambda \in [0,1]$.

To derive an explicit expression of the objective function in problem (3.9), the extreme values of $\overline{A}$ and E should be obtained first. Since $\{T_{ij} \big| \forall (i,j) \in \mathcal{E}\}$ satisfy the triangle inequality, the UAV would return to the depot immediately after visiting

each SN to minimise $\overline{A}$. The corresponding energy consumption is certainly the maximal value of E. Similarly, as shown in (3.4), $\{E_{ij} \big| \forall (i,j) \in \mathcal{E}\}$ satisfy the triangle inequality and are monotonically increasing of $\|\mathbf{w}_i - \mathbf{w}_j\|$. Therefore, the most energy-efficient path would include exactly one cycle with the shortest flying distance, that is, a Travelling Salesman Problem (TSP) solution. The corresponding average AoI can be seen as $\overline{A}_{max}$. Notably, although TSP is an NP-hard problem, it has been well researched so that it is reasonable to assume that the TSP solution, as well as its corresponding E_{min} and $\overline{A}_{max}$, are known hereafter.

Moreover, it is worth noting that choosing the value of weights in the weighted sum method is a crucial step as it should incorporate accurately the preferences of the decision-maker. There are two broad classes of approaches identified in recent years. Firstly, with the ranking method, the authors of [103] first compare the importance of different objective functions pairwise and yield a comparison matrix via the analytical hierarchy process, following which the eigenvalues of this matrix can be used as the weights. However, this method is inefficient for the problem (3.7) because it only involves two objective functions. In such cases, the ranking method converges to the second approach for selecting weight values, namely the rating method. When using the rating method, the decision-maker assigns independent values of relative importance to both AoI and energy consumption based on their preferences, expert judgment, and analytical methods. After solving the converted single-objective problem (3.9), sensitivity analysis could be conducted to understand how changes in the weights affect the solution and whether the chosen weights are appropriate. The value of weights can be then adjusted based on the performance of the optimisation results [104].

3.3.2 Applying Bender's Decomposition

For notational convenience, the constant terms in (3.9a) are ignored and Problem (3.9) can be rewritten as,

$$\min_{\mathbf{X},\mathbf{Y}} \sum_{(i,j)\in\mathcal{E}} C^T_{ij} y_{ij} + \sum_{(i,j)\in\mathcal{E}} C^E_{ij} x_{ij}, \tag{3.10a}$$

$$s.t. \quad (3.7c) - (3.7i), \tag{3.10b}$$

where $C^T_{ij} \triangleq \lambda T_{ij}/(K\overline{A}_{max} - K\overline{A}_{min})$ and $C^E_{ij} \triangleq (1-\lambda)E_{ij}/(E_{max} - E_{min})$ are coefficients defined for simplicity.

Because Bender's decomposition exploits the problem structure and decentralises the overall computation burden [89], it is seen as a promising approach for large-scale MILP. To apply Bender's decomposition for problem (3.10), first rewrite it as the following (3.11) without loss of optimality,

$$\min_{\mathbf{X}} \sum_{(i,j)\in\mathcal{E}} C^E_{ij} x_{ij} + g(\mathbf{X}), \tag{3.11a}$$

$$s.t. \quad (3.7c) - (3.7e),\ (3.7i), \tag{3.11b}$$

where $g(\mathbf{X})$ is defined to be the optimal solution of the following problem,

$$\min_{\mathbf{Y}} \sum_{(i,j)\in\mathcal{E}} C^T_{ij} y_{ij}, \tag{3.12a}$$

$$s.t. \quad (3.7f) - (3.7h). \tag{3.12b}$$

Problem (3.12) is certainly a linear programming with respect to $\mathbf{Y}$ for a given value of $x_{ij} \in \mathbf{X}$. Then, write the dual for (3.12) as,

$$\max_{\{\alpha_i\}\{\beta_i\}\{\gamma_{ij}\}} \sum_{i\in\mathcal{K}} \alpha_i - \sum_{(i,j)\in\mathcal{E}} K x_{ij} \gamma_{ij}, \tag{3.13a}$$

$$s.t. \ -\alpha_i + \beta_i - \gamma_{0i} \le C^T_{0i},\ \forall i \in \mathcal{K}, \tag{3.13b}$$

$$\alpha_i - \gamma_{i0} \le C^T_{i0},\ \forall i \in \mathcal{K}, \tag{3.13c}$$

$$\alpha_i - \alpha_j - \gamma_{ij} \le C^T_{ij},\ \forall (i,j) \in \mathcal{E},\ i \ne 0,\ j \ne 0, \tag{3.13d}$$

$$\gamma_{ij} \ge 0,\ \forall (i,j) \in \mathcal{E}, \tag{3.13e}$$

where $\{\alpha_i \,|\, i \in \mathcal{K}\}$, $\{\beta_i \,|\, i \in \mathcal{K}\}$ and $\{\gamma_{ij} \,|\, (i,j) \in \mathcal{E}\}$ are dual variables. The key observation is that the constraints (3.13b)-(3.13e) are not related to the values of $\mathbf{X}$. Supposing the polyhedron constructed by the constraints (3.13b)-(3.13e) has M extreme points and N extreme rays, (3.13) has an equivalent form as follows [89].

$$\min_{\theta} \theta, \tag{3.14a}$$

$$s.t. \sum_{i\in\mathcal{K}} \alpha^{p,m}_i - \sum_{(i,j)\in\mathcal{E}} K x_{ij} \gamma^{p,m}_{ij} \le \theta,\ \forall m = 1,...,M, \tag{3.14b}$$

$$\sum_{i\in\mathcal{K}} \alpha^{r,n}_i - \sum_{(i,j)\in\mathcal{E}} K x_{ij} \gamma^{r,n}_{ij} \le 0,\ \forall n = 1,...,N, \tag{3.14c}$$

where $(\alpha^{p,m}_1,...,\alpha^{p,m}_K,\beta^{p,m}_1,...,\beta^{p,m}_K,\gamma^{p,m}_{01},...,\gamma^{p,m}_{K-1K})$ and $(\alpha^{r,n}_1,...,\alpha^{r,n}_K,\beta^{r,n}_1,...,\beta^{r,n}_K,$ $\gamma^{r,n}_{01},...,\gamma^{r,n}_{K-1K})$ denote the m^{th} extreme point and n^{th} extreme ray of the polyhedra

Algorithm 2 Applying Bender's Decomposition to (3.10)

1: Initialise the RMP without any cuts in (3.15c). Set $k = 0$.
2: **repeat**
3: Solve the RMP. Denote the solution as $\mathbf{X}^k$ and θ^k.
4: Introduce $\mathbf{X}^k$ to the dual sub-problem (3.13). Solve (3.13) and denote the optimal objective value as $g(\mathbf{X}^k)$.
5: **if** $g(\mathbf{X}^k) < \infty$ **then**
6: Acquire an extreme point from the solution of (3.13) and add an optimality cut (3.14b) to RMP.
7: **else**
8: Acquire an extreme ray and add a feasibility cut (3.14c).
9: **end if**
10: $k = k + 1$.
11: **until** $g(\mathbf{X}^k) = \theta^k$

constructed by (3.13b)-(3.13e), respectively. The constraints in (3.14b) and (3.14c) are named optimality and feasibility cuts, respectively. Since problem (3.12) is a linear programming of which the strong duality is held, (3.12), (3.13) and (3.14) achieve the same optimal solution. Accordingly, replacing the component $g(\mathbf{X})$ by (3.14), (3.11) can be rewritten as the following form without loss of optimality,

$$\min_{\mathbf{X},\theta} \sum_{(i,j)\in\mathcal{E}} C^E_{ij} x_{ij} + \theta, \tag{3.15a}$$

$$s.t. \quad (3.7c) - (3.7e),\ (3.7i), \tag{3.15b}$$

$$(3.14b) - (3.14c). \tag{3.15c}$$

Problems (3.15) and (3.12) are always referred as master problem and sub-problem, respectively.

However, since the number of the constraints in (3.14b) and (3.14c) is extremely large, generating all of them is impractical. To this end, a problem having a similar form as (3.15) but which does not consist of all the constraints in (3.15c) is constructed and referred to as the relaxed master problem (RMP). According to the nominal use of Bender's decomposition, adding the optimality and feasibility cuts according to the solution of dual sub-problem (3.13) to the RMP and solving it iteratively. The procedure of Bender's decomposition is summarised as Algorithm 2, a realisation of which implemented by the Python API of Gurobi 9.1.2 [67] can be found in github.com/Yuanliaoo/BDforUavPath.

Hereafter, the optimality and convergence of Bender's decomposition are reviewed. Firstly, denoting the optimal solution of problem (3.10) as ψ^*, the Proposition 2.3 in Section 2.3 shows that at iteration k, the lower and upper bounds of

ψ^* can be obtained by step 3 and 4 of Algorithm 2 by $\mathsf{LB}^k = \sum_{(i,j)\in\mathcal{E}} C_{ij}^E x_{ij}^k + \theta^k$ and $\mathsf{UB}^k = \sum_{(i,j)\in\mathcal{E}} C_{ij}^E x_{ij}^k + g(\mathbf{X}^k)$, respectively. i.e. $\mathsf{LB}^k \leq \psi^* \leq \mathsf{UB}^k$. Therefore, when the gap between LB^k and UB^k is equal to 0, the global optimal solution ψ^* is surely achieved, shown as the stopping criteria in the step 11 of Algorithm 2. Also, Theorem 3.1 and Section 4 in [89] illustrate that the procedures would terminate and converge to ψ^* within a finite number of iterations.

3.4 General Trajectory Optimisation

The fly-hover-communication protocol in the preceding section determines the visiting order of the UAV. However, both the average AoI and energy can be further optimised when the UAV is allowed to collect data while flying instead of the binary flying status. In this section, assuming the visiting order has been solved by problem (3.7), the UAV trajectory is further optimised to improve the system performances without the fly-hover-communication assumption.

Denote the UAV location at time t projected onto the horizontal plane by $\mathbf{q}(t) \in \mathbb{R}^2$. The achievable rate between UAV and the SN i at time t can be rewritten from (3.1) as a function of $\mathbf{q}(t)$,

$$R(\mathbf{q}(t)) = B \cdot \log_2 \Big(1 + \frac{P^t \rho_0}{\sigma^2 (H^2 + \|\mathbf{q}(t) - \mathbf{w}_i\|^2)}\Big), \tag{3.16}$$

To guarantee the successful decoding and the quality of service (QoS), the signal-to-noise-ratio (SNR) at the UAV, defined by $\text{SNR} \triangleq \frac{P^t \rho_0}{\sigma^2 (H^2 + \|\mathbf{q}(t) - \mathbf{w}_i\|^2)}$, is required to greater than a pre-specified threshold [50, 96]. Because SNR is monotonically decreasing with $\|\mathbf{q}(t) - \mathbf{w}_i\|^2$, this QoS requirement can be satisfied by a distance constraint, i.e., $\|\mathbf{q}(t) - \mathbf{w}_i\|^2 \leq d^{th}$. As shown in Fig. 3.2, the UAV can only receive data from SN i when it is located in a circular disc with the centre $\mathbf{w}_i$ and radius d^{th}, which is named as coverage area hereafter.

The UAV trajectory only needs to be determined within the coverage areas because in other areas the UAV would fly along line segments to decrease both the flying time and energy. Firstly, select the initial and final locations for the UAV trajectory within a certain circular coverage area. As shown in Fig. 3.2, when the UAV visits i_{r-1} and i_r adjacently, the intersection point of the line segment $\mathbf{w}_{i_{r-1}}\mathbf{w}_{i_r}$ and the edge of the coverage area is defined as the initial location of the UAV trajectory when it flies and connects to SN i_r, denoted by $\mathbf{q}_{i_r}^I$, while the intersection of $\mathbf{w}_{i_r}\mathbf{w}_{i_{r+1}}$ and the edge is defined as the final point and denoted by $\mathbf{q}_{i_r}^F$. Once the

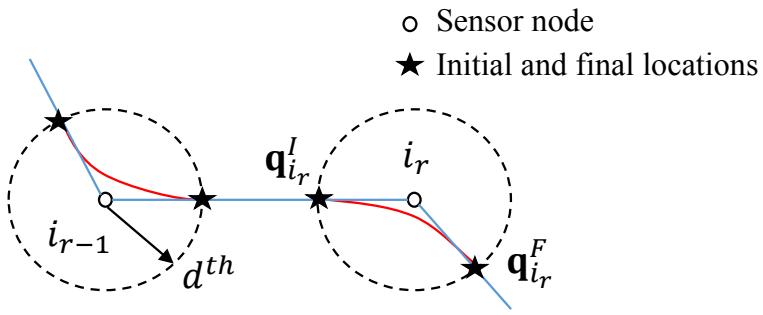

Fig. 3.2 Illustration of further trajectory optimisation. The blue line represents the path solved by problem (3.7) while the red line shows a possible solution of the optimised trajectory obtained by (3.17).

start and final locations are fixed, the UAV trajectory when flying across the coverage area of SN i_r can be optimised by the following problem,

$$\min_{\{\mathbf{q}(t)\},T_{i_r}} \int_0^{T_{i_r}} P^f(\|\dot{\mathbf{q}}(t)\|)\,dt, \tag{3.17a}$$

$$\min_{\{\mathbf{q}(t)\},T_{i_r}} \frac{f_{i_{r-1}i_r}}{K} T_{i_r}, \tag{3.17b}$$

$$s.t. \quad \int_0^{T_{i_r}} R(\mathbf{q}(t))\,dt \geq D_{i_r}, \tag{3.17c}$$

$$\mathbf{q}(0) = \mathbf{q}_{i_r}^I, \quad \mathbf{q}(T_{i_r}) = \mathbf{q}_{i_r}^I, \tag{3.17d}$$

$$\|\mathbf{q}(t) - \mathbf{w}_{i_r}\|^2 \leq d^{th},\ \forall t \in [0, T_{i_r}], \tag{3.17e}$$

$$\|\dot{\mathbf{q}}(t)\| \leq V^{max},\ \forall t \in [0, T_{i_r}], \tag{3.17f}$$

where T_{i_r} denotes the flying time when the UAV travels through the coverage area of SN i_r, $\|\dot{\mathbf{q}}(t)\|$ calculates the norm of the UAV velocity at time t and V^{max} denotes the maximum UAV speed. The objective functions (3.17a) and (3.17b) optimise the partial energy consumption and average AoI, respectively. (3.17c) guarantees that the data collection is completed during this period and (3.17f) is the maximum speed constraint.

Similar to Section 3.3, problem 3.17 is first converted to a single-objective problem by applying the linear combination technique, that is,

$$\min_{\{\mathbf{q}(t)\},T_{i_r}} C^E \int_0^{T_{i_r}} P^f(\|\dot{\mathbf{q}}(t)\|)\,dt + C^T T_{i_r}, \tag{3.18a}$$

$$s.t. \quad (3.17c) - (3.17f), \tag{3.18b}$$

where $C^E \triangleq (1-\lambda)/(E_{max}-E_{min})$ and $C^T \triangleq \lambda f_{i_{r-1}i_r}/(K\overline{A}_{max}-K\overline{A}_{min})$ are combination coefficients similar to section III-A. Notably, because the UAV is allowed to collect data while flying in this section, $E_{max}, E_{min}, \overline{A}_{max}$ and $\overline{A}_{min}$ may not be the bounds of the system performances anymore. However, involving them in the coefficients can provide a scaling balance between these two performances, i.e. average AoI and energy, because they are in different measurements. ($\overline{A}$ in second and E in Joule).

Problem (3.17) is challenging to solve for the following two main reasons. First, (3.17) involves an infinite number of variables $\{\mathbf{q}(t)\}$ that is over continuous time t. Second, both the objective function (3.17a) and the constraint (3.17c) are non-convex with respect to decision variables. Fortunately, after being converted to a single objective problem by linear combination technique, (3.17) has been solved perfectly in the previous work [27]. Specifically, in Section IV of [27], the path discretisation technique is applied to discretise the variables $\{\mathbf{q}(t)\}$ and the successive convex approximation (SCA) method is then utilised to solve the non-convex problem. The solving procedure proposed by [27] is reviewed in the following two subsections.

3.4.1 Path Discretisation

Path discretisation is a method which can discretise the continuous variables and is suitable for the case without the mission time information [27]. In (3.18), the flying time T_{i_r} is one of the optimisation variables and cannot be pre-specified, thus the path discretisation technique is employed.

With path discretisation, the UAV trajectory when it flies in the coverage area of SN i_r, i.e., $\{\mathbf{q}(t)\}$, is discretised into $M+1$ line segments, which are represented by $M+2$ waypoints $\{\mathbf{q}_m\}_{m=0}^{M+1}$. Thus, the constraint (3.17d) could be rewritten as $\mathbf{q}_0 = \mathbf{q}_{i_r}^I$, $\mathbf{q}_{M+1} = \mathbf{q}_{i_r}^I$. Moreover, the adjacent waypoints should satisfy the following constraints,

$$\|\mathbf{q}_{m+1} - \mathbf{q}_m\| \leq \Delta_{max}, \quad \forall m \in \{0,1,...,M\}, \tag{3.19}$$

where Δ_{max} is a pre-specified maximum value of each line segment, in which the UAV velocity and the distance between the UAV and SN are both approximately unchanged. [27] suggests that the value of Δ_{max} can be chosen as $\Delta_{max} \ll H$ and M should be set as $M \geq \frac{2d^{th}}{\Delta_{max}} - 1$. Denote $T_m^{i_r}$ as the duration time when the UAV is in the line segment m. Then the velocity along this line segment is given by $\mathbf{v}_m = \frac{\mathbf{q}_{m+1}-\mathbf{q}_m}{T_m^{i_r}}$ and the total flying time within the coverage area can be calculated by $T_{i_r} = \sum_{m=0}^{M} T_m^{i_r}$.

Afterwards, rewrite the transmission rate and propulsion power by the discrete variables. According to (3.16), the rate when the UAV located at the waypoint $\mathbf{q}_m$ can be expressed as,

$$R(\mathbf{q}_m) = B \cdot \log_2 \Big(1 + \frac{P^t \rho_0}{\sigma^2 (H^2 + \|\mathbf{q}_m - \mathbf{w}_i\|^2)}\Big), \tag{3.20}$$

Denoting the length of line segment m as $\Delta_m \triangleq \|\mathbf{q}_{m+1} - \mathbf{q}_m\|$ and introducing $V = \frac{\Delta_m}{T_m^{i_r}}$ to the equation (2), the propulsion power can be rewritten as,

$$\begin{aligned} &P^f\big(\frac{\Delta_m}{T_m^{i_r}}\big) \\ =&P_0\Big(1 + \frac{3}{U_{tip}^2}\big(\frac{\Delta_m}{T_m^{i_r}}\big)^2\Big) + P_i\Big(\sqrt{1 + \frac{1}{4v_0^4}\big(\frac{\Delta_m}{T_m^{i_r}}\big)^4} - \frac{1}{2v_0^2}\big(\frac{\Delta_m}{T_m^{i_r}}\big)^2\Big)^{1/2} + \frac{1}{2} d_0 \rho s A \big(\frac{\Delta_m}{T_m^{i_r}}\big)^3, \end{aligned} \tag{3.21}$$

As a result, problem (3.18) can be reformulated as,

$$\min_{\{\mathbf{q}_m\},\{T_m^{i_r}\}} \underbrace{C^E\Big(P_0 \sum_{m=0}^{M} \big(T_m^{i_r} + \frac{3\Delta_m^2}{U_{tip}^2 T_m^{i_r}}\big) + P_i \sum_{m=0}^{M} \big(\sqrt{{T_m^{i_r}}^4 + \frac{\Delta_m^4}{4v_0^4}} - \frac{\Delta_m^2}{2v_0^2}\big)^{1/2} + \frac{1}{2} d_0 \rho s A \sum_{m=0}^{M} \frac{\Delta_m^3}{{T_m^{i_r}}^2}\Big)}_{\text{partial energy consumption}}$$

$$+ \underbrace{C^T \sum_{m=0}^{M} T_m^{i_r}}_{\text{partial average AoI}}, \tag{3.22a}$$

$$s.t. \quad B \sum_{m=0}^{M} T_m^{i_r} \log_2 \Big(1 + \frac{P^t \rho_0}{\sigma^2 (H^2 + \|\mathbf{q}_m - \mathbf{w}_i\|^2)}\Big) \geq D_{i_r}, \tag{3.22b}$$

$$\mathbf{q}_0 = \mathbf{q}_{i_r}^I,\ \mathbf{q}_{M+1} = \mathbf{q}_{i_r}^I, \tag{3.22c}$$

$$\|\mathbf{q}_m - \mathbf{w}_{i_r}\|^2 \leq d^{th}, \quad \forall m \in \{0,1,...,M+1\}, \tag{3.22d}$$

$$\|\mathbf{q}_{m+1} - \mathbf{q}_m\| \leq \min\{\Delta_{max}, T_m^{i_r} V^{max}\}, \quad \forall m \in \{0,1,...,M\}, \tag{3.22e}$$

$$T_m^{i_r} \geq 0, \quad \forall m \in \{0,1,...,M\}. \tag{3.22f}$$

Compared with (3.18), it can be observed that there are a finite number of optimisation variables in (3.22). However, problem (3.22) is still challenging to solve due to the non-convex objective function (3.22a) and constraint (3.22b). Thus, the SCA technique is then utilised to obtain a high-quality solution of (3.22) satisfying the Karush-Kuhn-Tucker (KKT) conditions.

3.4.2 Successive Convex Approximation

Firstly, considering the objective function (3.22a) in (3.22), it can be observed that only the second term in (3.22a) is non-convex with respect to the variables, while all other terms are convex. To tackle this issue, the non-negative slack variables $\{z_m \geq 0\}$ are introduced to (3.22) such that,

$$z_m^2 = \sqrt{{T_m^{i_r}}^4 + \frac{\Delta_m^4}{4v_0^4}} - \frac{\Delta_m^2}{2v_0^2}, \tag{3.23}$$

which can be rewritten as,

$$\frac{{T_m^{i_r}}^4}{z_m^2} = z_m^2 + \frac{\Delta_m^2}{v_0^2}, \tag{3.24}$$

Secondly, another set of slack variables $\{A_m\}$ are introduced to deal with the non-convexity in the constraints (3.22b),

$$A_m^2 = T_m^{i_r} \log_2\Big(1 + \frac{P^t \rho_0}{\sigma^2(H^2 + \|\mathbf{q}_m - \mathbf{w}_i\|^2)}\Big), \tag{3.25}$$

Therefore, the problem (3.22) can be reformulated as,

$$\min_{\substack{\{\mathbf{q}_m\},\{T_m^{i_r}\},\\ \{z_m\},\{A_m\}}} C^E\Big(P_0 \sum_{m=0}^{M}\big(T_m^{i_r} + \frac{3\Delta_m^2}{U_{tip}^2 T_m^{i_r}}\big) + P_i \sum_{m=0}^{M} z_m + \frac{1}{2} d_0 \rho s A \sum_{m=0}^{M} \frac{\Delta_m^3}{{T_m^{i_r}}^2}\Big) + C^T \sum_{m=0}^{M} T_m^{i_r}, \tag{3.26a}$$

$$s.t. \quad \sum_{m=0}^{M} A_m^2 \geq \frac{D_{i_r}}{B}, \tag{3.26b}$$

$$\mathbf{q}_0 = \mathbf{q}_{i_r}^I,\ \mathbf{q}_{M+1} = \mathbf{q}_{i_r}^I, \tag{3.26c}$$

$$\|\mathbf{q}_m - \mathbf{w}_{i_r}\|^2 \leq d^{th}, \quad \forall m \in \{0,1,...,M+1\}, \tag{3.26d}$$

$$\|\mathbf{q}_{m+1} - \mathbf{q}_m\| \leq \min\{\Delta_{max}, T_m^{i_r} V^{max}\}, \quad \forall m \in \{0,1,...,M\}, \tag{3.26e}$$

$$\frac{{T_m^{i_r}}^4}{z_m^2} \leq z_m^2 + \frac{\|\mathbf{q}_{m+1} - \mathbf{q}_m\|^2}{v_0^2}, \quad \forall m \in \{0,1,...,M\}, \tag{3.26f}$$

$$\frac{A_m^2}{T_m^{i_r}} \leq \log_2\Big(1 + \frac{P^t \rho_0}{\sigma^2(H^2 + \|\mathbf{q}_m - \mathbf{w}_i\|^2)}\Big), \quad \forall m \in \{0,1,...,M\}, \tag{3.26g}$$

$$T_m^{i_r} \geq 0, \quad \forall m \in \{0,1,...,M\}, \tag{3.26h}$$

$$z_m \geq 0, \quad \forall m \in \{0,1,...,M\}. \tag{3.26i}$$

Note that the section IV-B in [27] also proves that replacing the strict equality in (3.24) and (3.25) by inequality in the constraints (3.26f) and (3.26g) would not affect the optimality of the original problem (3.22). However, problem (3.26) is still

difficult to solve due to the non-convex constraints (3.26b), (3.26f) and (3.26g). The SCA method is then utilised to handle these non-convex constraints.

For the constraint (3.26b), it can be observed that each term of the left-hand side (LHS) of (3.26b) is convex with respect to A_m, which is global lower bounded by its first-order Taylor expansion, that is,

$$A_m^2 \geq {A_m^{(l)}}^2 + 2A_m^{(l)}(A_m - A_m^{(l)}), \tag{3.27}$$

where $A_m^{(l)}$ is the value of A_m at the lth iteration. Similarly, the LHS of (3.26f) is convex with respect to the variables and the right-hand side (RHS) is also convex, thus the lower bound of RHS can be obtained by its first-order Taylor expansion, that is,

$$\begin{aligned} & z_m^2 + \frac{\|\mathbf{q}_{m+1} - \mathbf{q}_m\|^2}{2v_0^2} \\ \geq & {z_m^{(l)}}^2 + 2z_m^{(l)}(z_m - z_m^{(l)}) - \frac{\|\mathbf{q}_{m+1}^{(l)} - \mathbf{q}_m^{(l)}\|^2}{v_0^2} + \frac{2}{v_0^2}(\mathbf{q}_{m+1}^{(l)} - \mathbf{q}_m^{(l)})^T(\mathbf{q}_{m+1} - \mathbf{q}_m), \end{aligned} \tag{3.28}$$

where the $z_m^{(l)}$ and $\mathbf{q}_m^{(l)}$ are the value of the corresponding variables in the lth iteration. Thirdly, because the RHS of (3.26g) is convex with respect to the term $H^2 + \|\mathbf{q}_m - \mathbf{w}_i\|^2$, a concave lower bound of it can be written as,

$$\begin{aligned} & \log_2\left(1 + \frac{P^t\rho_0}{\sigma^2(H^2 + \|\mathbf{q}_m - \mathbf{w}_i\|^2)}\right) \\ \geq & \log_2\left(1 + \frac{P^t\rho_0}{\sigma^2(H^2 + \|\mathbf{q}_m^{(l)} - \mathbf{w}_i\|^2)}\right) - \beta_m(\|\mathbf{q}_m - \mathbf{w}_i\|^2 - \|\mathbf{q}_m^{(l)} - \mathbf{w}_i\|^2) \\ \triangleq & R_m^{(l)}(\mathbf{q}_m), \end{aligned} \tag{3.29}$$

where β_m is a constant defined as $\beta_m = \frac{(\log_2 e)(P^t\rho_0/\sigma^2)}{(H^2+\|\mathbf{q}_m^{(l)}-\mathbf{w}_i\|^2)(H^2+\|\mathbf{q}_m^{(l)}-\mathbf{w}_i\|^2+P^t\rho_0/\sigma^2)}$.

By replacing the non-convex constraints (3.26b), (3.26f) and (3.26g) by their corresponding lower bounds at the lth iteration, the following problem can be obtained,

$$\min_{\substack{\{\mathbf{q}_m\},\{T_m^{i_r}\},\\ \{z_m\},\{A_m\}}} C^E\Big(P_0\sum_{m=0}^{M}\big(T_m^{i_r} + \frac{3\Delta_m^2}{U_{tip}^2 T_m^{i_r}}\big) + P_i\sum_{m=0}^{M} z_m + \frac{1}{2}d_0\rho sA\sum_{m=0}^{M}\frac{\Delta_m^3}{{T_m^{i_r}}^2}\Big) + C^T\sum_{m=0}^{M} T_m^{i_r}, \tag{3.30a}$$

$$s.t. \quad \sum_{m=0}^{M}\big({A_m^{(l)}}^2 + 2A_m^{(l)}(A_m - A_m^{(l)})\big) \geq \frac{D_{i_r}}{B}, \tag{3.30b}$$

Algorithm 3 SCA algorithm for solving (3.22)

1: Initialise the variables as $\{\mathbf{q}_m^{(0)}\}$, $\{T_m^{i_r(0)}\}$, $\{z_m^{(0)}\}$, $\{A_m^{(0)}\}$. Set $l=0$.
2: **repeat**
3: Solve the convex problem (3.30) and denote the solution as $\{\mathbf{q}_m^{(l)}\}$, $\{T_m^{i_r(l)}\}$, $\{z_m^{(l)}\}$, $\{A_m^{(l)}\}$.
4: Update $l=l+1$.
5: **until** The fractional decrease of the objective value of (3.30) is less than a given threshold.

Table 3.1 Parameter Settings

Parameter	Value	Parameter	Value
B	2 MHz	σ^2	-110 dBm
f_c	5.8 GHz	c	3×10^8 m/s
H	100 m	ρ_0	-47 dB
P^t	0.1 W	D_i	500 Mbits
K	10 (expect Fig. 3.5)	V	[10, 18, 30] m/s [27]
P^h	165 W [27]	P^f	[126, 162, 356] W [27]
d^{th}	50 m	V^{max}	30 m/s [27]

$$\frac{T_m^{i_r 4}}{z_m^2} \le {z_m^{(l)}}^2 + 2z_m^{(l)}(z_m - z_m^{(l)}) - \frac{\|\mathbf{q}_{m+1}^{(l)} - \mathbf{q}_m^{(l)}\|^2}{v_0^2} + \frac{2}{v_0^2}(\mathbf{q}_{m+1}^{(l)} - \mathbf{q}_m^{(l)})^T(\mathbf{q}_{m+1} - \mathbf{q}_m),$$
$$\forall m \in \{0,1,...,M\}, \tag{3.30c}$$

$$\frac{A_m^2}{T_m^{i_r}} \le R_m^{(l)}(\mathbf{q}_m), \quad \forall m \in \{0,1,...,M\}, \tag{3.30d}$$

$$(3.26c) - (3.26e), \quad (3.26h) - (3.26i). \tag{3.30e}$$

It can be verified that the problem (3.30) is a convex optimisation problem, which can thus be solved efficiently by using existing software toolbox such as CVX [105]. According to the basic procedure of the SCA method, a solution of (3.26) satisfying the KKT conditions can be achieved by successively updating the local point at each iteration via solving (3.30). The algorithm is summarised as Algorithm 3 and a realisation coded by MATLAB and CVX [105] can be found in github.com/Yuanliaoo/AoIEnergyUAVTraOpt.

3.5 Numerical Investigations

In this section, numerical investigations are presented to evaluate the proposed multi-return-allowed framework. The parameter settings are summarised in Table 3.1. The following three typical choices of speed are selected to simulate in this section, *Maximum-endurance (ME) speed* maximises the UAV endurance under any given

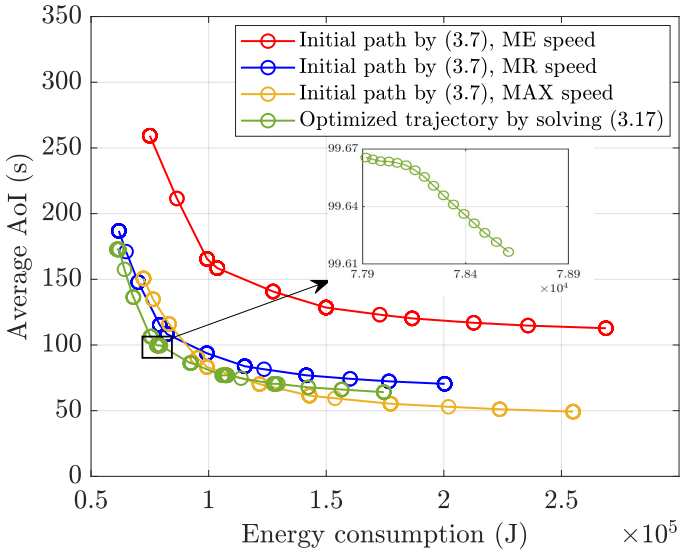

Fig. 3.3 Pareto front for $\overline{A}$ and E with different speed.

onboard energy; *Maximum-range (MR) speed* maximises the total travelling distance with any given onboard energy; *Maximal (MAX) speed* is the maximal achievable speed of the UAV. As illustrated in [27], the ME, MR and MAX speeds are 10 m/s, 18 m/s and 30 m/s, respectively. The corresponding values of the propulsion power are 126 W, 162 W and 356 W, as shown in Table 3.1.

Fig. 3.3 depicts the Pareto front of $\overline{A}$ and E. Firstly, solving (3.9) for different values of λ, the obtained results, represented by red, yellow and blue small circles, are in accordance with the intuition that $\overline{A}$ and E are competing with each other. It is worth pointing out that although the value of $\lambda \in [0,1]$ is sampled every 0.01 to plot Fig. 3.3, the actual results are distributed sparsely and overlap. The reason is that both $\overline{A}$ and E are functions of the UAV path, which are determined by the binary variables $\mathbf{X}$ in (3.7). Furthermore, optimizing the initial path with MR speed by solving (3.17), the obtained result, represented by green circles in Fig. 3.3, shows the improvement in both the $\overline{A}$ and E whatever the value of λ is. Besides, these Pareto points are distributed more densely because the variables in (3.17) can take continuous values.

Using the MR speed, the path designs under four different values of λ, 0, 0.5 and 1, as well as their corresponding performances are compared in Fig. 3.4(a), Fig. 3.4(b) and Fig. 3.4(c), respectively. As expected, frequent UAV returns to the depot result in reduced average AoI at the cost of more energy consumption. Moreover, Fig. 3.4(d) shows the trajectories optimised by Algorithm 3 when setting $\lambda = 0.5$. Comparing Fig. 3.4(b) and Fig. 3.4(d), it can be observed that when the UAV is

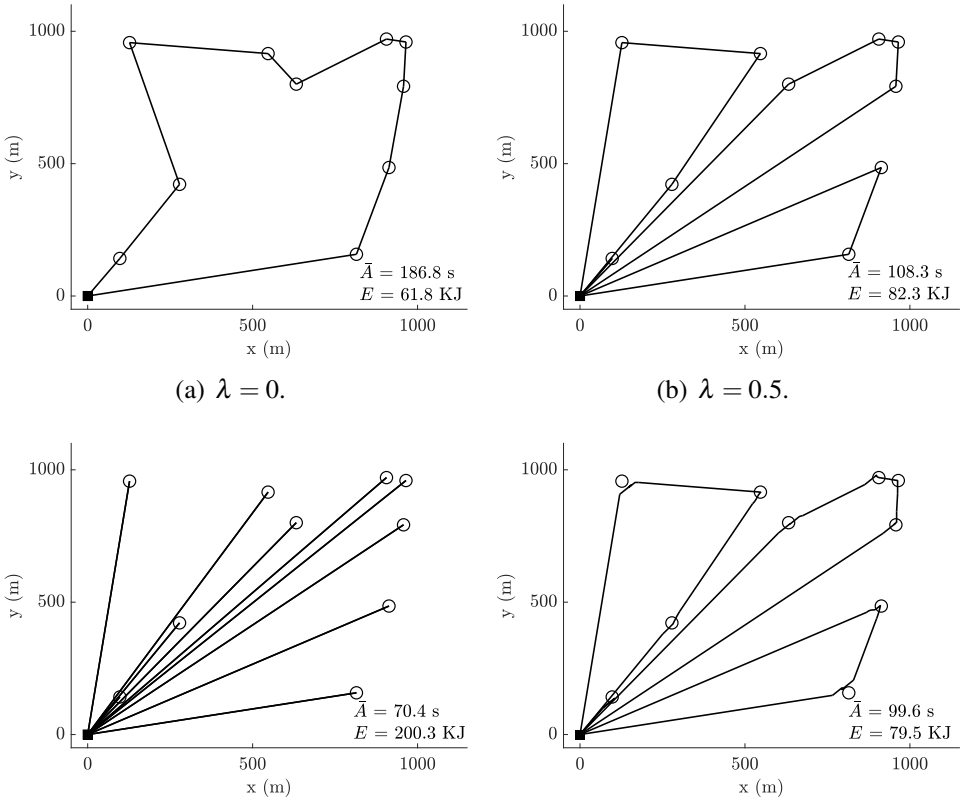

(a) $\lambda = 0$. (b) $\lambda = 0.5$.

(c) $\lambda = 1$. (d) $\lambda = 0.5$, optimised by Algorithm 3.

Fig. 3.4 Comparison of the trajectories as well as $\overline{A}$ and E with different weights λ. Small circles denote SNs and the square represents the depot.

allowed to communicate while flying, it does not need to reach the exact SN location. Instead, it would fly along a trajectory within the coverage area to achieve the better $\overline{A}$ and E.

Fig. 3.5 compares the proposed multi-return-allowed mode (setting $\lambda = 0.5$) with the framework studied in [22], in which the UAV returns to the depot only after all SNs have been visited, as well as the TSP solution. Firstly, comparing the three serving modes under the fly-hover-communication assumption, denoted by red, blue and yellow lines, it can be observed that the proposed multi-return-allowed mode can decrease $\overline{A}$ significantly at the cost of a larger E. Numerically, take the $K = 10$ as an example, the mode in [22] decreases $\overline{A}$ by 4% at the cost of 4% more energy consumption when compared with the TSP solution. Furthermore, the proposed framework shows a 51% gain in $\overline{A}$ than mode [22] with a 37% higher energy consumption. Secondly, comparing the path initialised by (3.7) and the trajectory optimised by (3.17), it can be seen that both the $\overline{A}$ and E are further improved when

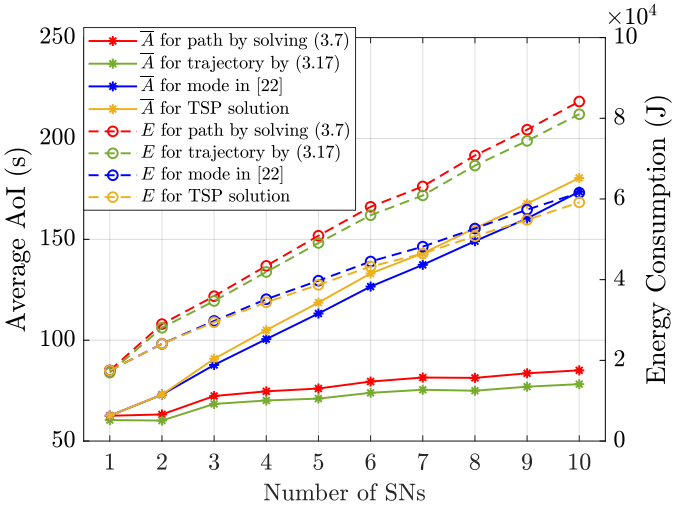

Fig. 3.5 Comparing $\overline{A}$ and E for different serving modes.

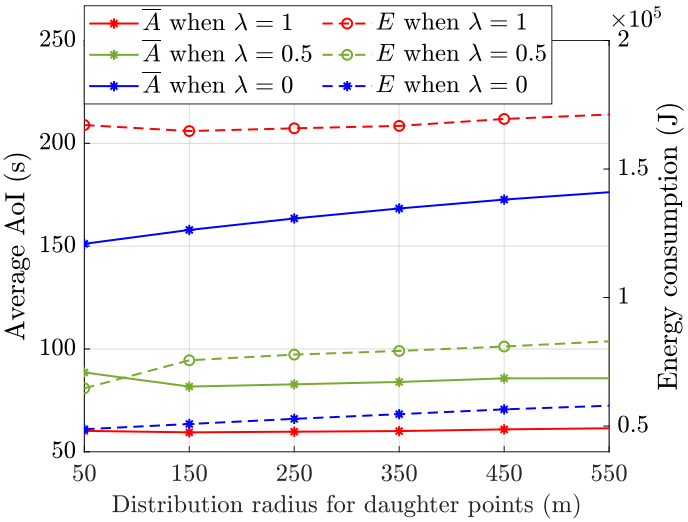

Fig. 3.6 Comparing $\overline{A}$ and E for different SN distributions.

the UAV can communicate while flying. For instance, $\overline{A}$ and E decrease by 8% and 4% respectively in the optimised trajectory when $K = 10$.

In Figures 3.3 to 3.5, all SNs are assumed to follow the normal distribution. However, in practice, SNs often aggregate in hotspots to gather more valuable information, thus showing heterogeneity in the spatial domain. In Fig. 3.6, the Matérn cluster process is used to capture the spatial heterogeneity of SN distribution [106]. The Matérn cluster process is a doubly Poisson cluster process, where parent points are first generated according to a Poisson process with a density of 2 parent points per km^2, and then 10 daughter points (representing the SNs) are generated uniformly in the circles with the radius r around parent points. Increasing this

distribution radius r results in a sparser SN distribution and vice versa. The numerical results in Fig. 3.6 are averaged over 1000 Monte Carlo simulations. Firstly, when setting $\lambda = 0$, problem (3.9) converges to the TSP problem, where the UAV follows a Hamiltonian path and returns to the depot only once. In such cases, increasing the sparsity of SN distribution results in a monotonically increasing AoI and energy consumption, as shown by the blue lines in Fig. 3.6. However, when setting $\lambda = 0.5$ and $\lambda = 1$, there is no monotonic relationship between system performance and SN distribution because the UAV needs to return to the depot multiple times to offload the collected data. In practice, there are often a group of UAVs performing data collection tasks, and ground SNs often follow such homogeneous distributions and are associated with a specific UAV for data offloading. Recalling the results in Fig. 3.6, determining the association strategy based on SN distribution is crucial because the SN distribution shows a non-monotonic and complex impact on system performance.

Moreover, compared with previous works [22, 23, 91], a significant contribution of this work is proposing a MILP formulation for the AoI-aware UAV path planning problem. Notably, although the path planning problems are always NP-hard, proposing a MILP formulation allows us to solve it efficiently by commercial solvers, such as Gurobi [67], and handle it decentralised by some decomposition techniques, such as Bender's decomposition shown in Section 3.3.2. Section 3.2.2 illustrates that the proposed flow-based formulation can be extended to characterise the problem studied in [22] by changing one constraint. Table 3.2 compares the solving time between Gurobi and dynamic programming (DP) proposed in [22], which both achieve the optimal solution of the AoI-aware Hamiltonian path planning. The results presented in Table 3.2 are implemented on MATLAB R2020b and solved by Gurobi 9.1.2[67], running on a Windows 7 with Intel-i7 2.50 GHz and 8 GB RAM. It can be seen that solving by Gurobi shows a significant gain in the running time of than DP method when the number of SNs is greater than 8.

3.6 Conclusion

This chapter studies the path planning problem of a UAV-assisted data collection task, in which two inherently competing metrics, namely the average AoI and the aggregate energy consumption, are optimised jointly. To characterise the trade-off between those two performance metrics and reveal the Pareto frontier, a multi-return-allowed serving mode is proposed, in which the UAV is allowed to return to the depot

Table 3.2 Comparing the solving time by Gurobi and dynamic programming (DP) in seconds.

Number of SN	Example 1		Example 2		Example 3	
	Gurobi	DP	Gurobi	DP	Gurobi	DP
2	0.81	0.01	0.95	0.01	0.75	0.01
3	0.96	0.01	0.88	0.01	0.85	0.01
4	0.96	0.01	0.91	0.02	0.93	0.01
5	0.99	0.15	0.94	0.10	0.93	0.10
6	1.03	0.29	0.91	0.27	0.97	0.29
7	1.75	1.10	1.13	0.98	1.65	1.13
8	1.99	8.21	1.53	8.15	1.68	8.73
9	63.92	125.98	53.34	131.00	49.81	124.90
10	174.78	266.52	142.60	282.43	165.62	278.70

at any instance during the service cycle and formulate it as a multi-objective MILP with a flow-based constraint set. The two objectives are combined into a single one through the weighted linear combination technique, and Bender's decomposition is applied to decentralise the overall computational burden. Subsequently, a more general trajectory in which the UAV can communicate while flying is studied to further improve both these metrics. Additionally, previous research works that solely focus on Hamiltonian paths can be considered as a special case of the proposed approach since it allows multiple returns to the depot during a serving cycle. A wide set of numerical investigations reveals that the proposed multi-return-allowed mode unveils the trade-off between the two competing metrics and hence, provides non-dominated solutions for advanced decision-making.

Chapter 4

Preliminaries of Robotic Aerial Base Stations

4.1 Introduction

As reviewed in Chapter 2, aerial base stations (ABSs) mounted on airborne platforms, such as unmanned aerial vehicles (UAVs), exhibit increasing potential in 6G cellular networks thanks to their functionally flexible deployment and three-dimensional manoeuvrability. ABSs could be utilised to play a vital role in a wide range of wireless systems, such as micro base stations (BSs), relays, data collectors and moving anchors for localisation. Although ABSs have attracted significant attention from both academia and industry in recent years, the limited endurance restricted by the capacity of the onboard battery is still a critical issue. This issue becomes particularly pronounced when ABSs are intended to offer daily mobile data service rather than just being used for short-term sporadic emergency communications. With this in mind, the prototype of robotic aerial base station (RABS) with anchoring capabilities via robotic manipulators [107] is developed to allow for a massive improvement in providing long-term wireless connectivity compared to hovering/flying ABSs. More specifically, by taking advantage of grasping capabilities [108], RABSs can attach autonomously to lampposts or other tall urban landforms via energy-neutral grasping to serve as small cells for multiple hours or even longer. This is in contrast to the flying/hovering endurance for the small-size rotary-wing UAVs acting as small BSs which is less than an hour.

Growing effort has recently been devoted to overcoming the endurance issue of ABSs by developing novel prototypes. The wireless power transfer (WPT) technique is a potential technique to power the ABSs without needing to interrupt the service,

with recharging in the ground stations. In [109], the free space optics (FSO) beam is proposed to recharge ABSs via the WPT technique. However, the energy transfer efficiency of FSO is greatly affected by environmental factors, e.g., when an ABS is located at an altitude of 1 km, the link margin is 38 dB in clear weather in contrast to -15 dB on a foggy day. In [110, 111], high-energy laser beams transmitted from a ground station are utilised to power the ABSs. Theoretically, the laser-powered ABS can provide an unlimited serving time when it is close enough to the charging station to maintain a safe energy level. The authors of [112] utilise a tethered UAV to carry an ABS, in which system a tether linking the UAV with a ground BS could transfer both data and power simultaneously. Although tethered UAVs can communicate with ground devices without the need to recharge, this seamless connection comes at the expense of limited flexibility since the flying range of tethered UAVs is restricted by their BS being located either on the ground or on a rooftop. Moreover, Nokia Bell Labs developed a landing-based ABS prototype named F-cell [3], to satisfy emergency communication requirements. The F-cell can be carried and transported by a UAV and then dropped on rooftops or other easy-to-land platforms to offer wireless service. Each F-cell is equipped with a solar panel to provide the processing energy and a 64-antenna massive MIMO array to enhance the wireless backhaul capacity. However, the F-cell requires a flat area to take off and land (i.e., a rooftop) thereby significantly restricting its operational capabilities, whilst facing severe safety challenges since it is not fixed to the surface. Notably, RABS can be deemed as autonomous robots that can safely grasp in wide set of different tall urban landforms by utilizing robotic manipulators. Besides, unlike the F-cell that is transported and relocated by a UAV, RABS can respond to communication requirements more flexibly and quickly thanks to its inherent flying ability. Fig. 4.1 compares the proposed RABS prototype with hovering-based, laser-powered and tethered ABSs. It also depicts the fulfilment of the 'Impossible Triangle' achieved by RABSs since they can achieve at the same time flexible deployment, energy efficiency and high endurance in providing wireless connectivity.

Considering the functional movable ability and energy efficiency, a wide range of possible use cases for robotic small cells in dense urban areas are envisioned to assist towards the aim of network densification. Firstly, considering the low data rate of cell-edge users and the high possibility of BSs being overloaded during unexpected crowded events, i.e., congestion episodes, RABSs can be deployed on-demand as micro BSs or relays to significantly enhance the network capacity and/or extend the cell coverage effectively. Secondly, in next-generation cellular networks, new radio applications always place more extensive and stringent requirements on

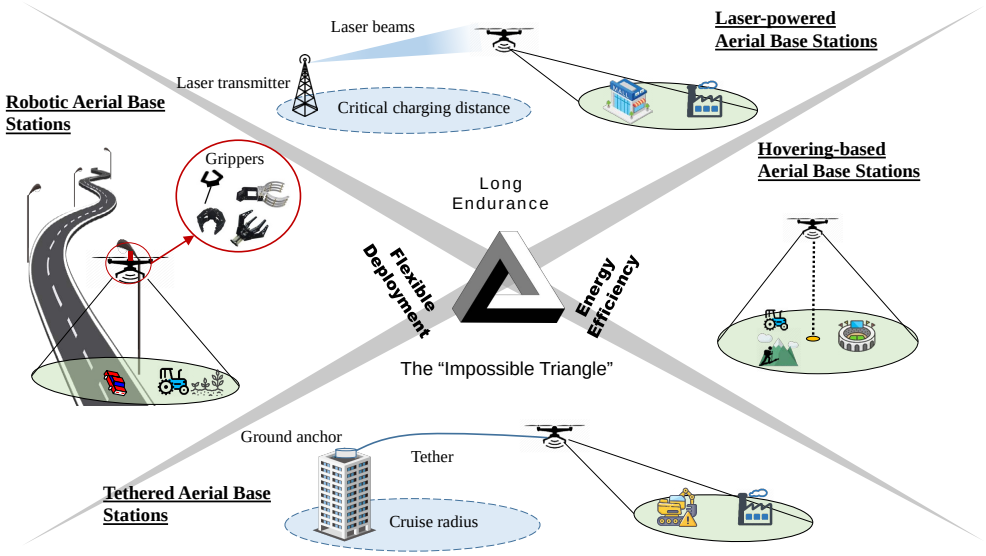

Fig. 4.1 Comparing the RABS prototype with other types of ABS: The "Impossible Triangle" achieved by robotic aerial base stations since this concept manages to simultaneously achieve three fundamental operational capabilities.

communication systems, in which cases RABSs can be utilised to satisfy these new radio applications, e.g., RABSs attached to lampposts can act as road side units to offer low-latency and high-reliable service in intelligent transportation systems. They can also be installed with edge computing or caching modules to alleviate the overload and congestion in cloud servers in case of congestion episodes. Thirdly, RABSs can cooperate with other types of non-terrestrial nodes located at different vertical platforms, such as high-altitude platform stations (HAPSs) as well as satellites, and provide wireless access from the side closer to ground users.

4.2 System Architecture

4.2.1 A Primer Hardware Design

The recent development in multi-rotor UAVs enables ABSs to perform a wide range of operations in a controllable manner, i.e., flying along a predefined route, hovering at a specific location and cooperating with other ABSs. According to their aero-mechanical design, UAVs can be classified into fixed-wing and rotary-wing UAVs. Because small-size rotary-wing UAVs are able to take off and land on various types of urban platforms and yield more flexible operations, they can be chosen to carry and transport the RABSs. The hardware design of RABS is illustrated by Fig. 4.2, which

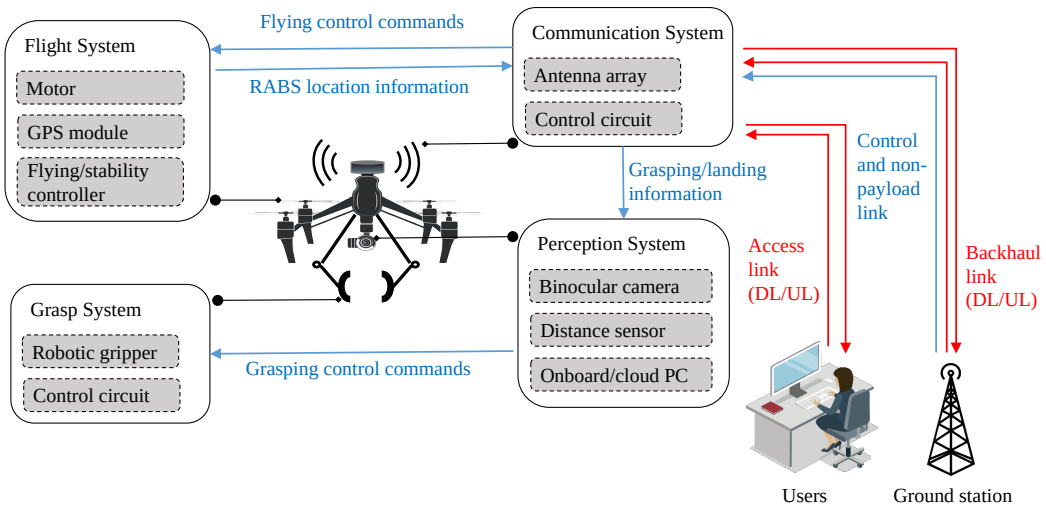

Fig. 4.2 Hardware structure of the designed RABS prototype.

includes four subsystems to perform different operations, i.e., flight, communication, grasp and perception systems.

Unlike conventional ABSs, a robotic gripper is mounted on the RABS so that it can grasp different urban landforms, such as lampposts and rooftops in a flexible and safe manner. In [113], robotic grippers are classified into several categories via different classification strategies. Specifically, grippers can be divided into four categories according to the number of fingers, i.e., 2-finger gripper, 3-finger gripper, 4-finger gripper, and anthropomorphic hand. The finger design is always determined by the contacting surfaces with the objects when performing the grasping operation. Inspired by the fact that nearly 60%-70% of human grasping actions of objects with parallelepiped, pyramidal, and cylindrical shapes can be operated by two fingers, the 2-finger gripper is the most popular design for practical industrial applications [113]. According to the type of actuation used, grippers can be classified as vacuum, magnetic, hydraulic, pneumatic and electric types. Considering the RABS is battery-powered and the contacting surface of typical landforms (e.g., lampposts) is usually metal, electric or magnetic (or electromagnetic) grippers might be employed by RABS as well. According to the grasping method, grippers can be divided into four categories, i.e., impactive, ingressive, astrictive and constitutive grippers, which should be determined by the shape of target objects as well as the operation requirements. The required force to hang the RABS to a lamppost via a 2-finger gripper is calculated by Eq. (1) in [107]. Taking the DJI Matrice 300 RTK

UAV with a weight of 6.3 kg as an example, the force requirement from the gripper should be 1234.8 N in the worst case.

4.2.2 Workflow of Robotic Aerial Base Stations

In order to deploy RABSs at suitable locations to adapt to the traffic dynamic in both spatial and temporal domains, a central controller needs to monitor the changes in traffic in real-time, and timely send commands to RABSs that they need to relocate their positions. Once the RABS receives the control signal from the ground control stations and decides to grasp at a certain location, it is required to fly to this target point and grasp reliably. To achieve this task, RABS should be equipped with a variety of onboard sensors to control its localisation, velocity and attitude via global navigation satellite system (GNSS) and Radar/Lidar-based localisation techniques. Furthermore, to complete the grasping function at a chosen location autonomously, real-time object detection capability is required in the RABS. Fortunately, thanks to the recent development of deep learning methods, UAVs can perform autonomous and real-time grasping precisely via vision-based and AI-aided approaches. Take the UAV prototype with grasping ability designed in [108] as an example. For the hardware design, a computer deployed in the ground station is used to offer enough computational capacity for vision measurements and a downward-looking binocular camera is mounted onboard to recognise the grasping target. For the software structure, the Yolo3 algorithm is employed to perform the object detection, which includes three steps, i.e., collect and label samples, train the neural network and test the trained model. The developed UAV prototype is then able to perform the grasping task accurately. Note that since RABS will be part of the 5G and beyond network infrastructure, those computationally heavy tasks could potentially be offloaded to suitable edge clouds instead of an extra computer.

4.2.3 Wireless Access, Backhaul and Non-payload Links

In this section, the spectrum design for both access, backhaul and non-payload links of RABSs are discussed. For the access link, RABSs can communicate on high-frequency bands, such as mmWave or sub-THz, to support extremely high-capacity networks via network densification and ultimately enable novel applications with multimodalities. Operating the RABSs on the high-frequency bands has the following two benefits. Firstly, it could avoid the interference with the existing communication systems operating on the low frequencies. Secondly, because carriers on these high

frequencies are always characterised by very high path loss in non-line-of-sight (NLoS) conditions, RABSs can be carefully deployed to improve the line-of-sight (LoS) probability thanks to their high flexibility. To characterise the urban micro BS propagation working on these high-frequency carriers, the large-scale path loss of 28, 38, 73 and 143 GHz is measured in [114]. Notably, all of the results in [114] are measured on the urban micro BSs placed at an altitude from 4 m to 36 m above the ground, thus, the proposed path loss model can be employed for RABSs straightforwardly. For instance, the micro cell TX working at 143 GHz is located at a height of 4 m above the ground (similar heights as lampposts) and the measurements show that it can provide up to 117.4 m coverage in the outdoor urban area for both LoS and NLoS scenarios [114].

As shown in Fig. 4.2, in addition to providing wireless access to users, RABSs also establish wireless connections with ground base stations for the following two purposes. On the one hand, to safely execute operations such as flight, landing, and grasping, RABSs should receive essential safety–critical information and operational commands from ground stations, such as air traffic information, control commands from remote pilots, and positional data of the target grasping points. This link is commonly known as the control and non-payload link. Due to the catastrophic consequences of this link interruption, potentially resulting in the loss of control of UAVs, the International Civil Aviation Organisation has mandated that the control and non-payload link must operate over protected aviation spectrum [115]. For example, the *C*-band spectrum at 5030–5091 MHz has been allocated for UAV non-payload links during the World Radiocommunication Conference (WRC)-12 [81]. These frequency bands can also be utilised for transmitting control commands to RABSs.

On the other hand, RABSs could also communicate with ground base stations via the wireless backhaul link. It is worth noting that while non-payload links only require a relatively small data rate to transmit limited information, the backhaul links require a large capacity to enable RABSs to provide wireless coverage to as many users as possible. Numerically, as investigated in [81], non-payload links require a throughput of kilobits per second while the backhaul links should serve dozens of gigabits per second to process high-quality applications. With this in consideration, two potential approaches could be used to enhance the capacity of backhaul links. Firstly, RABSs can connect with the macro BSs on the high-frequency bands to guarantee the backhaul requirements. Besides the aforementioned mmWave and sub-THz, free space optics (FSO) can also be employed for the backhaul links because the RABSs can adjust the position flexibly so that their backhaul links to the

macro BSs (always placed at heights of 15-50 m) will not be blocked by obstacles. Having a future vision, HAPSs, deployed at altitudes in the range of 20 to 50 km, could be utilised as the macro BSs while connecting with the small cells (i.e., ABSs, RABSs, urban micro BSs, etc.) on the FSO beams [109]. Secondly, by mounting a multi-antenna array on the RABS, the capacity of backhaul links can be improved via MIMO techniques, which have been applied in the Nokia F-cell.

4.3 Ideal Attributes of Robotic Aerial Base Stations

In this section, four key attributes of RABS-assisted wireless systems are illustrated that can be deemed as advantages compared with other aerial platforms used for communications.

1) Network densification without densifying the infrastructure: To deal with the rapidly growing volume of traffic demand, one promising technique is network densification, i.e., deploying a large number of small cells densely. However, as measured by [116], the traffic distribution in urban regions shows high inhomogeneity in both spatial and temporal domains. Due to this inhomogeneous traffic distribution, network densification via densifying the wireless nodes may cause significant waste in both capital expenditure and operating expenditure. In contrast, RABS provides an alternative approach for low-cost and flexible network densification. More specifically, RABSs could be deployed in hot spot regions and transported to other peak traffic areas by following the temporal traffic dynamic as it unfolds. In that sense, network densification via RABS could ensure capacity is always targeted at the specific locations and times when it is most needed. In other words, compared with terrestrial micro BSs, RABS show a higher flexibility thanks to their mobility which allows them to follow the spatio-temporal traffic variations as they unfold.

2) Overcoming the ABS endurance issue: As one of the initial motivations, the serving endurance of RABSs can be multiple hours or even longer, compared to the hovering/flying time of conventional ABSs which is always less than one hour. Fig. 4.3 compares the power of different modules in ABS and RABS. The first three bars represent the propulsion power of different UAVs. As summarised in Appendix A, the propulsion power of UAVs is a function of their flying speed and is also affected by hardware design and environmental factors. To provide an intuitive comparison, the propulsion power values in Fig. 4.3 are calculated based on typical flight speeds and common environmental factors for UAVs. Specifically, the first bar shows the flying power of rotary-wing UAVs in hovering mode [27], the second bar represents

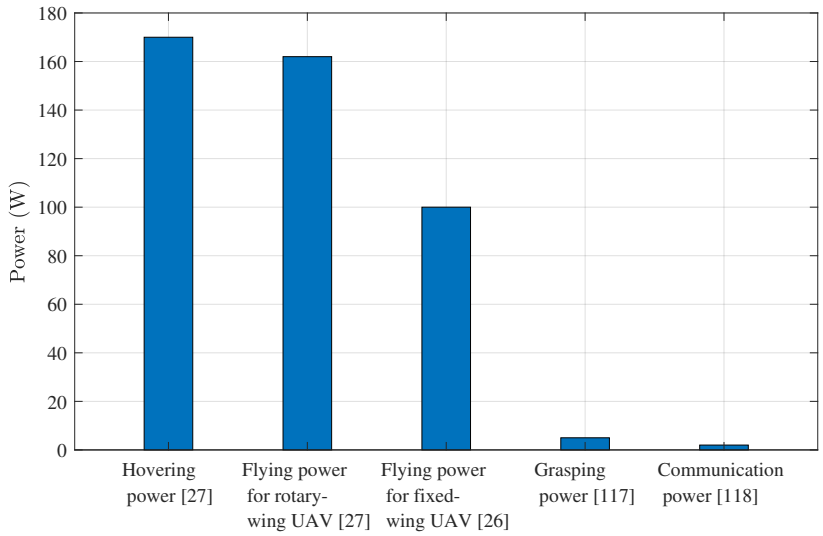

Fig. 4.3 Comparing different types of power.

the propulsion power of rotary-wing UAVs at the optimal speed that maximises total flying distance [27], and the third bar indicates the minimum propulsion power of fixed-wing UAVs [26]. Further discussions on the propulsion power can be found in Appendix A. Additionally, the fourth and fifth bars represent the grasping and communication power of RABSs, as measured in [117] and [118], respectively. It is worth noting that Fig. 4.3 takes typical values for comparing the power consumption across various ABS operations, while these values may vary depending on actual hardware configurations and environmental conditions. Comparing the hovering, flying and communication power, it can be observed that the propulsion power is much more significant than the communication-related counterpart during the ABS serving endurance. Moreover, noticing that the grasping power is almost 16 times less than hovering and flying power, RABSs, which provide service when grasping at urban landforms, certainly have a longer lifetime than conventional ABSs. Most importantly, it should be noted that the specialised dexterous grippers can be designed that operate in an energy-neutral manner, in which case the perching energy consumption can be completely eliminated.

3) Adapting to harsh weather conditions: One of the most critical issues when operating UAVs is harsh weather conditions, such as rainstorms, strong winds, and extreme temperatures. These weather conditions can impact flight safety in various scenarios. Heavy rain, snow and other water might cause the onboard motors to stop and pose a threat to UAV flight safety. Flying or hovering in windy environments consumes more energy to control the UAV and sometimes is even impossible to

Table 4.1 Noise Emission of DJI Matrice 600 Pro

UAV status	Altitude (m)	Lateral distance (m)	Noise (dB)
Hovering	9.18	0	89.6
		2.45	88.7
		5.28	87.3
		9.14	83.7
		15.84	79.2
Flying (3.23 m/s)	7.5	0	85.3
		2.45	84.0
		5.28	82.7
		9.14	79.6
		15.84	75.9

take off. Furthermore, vision-based operations, such as monitoring and sensing, can be affected in foggy weather. In most of these cases, grasping-based RABSs can provide services in a significantly safer manner due to their anchoring capability, which can be summarised as rainproof and windproof.

4) Low-noise operation: The number of UAV-assisted applications has grown significantly in recent years, such as cargo delivery, environmental monitoring, smart agriculture and wireless communication. Within that context, UAVs are regarded as a new source of environmental noise pollution and are starting to attract increasing attention from researchers. As shown in Table 4.1, the authors of [119] measure the noise emission of DJI Matrice 600 Pro when flying and hovering. It can be seen that the noise generated by UAVs operating at a low altitude is very close to the so-called Acceptable-Noise-Level (ANL) which is at 85 dB. Furthermore, recalling that the free-field sound decay rate is at approximately 6 dB with a doubling of the distance, the UAV operating at the highest permitted altitude of 120 m would still produce nearly 50 dB of noise pollution. Note that the limits for urban ambient noise are at 45 dB during the night and at 55 dB during the day. Therefore, noise pollution is a critical and real issue when applying ABSs in urban areas, especially when considering public acceptance. However, when RABSs anchor at lampposts and switch off their rotors, they can provide zero levels of noise emission and are thus more suited for urban applications.

4.4 Case Study I: Comparing with Terrestrial Networks

As mentioned in Section 4.3, one of the main advantages of RABSs lies in their controllable mobility, which brings increased flexibility and agility to cellular networks. However, the design of RABSs, as illustrated in Section 4.2, limits their connectivity with the macro base station (MBS) to a wireless backhaul link with limited capacity, unlike the high-capacity fibre link used by ground BSs. This section studies a heterogeneous network (HetNet) configuration comprising an MBS and an RABS connected by a wireless backhaul link with limited capacity. The objective is to highlight the extent to which RABSs can enhance the performance of cellular networks.

Consider the downlink case in a HetNet consisting of an MBS and an RABS deployed as a small cell. The geographical area under consideration is $1 \times 1\,\text{km}^2$, with 121 candidate locations evenly distributed throughout the area. Thanks to the flying and grasping capabilities, the RABS can autonomously select and establish wireless connections with ground users by dynamically selecting one of the candidate locations. Moreover, the out-of-band relaying protocol is utilised in this HetNet, i.e., the accessing link connecting the users with BSs and the backhauling link between the RABS and MBS are conducted in orthogonal channels. Assume that there are 20 orthogonal subcarriers with a bandwidth of 180 kHz for accessing connection, and the backhauling link has a bandwidth of 700 kHz. The transmission power for MBS and RABS is set to 3 W and 1 W, respectively. Besides, one user can be provisioned by one or multiple subcarriers while one subcarrier can only be assigned to at most one user to avoid intra-cell interference. The path loss model follows the results shown in 3GPP [120], that is, $128.1 + 37.6\log_{10}(d)$ and $140.7 + 36.7\log_{10}(d)$ for the path loss in macro and small cells, respectively, where d is the distance between BSs and users in kilometres. For the wireless backhaul channel, the path losses are $100.7 + 23.5\log_{10}(d)$ and $125.2 + 36.3\log_{10}(d)$ for line-of-sight (LoS) and non-line-of-sight (NLoS) links, respectively. The LoS probability is calculated by $\min(0.018/d, 1)(1 - \exp(-d/0.072)) + \exp(-d/0.072)$.

Taking fairness into consideration, the minimum rate among all users is maximised by optimizing the following three decisions: Firstly, the RABS selects one of the candidate locations to grasp when providing wireless connections. Secondly, whether each user should be associated with the MBS or RABS is determined. Thirdly, available subcarriers are allocated for accessing links. The problem is formu-

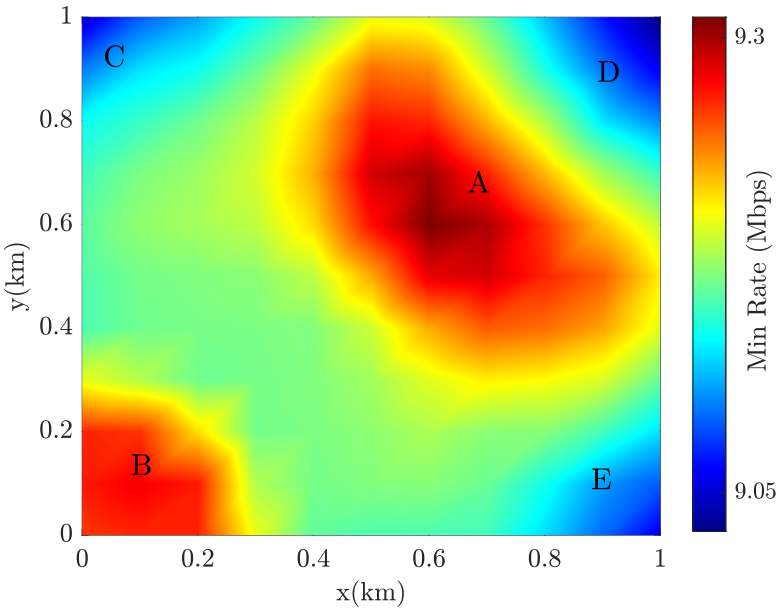

Fig. 4.4 Minimum data rate versus RABS locations.

lated as a binary polynomial optimisation problem and solved using a semidefinite relaxation-based heuristic method as proposed in previous work [121].

Assuming there are 10 users distributed randomly and the MBS is located at the origin point, Fig. 4.4 presents the minimum data rate versus different candidate locations via 100 Monte Carlo simulations. The best RABS deploying area denoted as area A, is located at the centre of the macro cell edge to cover most of the cell-edge users. In contrast, when the RABS is placed in the corner areas C, D and E, the system performance is the worst because the RABS cannot cover most of the cell-edge users. For example, if the RABS is deployed in area C, it cannot connect with the users in areas D and E, which typically have low data rates because they are far from the MBS. When the RABS is placed near the MBS, denoted as area B, although it is far from the cell-edge users, the backhaul capacity increases, resulting in another peak. Hence, region A can be considered the operational area for the RABS, allowing it to change its perching point on lampposts located within that area.

To demonstrate the impact of RABS on the cellular network, Fig. 4.5 compares the minimum data rate for different network configurations, i.e., a two-tier network with an RABS deployed following the strategy proposed in [121], a two-tier network with a randomly-deployed small base station (SBS) and a single-tier network with only MBS. It can be observed that the two-tier HetNet could enhance the system performance when $I \geq 3$. However, all types of networks show the same performance

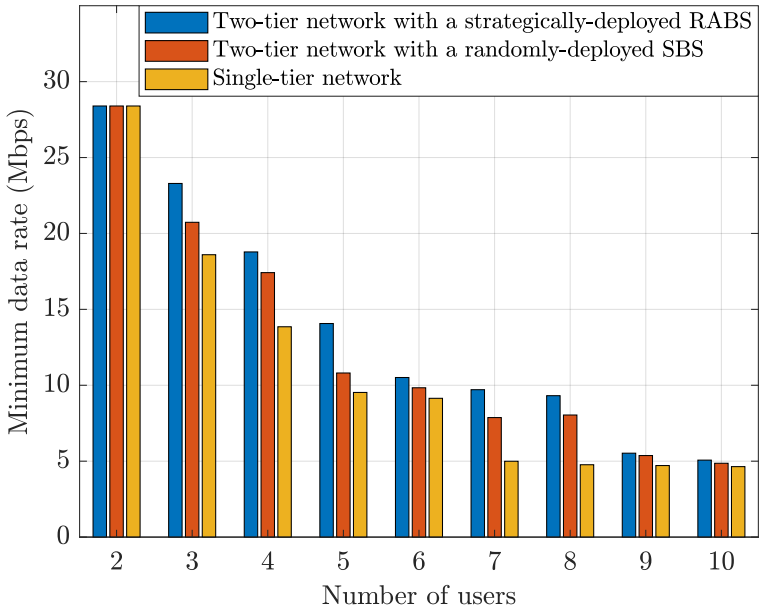

Fig. 4.5 Minimum rate versus number of users.

when $I \leq 2$, as in such cases, the minimum rate is primarily constrained by the limited capacity of the backhaul link, resulting in all users being associated with the MBS. Comparing the two-tier network with a randomly deployed SBS and the single-tier network, it can be observed that deploying an extra SBS significantly enhances the minimum data rate, as the SBS can alleviate the coverage burden of the MBS. However, conventional SBSs are often installed on rooftops and other low-altitude urban platforms, making their positions inflexible, while the controllable movement of RABS compensates for this deficiency. Numerically, comparing two-tier networks with a strategically-deployed RABS and a randomly-deployed SBS, it can be seen that the minimum data rate can be improved by up to 36%, as the RABS can be deployed near cell-edge users and improve system performance. In conclusion, this case study provides compelling evidence that the implementation of RABS significantly enhances the minimum data rate of cellular networks, thanks to its inherent flexibility and agility.

4.5 Case Study II: Comparing with Other Types of ABS

As reviewed in Section 4.1, several novel prototypes of ABS have been recently developed to overcome the endurance issue. To better clarify the benefits of the RABS pointed out above, it is compared with the following three types of ABS:

- Hovering-based ABS is the conventional ABS that can provide wireless service when hovering and change its location freely. However, one of the main challenges is that due to the limited battery capacity, hovering-based ABSs need to fly back to charging stations periodically and recharge via drone swapping or battery swapping strategies [122].

- Tethered ABS is an ABS that is connected with a ground anchor by a physical cable or tether [112]. The physical link brings ABS an unlimited serving endurance. However, this comes at the cost of reduced mobility so tethered ABS can only serve users distributed near the ground anchor.

- Laser-powered ABS is another type of ABS having unlimited endurance in theory [110]. High-power laser beams transmitted from ground laser directors are used to power ABSs when hovering and flying. Although these wireless laser beams can power ABSs from a longer distance than physical tethers, the cruise range of laser-based ABSs is still limited within a ball centred around the ground laser transmitter to guarantee a safe energy level. The maximum radius of this cruise range is named as critical charging distance [111].

Initially, the coverage performance of these four types of ABSs is compared. Assuming 100 users are distributed randomly over an area of 2 km by 2 km, the problem investigated in [96] is employed as the simulation scenario, where ABSs are positioned to cover as many ground users as possible. Successful covering is defined as users experiencing path loss values lower than a predetermined threshold of 118 dB. The air-to-ground channel model proposed in [96] is employed to calculate the path loss value for hovering-based, tethered, and laser-powered ABSs. However, because RABSs tend to be deployed at lower altitudes (such as lampposts) having a higher probability of being blocked, the 3GPP path loss model for urban small cells is applied for RABSs' coverage area [120]. Assume that hovering-based, tethered, and laser-powered ABSs are hovering at the altitude of 100 m when providing wireless service, and the detailed constraints for different types of ABS are clarified as follows. Hovering-based ABS can be deployed freely to cover as many users as possible; this

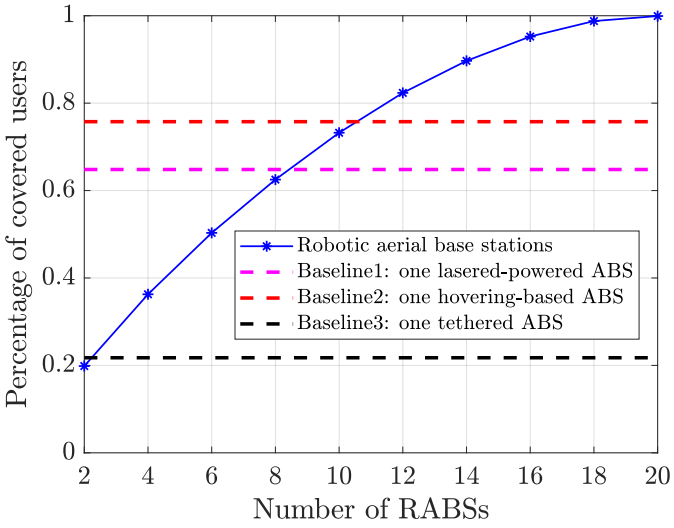

Fig. 4.6 Comparing the coverage performance for different types of ABS

problem has been studied in [96]. Moreover, the flying range of tethered ABS is limited by a 150 m cable linked with a ground anchor located at the origin point. Setting the laser transmission power to 800 W, the critical charging distance of laser-powered ABS can be calculated by Eq. (10) in [111]. To simulate the grasping-based deployment for RABSs, it is assumed that a lamppost is distributed every 100 m which is suitable for RABS grasping. RABSs can select a subset of these lampposts to grasp when providing wireless service to nearby ground users.

Averaged over 100 Monte Carlo simulations, Fig. 4.6 compares the coverage performance of RABSs with other baseline schemes, i.e., hovering-based, tethered and laser-powered ABSs. As expected, with an increase in the number of RABSs, the coverage improves. It can be also observed that a single laser-powered ABS and hovering-based ABS perform nearly as well as 8 and 10 RABSs, respectively. Besides, Fig. 4.6 also shows that the deployment of 20 RABSs can cover all ground users. Although RABSs require a denser deployment to achieve a high coverage probability, this should be considered in the context of the following result: even a swarm of 10 RABSs still offers significant energy savings compared to other types of ABS.

Fig. 4.7 compares the energy consumed by a swarm of RABSs with hovering-based, tethered and laser-powered ABSs when operating for 24 hours. The energy consumption for RABSs includes three parts, propulsion, anchoring and communication. RABSs are equipped with two types of grippers, a nominal energy-consuming gripper consuming 5 W and an energy-neutral gripper. The hovering and flying power is set to 170 W and 162 W, respectively [27], and the communication power

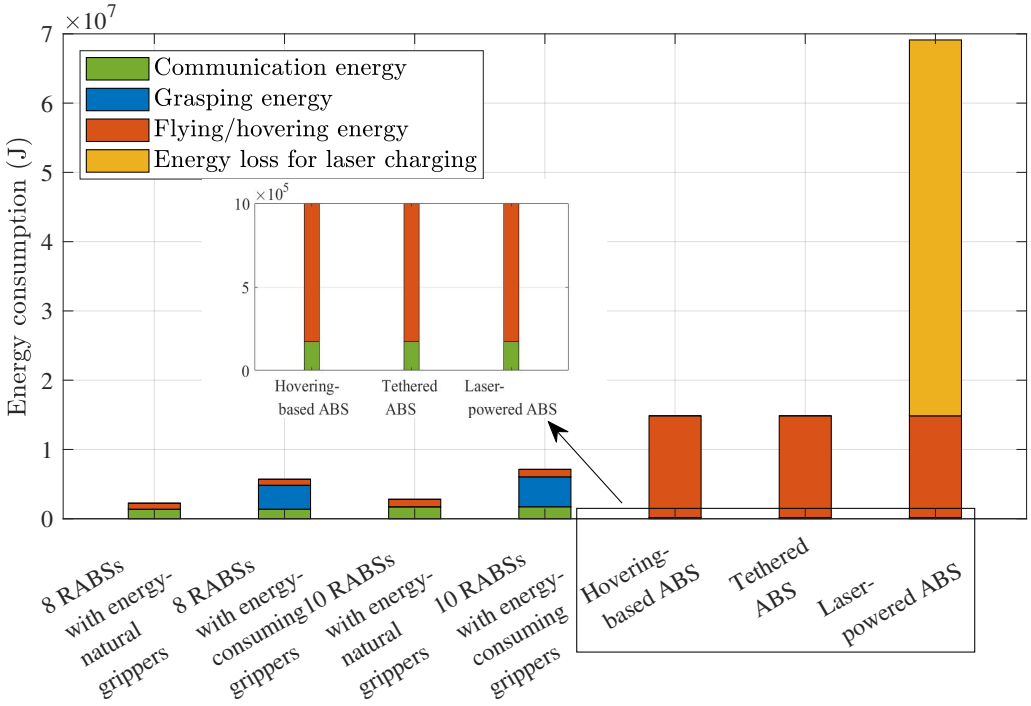

Fig. 4.7 Comparing the energy consumption for different types of ABS

is assumed to be 2 W [110]. To simulate the RABSs periodical relocating, it is reasonable to assume that half of the RABSs need to fly 500 m every hour to update the network topology. It should be pointed out that the reason for setting the moving distance as 500 m is that when an RABS needs to relocate to a farther lamppost, another RABS that is closer to moving to this position can always be found. The results depicted in Fig. 4.7 show that when equipping with the energy-neutral grippers, a swarm of 8 RABSs is more than 30 times more energy efficient than a laser-powered ABS for the same network coverage. Compared to tethered ABS and hovering ABS, a group of 10 RABSs are more than 6.6 and 5.3 times energy efficient respectively when providing the same level of wireless coverage. Besides, since the energy consumption for ABSs during hovering and flying is affected by environmental factors, e.g., more energy is needed to maintain stability in high winds and rainfall, in practice RABSs should show more energy gain because of their environmental independence, as illustrated in Section 4.3. Moreover, it is worth pointing out that although hovering-based ABS and RABSs cannot operate for such a long period due to the battery capacity limitation, in order to ensure a fair comparison, they are assumed to be able to be swapped and recharged to prolong the serving endurance [122]. Assuming that the capacity of the onboard battery is 6700 mAh and the nominal voltage is 14.8 V [110], it can be calculated that the hovering-based ABS

has to be recharged 41 times, while each RABS only needs to be recharged once when equipped with the energy-neutral grippers.

4.6 Conclusion

Robotic aerial base stations (RABSs) equipped with dexterous end effectors able to grasp onto tall urban landforms can introduce significant degrees of flexibility for network densification in future 6G networks. In this chapter, the system architecture of RABSs including both hardware design and communication considerations is discussed by gearing two previously disconnected areas, namely non-terrestrial communications and robotic dexterous end effectors with grasping capabilities. Afterwards, the RABS is demonstrated to provide long-term and flexible wireless service in an energy-efficient, weather-independent and environmentally friendly manner, following which two case studies are proposed to compare RABSs with terrestrial base stations and other types of ABSs in terms of coverage and energy performances.

Chapter 5

Optimal Deployment and Operation of Robotic Aerial Base Stations

5.1 Introduction

As illustrated in Section 4, robotic aerial base stations (RABSs) with grasping capabilities are developed to overcome the endurance issue of conventional aerial base stations (ABSs) and can provide relative long-term wireless connectivity in an energy-efficient way. More specifically, taking advantage of the grasping capabilities [117, 123], RABSs can attach autonomously in lampposts via energy-neutral grasping or land on other tall urban landforms to serve as small cells in urban environments for multiple hours or even longer. Also, compared to conventional ground base stations (BSs), RABSs show increased degrees of freedom which means they can change their grasping locations to better explore the spatial-temporal dynamic of the traffic load in real-time scenarios and hence increase the overall network performance [116]. In this chapter, the optimal deployment and operation strategy is investigated to explore the use of RABS from a network perspective.

Moreover, because of the increasing emphasis on green communication in recent years, the sleep mode technique is a potential way to decrease the system energy consumption by switching a subgroup of BSs off during the off-peak time [124]. In [125], the optimal sleeping decision is made on three different sides, that is, micro BS, core network and user sides. The work in [126] studies the energy efficiency performance under two types of sleeping policies, i.e., random and strategic sleeping policies. In [127], by controlling the sleep mode adaptively, the energy consumed by a heterogeneous network (HetNet) is minimised under the guarantee of quality of service (QoS). Similarly, the HetNet sleep strategy is further exploited

through a mathematical optimisation approach and a deep reinforcement learning method in [128] and [129], respectively. In [130], the BS activation decision is made to minimise the system energy with the consideration of the cell association and resource allocation jointly, which problem is solved through the reweighted l_1 minimisation technique. The work[124] reviews the application of sleep mode on the topic of green cellular networks.

As mentioned above, compared to the nominal ground BSs, RABSs show increased degrees of freedom that allow them not only to operate a sleep mode function but also to relocate the grasping points to respond to the spatial-temporal dynamic of traffic load. The main contributions of this chapter are summarised as follows.

- The prototype of RABS is developed to overcome the endurance issue of the conventional ABS, which can be employed to configure a flexible and green cellular network thanks to its mobility and energy efficiency. For an initial exposition from a network perspective, this chapter studies how RABSs operate the two critical binary decisions, i.e., the active/sleep mode of operation and relocating the grasping locations or not.

- An essential insight is explored that the deployment and operation decisions of RABSs are coupled with each other, that is, the RABS only needs to visit the locations where it is active. Based on this analysis, the optimal deployment and operation problem is formulated as an integer linear program (ILP) that aims to maximise the volume of served traffic under the onboard energy constraints. The modelled ILP problem is NP-hard and the scale grows sharply because of complicated and tightly coupled variables.

- To solve the above problem efficiently, a special case with only one RABS is investigated, the formulation of which can be greatly simplified and includes a knapsack type of constraint and a set of totally unimodular constraints. Based on the structure of this formulation, a Lagrangian heuristic algorithm is developed to capture a near-optimal solution in polynomial time. Afterwards, to handle the large-scale multi-RABS problem, a decomposition strategy is proposed based on the minimum-weight perfect matching problem and Hungarian algorithm, which decomposes the multi-RABS case into several single-RABS problems in polynomial time.

The remainder of this chapter is organised as follows. Section 5.2 details the application scenario, based on which the system model and mathematical formulation are proposed. In Section 5.3, a special case with only one RABS in the system is

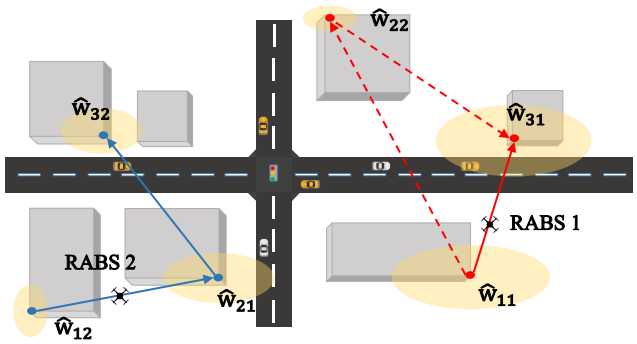

Fig. 5.1 Application scenario: Small dots denote the best two locations at each epoch. Light yellow ellipses represent the traffic demand and its volume is denoted by the area of ellipses. The dotted lines are the RABS flying routes without the onboard energy limitation, while the solid lines denote the flying route of the battery-limited RABSs.

illustrated and solved by a Lagrangian heuristic method, which is developed based on the analysis of the formulation structure. In 5.4, inspired by the graph theory and the Hungarian algorithm, a polynomial-time decomposition strategy is proposed to decompose the multi-RABS problem into several single-RABS problems. A wide set of numerical investigations is illustrated in Section 5.5.

5.2 System Model and Problem Formulation

Hereafter, a certain geographical area with M candidate locations and a wireless system including N RABSs are considered. Denote the Cartesian coordinates of candidate locations by $\mathbf{w}_m \in \mathbb{R}^2$, $m = 1, 2, ..., M$ and discretise the time horizon into T epochs with equal length δ. Within each epoch, the active/sleep status for the RABSs remains unchanged.

In this work, a similar assumption as in [127–129, 131] is made that the traffic patterns can be predicted from the typical experienced/historical data, which would be detailed later in Section 5.2.1. Fig. 5.1 illustrates an example application case with $N = 2$ and $T = 3$. Firstly, choose the best two locations from all candidate locations and depict them by small dots as shown in Fig. 5.1. The i^{th} best location at epoch t is denoted by $\hat{\mathbf{w}}_{ti}$, e.g., $\hat{\mathbf{w}}_{11}$ and $\hat{\mathbf{w}}_{12}$ represent the best and the second best locations at epoch 1, respectively. It should be noted that the best and the second best locations are the candidate locations with the largest and the second largest traffic demands, respectively. Further discussion can be found later in Section 5.2.1. When the energy constraint is ignored, N RABSs would always be able to visit all

chosen locations $\{\hat{\mathbf{w}}_{ti}\}$ to serve the most volume of traffic load. In that case, the flying route is denoted by the dotted lines in Fig. 5.1, where RABS 1 follows the route $\hat{\mathbf{w}}_{11} \rightarrow \hat{\mathbf{w}}_{22} \rightarrow \hat{\mathbf{w}}_{31}$ and RABS 2 passes $\hat{\mathbf{w}}_{12} \rightarrow \hat{\mathbf{w}}_{21} \rightarrow \hat{\mathbf{w}}_{32}$ successively. In contrast, when the battery limitation is taken into account, this ideal policy might be infeasible. In that case, RABSs might need to switch off at some epochs to save energy and wake up at others. For example, in Fig. 5.1, the relatively lower volume of traffic at location $\hat{\mathbf{w}}_{22}$ and long flying distance make visiting this point inefficient in terms of energy consumption. Thus, RABS 1 would wake up at epochs 1 and 3, and switch off at epoch 2. Most importantly, it is worth pointing out that these two operation decisions, i.e., active/sleep mode and relocate the grasping locations or not, are tightly coupled with each other. In other words, the RABS only needs to grasp at the chosen location $\hat{\mathbf{w}}_{ti}$ when it is active at epoch t. As presented by the solid lines in Fig. 5.1, since RABS 1 would be switched off during epoch 2 to satisfy the battery constraints, it does not need to relocate to $\hat{\mathbf{w}}_{22}$ at all. It would remain grasping at $\hat{\mathbf{w}}_{11}$ during epoch 2 and transport to $\hat{\mathbf{w}}_{31}$ directly at the start of epoch 3. These coupled decisions will become more evident in the mathematical programming formulation which is detailed in Section 5.2.3.

5.2.1 Spatial-temporal Traffic modelling

As investigated in [116], the traffic patterns in urban regions show high inhomogeneity in both spatial and temporal domains. Even so, they can still be predicted accurately from the typical experienced data via several existing methods, such as machine learning techniques [132]. Without loss of generality, the spatial-temporal traffic model proposed by [133] is used to characterise the traffic variation pattern in this chapter.

Particularly, the authors of [133] collect real traffic data of 185 base stations over three weeks in a 6 km $\times$ 2.5 km area in one big city in China. The recorded information is the total traffic volume in Byte of each base station and the research area can be divided into three typical regions: park, university campus and central business district (CBD). In the temporal domain, the authors first select traffic data from base stations located in three typical regions, which contain information on time, coordinates, and traffic volume. Then, the variation regularity of average traffic volume in a selected region is analysed to identify the main frequency components via the fast Fourier transform. The temporal traffic model incorporating more frequency components could fit the real data more accurately, albeit at the cost of increased complexity. Therefore, through further analyzing the data in the frequency domain

Table 5.1 Summary of Notations

Symbol	Description
$E^{\text{fly}}_{ti\to t'i'}$	Propulsion energy consumed by the RABS flying from $\hat{\mathbf{w}}_{ti}$ to $\hat{\mathbf{w}}_{t'i'}$
E^{grasp}	Grasping energy consumed by the RABS grasping for an epoch
E^{active}	Communication energy consumed by the RABS being active for an epoch
E^{sleep}	Communication energy consumed by the RABS being sleep for an epoch
E^n	Total energy consumed by the RABS n
$E^{\max}$	onboard battery capacity
M	Number of all candidate locations
N	Number of RABSs
P^{fly}	Propulsion power of the RABS
P^{grasp}	Grasping power of the RABS
P^{tra}	Transmission power of the RABS
P^{active}	Active mode power of the RABS
P^{sleep}	Sleep mode power of the RABS
T	Number of epochs
$V(t)$	Mean traffic volume at epoch t
$V_m(t)$	The traffic volume if an RABS is placed at the candidate location m at epoch t
$\hat{V}_{ti}$	The i^{th} largest traffic volume at epoch t
$\mathbf{w}_m$	The Cartesian coordinates of the candidate location m
$\hat{\mathbf{w}}_{ti}$	The location with the i^{th} largest traffic volume at epoch t
x^n_t	Binary variables indicating whether the RABS n be active or not at epoch t
$y^n_{ti\to t'i'}$	Binary variables indicating whether the RABS n fly from $\hat{\mathbf{w}}_{ti}$ to $\hat{\mathbf{w}}_{t'i'}$ or not
z^n_{ti}	Binary variables indicating whether the RABS n visit $\hat{\mathbf{w}}_{ti}$ or not
δ	Length of an epoch
σ	Standard deviation of the lognormal distribution

via fast Fourier transform, the authors find that using three frequency components, $\frac{\pi}{12}$, $\frac{\pi}{6}$ and $\frac{\pi}{4}$, could effectively achieve the trade-off between accuracy and complexity in modelling the temporal variation of traffic. It should be noted that these three frequencies correspond to the period of 24 hours, 12 hours and 8 hours, respectively, which align with user social behaviour that they exhibit repetitive behaviours within daily, semi-daily, and working hour intervals. Accordingly, the mean traffic volume among all base stations can be characterised by the following sinusoid superposition model containing these three frequency components,

$$V(t) = a_0 + a_1 \sin\left(\frac{\pi}{12}t + \varphi_1\right) + a_2 \sin\left(\frac{\pi}{6}t + \varphi_2\right) + a_3 \sin\left(\frac{\pi}{4}t + \varphi_3\right), \tag{5.1}$$

where a_0 is the average value of $V(t)$ during a period of time, $[a_1, a_2, a_3]$ and $[\varphi_1, \varphi_2, \varphi_3]$ are the amplitudes and phases that take different values in different scenarios. Fig. 5.2(a) depicts the temporal trend during a 24-hour period in four

typical regions, i.e., park, campus, CBD and the whole area, as well as the amplitudes and phases measured by [133].

Afterwards, the traffic distribution is explored and modelled in the spatial domain. The authors of [133] first illustrated that, compared to commonly-used spatial Poisson point process and Gaussian distribution models, the lognormal distribution can better fit the traffic volume distribution in real cellular networks. Specifically, the authors initially select the traffic volume of all base stations for each hour in the whole area of interest, forming 24 datasets corresponding to 24 hours. Subsequently, they computed the probability density function of the traffic volume and used the lognormal distribution to fit the real data. Finally, by comparing the real traffic volume and simulated data, the authors demonstrate that the lognormal distribution can effectively model the spatial distribution of traffic, and by changing the values of standard deviation, the lognormal distribution can fit the traffic distribution for different regions. For instance, the standard deviations corresponding to parks, campuses, and CBDs are 1.3, 3.6, and 2.8, respectively [133]. Fig. 5.2(b) and Fig. 5.2(c) present the spatial distribution in parks and campuses, respectively. It can be also noticed that the traffic shows more inhomogeneity when the value of standard deviation σ is larger.

After modelling the spatial-temporal distribution of traffic based on real data, Section IV of [133] proposes a method for modelling traffic volume at small base stations, which is employed to model the traffic demands generated from all candidate locations in this section. Particularly, in the first step, the serving period is divided into T epochs with equal duration $\delta = 1$ hour, the mean traffic volume among all candidate locations, denoted by $V(t)$, can be calculated by (5.1), in which the values of amplitudes and phases can be found in the legend of Fig. 5.2(a). Secondly, the estimated volume of traffic when placing the RABS in the candidate location m at epoch t is generated by lognormal distribution samples,

$$V_m(t) = \text{lognrnd}\big(\log(V(t)) - \frac{1}{2}\sigma^2, \sigma\big), \quad \forall m, \tag{5.2}$$

Eq. (5.2) denotes that the traffic volume at the candidate location m at epoch t can be characterised by the random value following the lognormal distribution with mean $\log(V(t)) - \frac{1}{2}\sigma^2$ and standard deviation σ, where $V(t)$ is calculated via (5.1).[1]

[1]The mean m and variance v of a lognormal random variable are the functions of the lognormal distribution parameters μ and σ, i.e., $m = \exp(\mu + \sigma^2/2)$ and $v = \exp(2\mu + \sigma^2)(\exp(\sigma^2) - 1)$, where μ and σ are mean and standard deviation of logarithmic values, respectively. In Eq. (5.2), the mean of traffic volume is denoted by $V(t)$, i.e., m is set to $V(t)$, thus the mean of the lognormal distribution can be calculated as $\mu = \log(V(t)) - \frac{1}{2}\sigma^2$ [134].

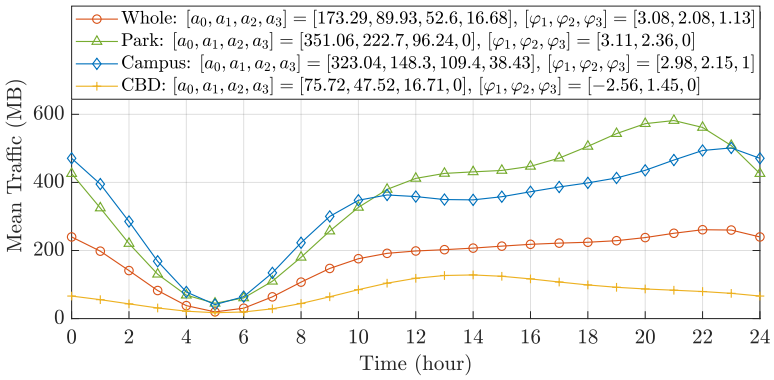

(a) Temporal distribution in 24 hour.

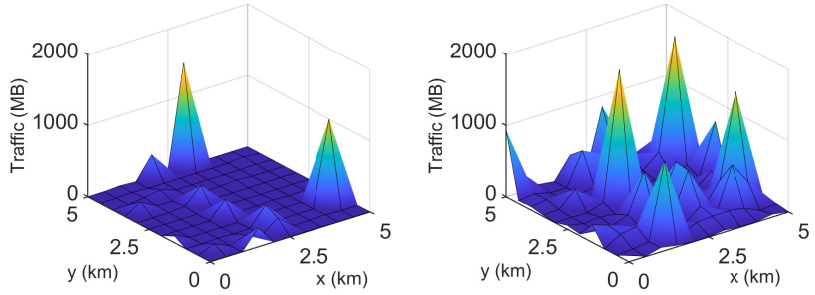

(b) Spatial distribution at 12 o'clock in campus region where $\sigma = 3.6$.

(c) Spatial distribution at 12 o'clock in park region where $\sigma = 1.3$.

Fig. 5.2 Visualisation of spatial-temporal traffic distribution.

According to the predicted traffic demand, the i^{th} largest traffic volume at epoch t is denoted by $\hat{V}_{ti}$ and the corresponding candidate location is indicated by $\hat{\mathbf{w}}_{ti}$. The locations with the largest N volume from all candidate locations are selected to deploy N RABSs at each epoch, as shown by the small dots in Fig. 5.1. According to the predicted traffic demand, the i^{th} largest traffic volume at epoch t is denoted by $\hat{V}_{ti}$ and the corresponding candidate location is indicated by $\hat{\mathbf{w}}_{ti}$. The locations with the largest N volume from all candidate locations are selected to deploy N RABSs at each epoch. For example, in Fig. 5.1, considering there are two RABSs available to be deployed, the locations with the largest and the second largest traffic volume are selected and shown by the small dots in Fig. 5.1.

5.2.2 RABS Energy Model

As shown in [107], the energy consumption of RABSs is generally composed of three main components, namely the propulsion energy, the grasping energy and the communication-related energy.

1) Propulsion Energy: Assuming the propulsion power for an RABS is denoted by P^{fly}, the flying energy of RABS when transporting from $\hat{\mathbf{w}}_{ti}$ to $\hat{\mathbf{w}}_{t'i'}$ is calculated as,

$$E^{\text{fly}}_{ti\to t'i'} = \frac{P^{\text{fly}}\|\hat{\mathbf{w}}_{t'i'} - \hat{\mathbf{w}}_{ti}\|^2}{v},\ t' > t, \tag{5.3}$$

where $\|\cdot\|$ calculates the Euclidean norm. Notably, $t' > t$ limits that the RABS can only fly from a selected location at epoch t to a location at epoch t' but cannot move in the opposite direction since the time passed.

2) Grasping Energy: The grasping power of an RABS depends on its size, weight and the hardware design of the mounted gripper [107]. Considering the ferromagnetic surfaces in tall urban landforms, such as the lampposts, electromagnetic solenoid-based grippers can be used for grasping due to their versatility [117]. Energy consumption for different kinds of grippers is further detailed in [107]. Typically, because the flying time is very short compared to the grasping and communication time (tens of seconds versus almost one hour), it is reasonable to approximate the grasping and communication time as the whole epoch duration δ so that the grasping energy consumed during an epoch can be calculated as $E^{\text{grasp}} = P^{\text{grasp}}\delta$, where P^{grasp} denotes the grasping power.

3) Communication Energy: The characteristic of communication power consumption depends on the hardware design of micro BS carried by RABS. In this work, a widely used unified BS power model proposed by [118] is employed since it is applicable to different types of communication configurations. Particularly, the communication energy for active and sleep modes can be approximated as $E^{\text{active}} = (\eta P^{\text{tra}} + P^{\text{active}})\delta$ and $E^{\text{sleep}} = P^{\text{sleep}}\delta$, respectively, where P^{tra} is the transmit power, P^{active} and P^{sleep} are the active and sleep mode power, respectively. $\eta > 0$ is a slope factor of the transmit power related to the hardware design of RABSs. In most cases, the inequality $P^{\text{sleep}} < P^{\text{active}}$ always holds so it is beneficial to turn off the RABS to save energy during the off-peak hours.

5.2.3 Problem Formulation

In this subsection, the aforementioned scenario is formulated as an optimisation problem aiming to maximise the offered traffic load with the guarantee of the onboard energy constraint by operating the RABSs mode. Unlike the terrestrial small cells operating only in the active/sleep mode, the operation decisions of RABSs incorporate the following three decisions/actions,

- **D1**: Would RABS be sleep or active at epoch t?

- **D2**: Would RABS fly from one location to another when time goes from epoch t to $t+1$?

- **D3**: At epoch t, how to deploy RABSs in N selected locations $\hat{\mathbf{w}}_{t1}, \hat{\mathbf{w}}_{t2}, ..., \hat{\mathbf{w}}_{tN}$?

Accordingly, there are three sets of binary variables employed to formulate the aforementioned decisions. The variable $x_t^n \in \{0,1\}$ denotes that the RABS n would be in active ($x_t^n = 1$) or in sleep ($x_t^n = 0$) mode at epoch t. The $y_{ti\to t'i'}^n \in \{0,1\}$ indicates whether ($y_{ti\to t'i'}^n = 1$) or not ($y_{ti\to t'i'}^n = 0$) the RABS n moves from $\hat{\mathbf{w}}_{ti}$ to $\hat{\mathbf{w}}_{t'i'}$ location. Similarly as in (5.3), the inequality $t' > t$ in $y_{ti\to t'i'}^n$ denotes the order of precedence. Finally, $z_{ti}^n \in \{0,1\}$ denotes the RABS n would visit location $\hat{\mathbf{w}}_{ti}$ ($z_{ti}^n = 1$) or not ($z_{ti}^n = 0$).

1) Constraints for coupling between decisions D1 and D3: As illustrated in Fig. 5.1, the RABS only needs to visit the locations where it is in active mode. To exploit this coupling, the following constraints should be satisfied,

$$\sum_{i=1}^{N} z_{ti}^n = x_t^n, \quad \forall n \in \{1,...,N\},\ \forall t \in \{1,...,T\}, \tag{5.4}$$

Equation (5.4) denotes that the RABS would be active at epoch t ($x_t^n = 1$) only when it visits one selected location at epoch t ($\sum_{i=1}^{N} z_{ti}^n = 1$).

2) Degree constraints for decisions D2 and D3: To satisfy the degree requirement for decisions D2 and D3, two pseudo-epochs are introduced and indexed by 0 and $T+1$. The following equations are employed to formulate the degree constriants,

$$\begin{cases} \sum\limits_{t'=t+1}^{T+1} \sum\limits_{i'=1}^{N} y_{ti\to t'i'}^n = z_{ti}^n, \forall i \in \{1,...,N\}, \forall n \in \{1,...,N\}, \forall t \in \{0,1,...,T\}, & \text{(5.5a)} \\ \sum\limits_{t'=0}^{t-1} \sum\limits_{i'=1}^{N} y_{t'i'\to ti}^n = z_{ti}^n, \forall i \in \{1,...,N\}, \forall n \in \{1,...,N\}, \forall t \in \{1,...,T+1\}, & \text{(5.5b)} \end{cases}$$

where (5.5a) depicts whether the RABS would depart from $\hat{\mathbf{w}}_{ti}$ or not, while (5.5b) indicates the landing process. For notational convenience, the energy consumption related to these two introduced pseudo-epochs is assumed to satisfy the following equation,

$$\begin{cases} E_{ti\to T+1i'}^{\text{fly}} = 0, \quad \forall i, i', t \in \{0,1,...,T\}, & \text{(5.6a)} \\ E_{0i\to ti'}^{\text{fly}} = E_{1i\to ti'}^{\text{fly}}, \quad \forall i, i', t \in \{1,2,...,T+1\}. & \text{(5.6b)} \end{cases}$$

Equation (5.6a) represents that the flying energy consumed by moving from any $\hat{\mathbf{w}}_{ti}$ to the selected locations at epoch $T+1$, i.e., $\hat{\mathbf{w}}_{T+1i'}$, is equal to 0, while (5.6b)

illustrates that the flying energy consumed by any path departing from $\hat{\mathbf{w}}_{0i}$ is equal to the value of which taking off from $\hat{\mathbf{w}}_{1i}$.

3) Energy constraints: By recalling the energy model mentioned in Section 5.2.2, the energy consumed by RABS n can be calculated by the sum of propulsion, grasping and communication energy,

$$E^n = \sum_{t=0}^{T}\sum_{i=1}^{N}\sum_{t'=t+1}^{T+1}\sum_{i'=1}^{N} E^{\text{fly}}_{ti\to t'i'} y^n_{ti\to t'i'} + \sum_{t=1}^{T}(E^{\text{active}} + E^{\text{grasp}})x^n_t + \sum_{t=1}^{T}(E^{\text{sleep}} + E^{\text{grasp}})(1-x^n_t), \tag{5.7}$$

Subsequently, the energy constraints ensuring that the onboard battery cannot run out are as follows,

$$E^n \le E^{\max}, \quad \forall n \in \{1,...,N\}, \tag{5.8}$$

where $E^{\max}$ indicates the capacity of the onboard battery.

4) Constraints for avoiding collision: For each selected location $\hat{\mathbf{w}}_{ti}$, there is at most one RABS that can visit at each epoch, that is,

$$\sum_{n}^{N} z^n_{ti} \le 1, \quad \forall t \in \{1,...,T\}, \forall i \in \{1,...,N\}, \tag{5.9}$$

Hereafter, the operation problem of RABSs aiming to maximise the total served traffic is formulated as,

$$\max_{\{x^n_t\}\{y^n_{ti\to t'i'}\}\{z^n_{ti}\}} \sum_{n=1}^{N}\sum_{t=1}^{T}\sum_{i=1}^{N} \hat{V}_{ti} z^n_{ti}, \tag{5.10a}$$

$$s.t.\ (5.4), (5.5\text{a}) - (5.5\text{b}), (5.8), (5.9), \tag{5.10b}$$

$$x^n_t \in \{0,1\},\ \forall n \in \{1,...,N\}, \forall t \in \{1,...,T\}, \tag{5.10c}$$

$$y^n_{ti\to t'i'} \in \{0,1\},\ \forall n \in \{1,...,N\}, \forall ti \to t'i'^2, \tag{5.10d}$$

$$z^n_{ti} \in \{0,1\},\ \forall n \in \{1,...,N\}, \forall t \in \{1,...,T\}, \forall i \in \{1,...,N\}. \tag{5.10e}$$

It can be seen that (5.10) is an integer linear programming (ILP) and its scale grows sharply as T and N increase because of the indexes combined in the variables. In other words, solving (5.10) by ILP solvers, such as Gurobi [67], can be very time-consuming and only applicable for small or medium problem instances. The following Section 5.3 investigates a special case with only one RABS, in which case, as will be shown, the problem (5.10) can be greatly simplified. By exploiting the formulation structure of this special problem, a Lagrangian heuristic method is developed to obtain a high-quality solution in polynomial time. Afterwards, a

polynomial-time decomposition strategy is then proposed based on the minimum-weight perfect matching problem in Section 5.4 to decompose the multi-RABS problem (5.10) into several single-RABS cases.

5.3 Special Case: Single-RABS Problem

In this section, a special case of (5.10) with only one RABS is studied, which formulation can be greatly simplified from (5.10) and includes a knapsack constraint and a set of totally unimodular constraints. Then the Lagrangian dual of the problem with this structure is proven to be equal to the optimal value of its linear relaxation. Based on this analysis, a Lagrangian heuristic algorithm is developed to achieve a near-optimal solution in polynomial time, which can provide insightful information on the potential gains of deploying a robotic small cell.

5.3.1 Problem Formulation and Analysis

To simplify the formulation (5.10) to the single-RABS case, some indexes and variables can be eliminated since the decision D3 does not need to be considered anymore. As illustrated in Section 5.2.1, the location with the best traffic volume, denoted by $\hat{V}_t$, is selected for each epoch when there is one RABS. This selected location is denoted by $\hat{\mathbf{w}}_t$. According to equation (5.3), the propulsion energy when flying from $\hat{\mathbf{w}}_t$ to $\hat{\mathbf{w}}_{t'}$ can be calculated by,

$$E^{\text{fly}}_{t\to t'} = \frac{P^{\text{fly}}\|\hat{\mathbf{w}}_{t'} - \hat{\mathbf{w}}_t\|^2}{v},\ t' > t, \tag{5.11}$$

Similarly, the binary variables can also be simplified. In that case, $x_t \in \{0,1\}$ indicates whether the RABS would be active or sleep at epoch t. Also, $y_{t\to t'} \in \{0,1\}$ denotes whether the RABS would be relocated from $\hat{\mathbf{w}}_t$ to $\hat{\mathbf{w}}_{t'}$ or not. Notably, (5.4) shows that being active at epoch t implies that the RABS visits location $\hat{\mathbf{w}}_t$. Thus, the variables $\{z^n_{ti}\}$ do not need to be considered since it is duplicates of $\{x_t\}$ in the single-RABS case.

[2] For simplicity of notation, $\forall ti \to t'i'$ is used to represent $\forall ti \to t'i' \in \{ti \to t'i' \big| t \in \{0,..,T\}, i \in \{1,...,N\}, t' \in \{1,..,T+1\}, i' \in \{1,...,N\}, t' > t\}$.

Similar to (5.7), the energy consumption of RABS can be calculated by,

$$E = \sum_{t=0}^{T} \sum_{t'=t+1}^{T+1} E^{\text{fly}}_{t\to t'} y_{t\to t'} + \sum_{t=1}^{T} (E^{\text{active}} + E^{\text{grasp}}) x_t + \sum_{t=1}^{T} (E^{\text{sleep}} + E^{\text{grasp}})(1 - x_t). \tag{5.12}$$

Hereafter, the operation problem for a single-RABS case can be formulated as,

$$\max_{\{x_t\}\{y_{t\to t'}\}} \sum_{t=1}^{T} \hat{V}_t x_t, \tag{5.13a}$$

$$s.t. \sum_{t'=t+1}^{T+1} y_{t\to t'} = x_t, \quad \forall t \in \{0,1,...,T\}, \tag{5.13b}$$

$$\sum_{t'=0}^{t-1} y_{t'\to t} = x_t, \quad \forall t \in \{1,...,T,T+1\}, \tag{5.13c}$$

$$E \le E^{\max}, \tag{5.13d}$$

$$x_t \in \{0,1\}, \quad \forall t \in \{0,1,...,T,T+1\}, \tag{5.13e}$$

$$y_{t\to t'} \in \{0,1\}, \quad \forall t \to t'^{3}. \tag{5.13f}$$

The constraints in (5.13b) and (5.13c) represent that the RABS would depart from $\hat{\mathbf{w}}_t$ ($\sum_{t'=t+1}^{T+1} y_{t\to t'} = 1$) and land at $\hat{\mathbf{w}}_t$ ($\sum_{t'=0}^{t-1} y_{t'\to t} = 1$) only when it is active at epoch t ($x_t = 1$), respectively. Finally, (5.13d) is the energy budget constraint to guarantee that the RABS would not run out of onboard battery during the defined time horizon T.

Clearly, it can be seen that (5.13) is also an ILP and its scale is much smaller than (5.10). However, constraint (5.13d) poses a challenge since it resembles a binary knapsack constraint. Thus, (5.13) is not easier than the NP-hard knapsack problem and its scale increases sharply with a growing T, verified by footnote 3. In other words, solving the globally optimal solution may take an extremely long computational time when the problem size is large. To balance the computational complexity and the optimality of the solution, an algorithm is proposed to efficiently achieve a near-optimal solution based on the structure of (5.13).

Lemma 1: *The set of constraints* (5.13b)-(5.13c) *is totally unimodular.*

Proof: Hereafter, the Lemma 2 is proven under the assumption $T = 3$, and the proof can be extended to any value of T. Setting $T = 3$, the constraints (5.13b)-

[3] For simplicity of illustration, $\forall t \to t'$ is used to represent $\forall t \to t' \in \{t \to t' \big| t \in \{0,..,T\}, t' \in \{1,..,T+1\}, t' > t\}$.

(5.13c) is as follows,

$$\begin{cases} y_{0\to1}+y_{0\to2}+y_{0\to3}+y_{0\to4}=x_0, & (5.14a)\\ y_{1\to2}+y_{1\to3}+y_{1\to4}=x_1, & (5.14b)\\ y_{2\to3}+y_{2\to4}=x_2, & (5.14c)\\ y_{3\to4}=x_3, & (5.14d)\\ y_{0\to1}=x_1, & (5.14e)\\ y_{0\to2}+y_{1\to2}=x_2, & (5.14f)\\ y_{0\to3}+y_{1\to3}+y_{2\to3}=x_3, & (5.14g)\\ y_{0\to4}+y_{1\to4}+y_{2\to4}+y_{3\to4}=x_4. & (5.14h) \end{cases}$$

Accordingly, the parameter matrix of (5.14a)-(5.14h) is given by (5.15), where each row denotes the parameters of all variables shown in the corresponding constraint, e.g. the first row denotes the parameters in (5.14a). The corollary 2.1 in Section 2.3 proves the fact *"If the* $(0,1,-1)$ *matrix A has no more than two nonzero entries in each column, and if* $\sum_j a_{ij}=0$ *if column j contains two nonzero coefficients, then B is totally unimodular."* Thus, the matrix in (5.15) is totally unimodular. □

$$\begin{array}{c} \begin{array}{ccccccccccccccc} y_{0\to1} & y_{0\to2} & y_{0\to3} & y_{0\to4} & y_{1\to2} & y_{1\to3} & y_{1\to4} & y_{2\to3} & y_{2\to4} & y_{3\to4} & x_0 & x_1 & x_2 & x_3 & x_4 \end{array} \\ \begin{pmatrix} 1 & 1 & 1 & 1 & 0 & 0 & 0 & 0 & 0 & 0 & -1 & 0 & 0 & 0 & 0 \\ 0 & 0 & 0 & 0 & 1 & 1 & 1 & 0 & 0 & 0 & 0 & -1 & 0 & 0 & 0 \\ 0 & 0 & 0 & 0 & 0 & 0 & 0 & 1 & 1 & 0 & 0 & 0 & -1 & 0 & 0 \\ 0 & 0 & 0 & 0 & 0 & 0 & 0 & 0 & 0 & 1 & 0 & 0 & 0 & -1 & 0 \\ -1 & 0 & 0 & 0 & 0 & 0 & 0 & 0 & 0 & 0 & 0 & 1 & 0 & 0 & 0 \\ 0 & -1 & 0 & 0 & -1 & 0 & 0 & 0 & 0 & 0 & 0 & 0 & 1 & 0 & 0 \\ 0 & 0 & -1 & 0 & 0 & -1 & 0 & -1 & 0 & 0 & 0 & 0 & 0 & 1 & 0 \\ 0 & 0 & 0 & -1 & 0 & 0 & -1 & 0 & -1 & -1 & 0 & 0 & 0 & 0 & 1 \end{pmatrix} \end{array} \tag{5.15}$$

Relaxing the energy constraint (5.13d) by a nonnegative Lagrange multiplier λ, the Lagrangian relaxation of (5.13) can be written as follows,

$$z_{\mathrm{LR}}(\lambda)=\max_{\{x_t\}\{y_{t\to t'}\}}\sum_{t=1}^{T}\hat{V}_t x_t-\lambda\left(E-E^{\max}\right), \tag{5.16a}$$

$$s.t.\ (5.13b),(5.13c),(5.13e),(5.13f), \tag{5.16b}$$

where $z_{\mathrm{LR}}(\lambda)$ denotes the Lagrangian relaxation and certainly is an upper-bound for (5.13). The Lagrangian dual problem calculating the least upper-bound can be

expressed as,

$$z_{\mathrm{LD}} = \min_{\lambda \geq 0} z_{\mathrm{LR}}(\lambda). \tag{5.17}$$

Another widely used relaxation technique of ILP is to relax the integer variables to continuous variables, namely linear relaxation of the ILP. To this end, the linear relaxation of (5.13) is as follows,

$$z_{\mathrm{LP}} = \max_{\{x_t\}\{y_{t\to t'}\}} \sum_{t=1}^{T} \hat{V}_t x_t, \tag{5.18a}$$

$$s.t. \quad (5.13b) - (5.13d), \tag{5.18b}$$

$$x_t \in [0,1], \quad \forall t \in \{0,1,...,T\}, \tag{5.18c}$$

$$y_{t\to t'} \in [0,1], \quad \forall t \to t'. \tag{5.18d}$$

The following proposition proves that the value of dual z_{LD} can be achieved by solving the linear relaxation (5.18). This fact could be utilised to choose a step size to guarantee the convergence of the subgradient method in the following Section 5.3.2.

Proposition 1: $z_{LD} = z_{LP}$

Proof: Define a polyhedral $\mathbf{Q}$ generated by constraints in (5.10b) and (5.10c). Since Lemma 1 shows that the parameter matrix of (5.10b)-(5.10c) is totally unimodular, the extreme points of polyhedral $\mathbf{Q}$ are integral. Corollary 6.6 in section II.3.6 of [84] proves the fact $z_{\mathrm{LD}} = z_{\mathrm{LP}}$. □

5.3.2 Lagrangian Heuristic Algorithm

Although proposition 1 illustrates that the value of Lagrangian dual z_{LD} can be achieved by solving the linear programming (5.18), the obtained results may not be integer so that it is still tricky to generate a feasible solution for (5.13). In this subsection, a Lagrangian heuristic algorithm is proposed which includes two steps, namely solving the dual problem (5.17) through the subgradient method and refining a feasible solution for (5.13). It can be shown that compared with solving (5.18) directly, the captured value of variables by the subgradient method is integer thus easing the refinement of feasible solutions for (5.13).

1) Subgradient Method for solving Lagrangian dual (5.17)*:* In the first step, the Lagrangian dual problem (5.17) is solved by the subgradient method in view of its convex and non-smooth construction. For any given λ, the subgradient direction can be obtained through the Lagrangian relaxation (5.16), which is still an ILP and thus difficult to solve. Fortunately, recalling that Lemma 1 points out the totally

unimodular structure of the constraints in (5.16), the optimal integer solution of (5.16) can be solved through its linear relaxation as follows [84] ,

$$\max_{\{x_t\}\{y_{t\to t'}\}} \sum_{t=1}^{T} \hat{V}_t x_t - \lambda\left(E - E^{\max}\right), \tag{5.19a}$$

$$s.t. \quad (5.13b), (5.13c), \tag{5.19b}$$

$$x_t \in [0,1], \quad \forall t \in \{0,1,...,T,T+1\}, \tag{5.19c}$$

$$y_{t\to t'} \in [0,1], \quad \forall t \to t'. \tag{5.19d}$$

Subsequently, a subgradient direction for a certain λ can be selected as [86],

$$g = E - E^{\max}. \tag{5.20}$$

To decrease the dual value $z_{\mathrm{LR}}(\lambda)$ along the subgradient direction, λ can be updated by,

$$\lambda_{k+1} = [\lambda_k - \alpha_k g_k]^+, \tag{5.21}$$

where notation $[\cdot]^+$ is defined as $[\cdot]^+ \triangleq \max(\cdot, 0)$, λ_k, α_k and g_k are the Lagrangian multiplier, step size and subgradient at k^{th} iteration, respectively. Furthermore, to ensure that $\{\lambda_k\}$ can converge to the optimal multiplier, the step size α_k can be chosen as [135],

$$\begin{cases} \alpha_0 = \dfrac{z_{\mathrm{LP}} - z_{\mathrm{LR}}(\lambda_0)}{\|g_0\|^2}, & (5.22a) \\ \alpha_k = \left(1 - \dfrac{1}{\beta k^{1-k^{-r}}}\right) \dfrac{\alpha_{k-1}\|g_{k-1}\|}{\|g_k\|}, & (5.22b) \end{cases}$$

where $\beta \geq 1$ and $0 < r < 1$ are predefined parameters. The procedure of the subgradient method is summarised as the step 1-6 in Algorithm 4.

2) Construct a feasible solution: Although the solution obtained by subgradient method is integer, it generally does not satisfy the energy constraint (5.13d) because of the relaxation operation in (5.16). To this end, a greedy method is then proposed to refine a feasible solution. Starting from the results obtained by subgradient method, the idea is to choose the active epoch with the least traffic load, then switch this epoch into the sleep status and delete the associated flying paths. Repeat this process until the energy constraint (5.13b) is satisfied. The greedy method is shown as the step 7-9 in Algorithm 4.

Remark 1: (Stopping criteria) In Algorithm 4, it can be verified that the proposed refinement procedure in step 7-9 can always return a feasible solution for problem (5.13) whenever the subgradient method in step 1-6 stops. Thus, to control the

Algorithm 4 Lagrangian Heuristic Algorithm

1: Solve (5.18) and denote the solution as z_{LP}.
2: Initialise λ_0. Obtain $z_{\mathrm{LR}}(\lambda_0)$ and g_0 by solving (5.19). Initialise the step size through (5.22a). Set $k = 1$.
3: **repeat**
4: Update the λ_k through (5.21). Obtain $z_{\mathrm{LR}}(\lambda_k)$ and g_k by solving linear programming (5.19). Update the step size through (5.22b).
5: $k = k + 1$.
6: **until** The number of iterations k achieves a threshold $k^{\max}$.
7: **repeat**
8: Choose the active epoch with the least traffic load. Switch the RABS into sleep mode at this epoch and delete the related route.
9: **until** Energy constraint (5.13d) is satisfied.

running time conveniently, the stopping criteria is set as the maximum number of iterations instead of the gap between $z_{\mathrm{LR}}(\lambda_k)$ and z_{LD}, which is a widely used stopping criteria to guarantee the result accuracy. Besides, the algorithm performance with different $k^{\max}$ would be evaluated in the following Section 5.5.

Remark 2: (Computation complexity) In the section 6.6.1 of [136], the worst case of solving a linear programming is approximately $\mathcal{O}\big((n^v + n^c)^{1.5} n^{v2}\big)$, where n^v and n^c are the number of variables and constraints respectively. Moreover, the refinement procedure 7-9 would check at most T epochs, thus the complexity of Algorithm 4 is approximately,

$$\mathcal{O}\big(k^{\max} \cdot (n^v + n^c)^{1.5} n^{v2} + T\big), \tag{5.23}$$

where $n^v = (T+2) + (T+2)!/2T!$ and $n^c = (3T+4) + (T+2)!/2T!$ for linear programming (5.19).

5.4 Decomposition Strategy for multi-RABS Problem

In Section 5.3, it is shown that the single-RABS problem (5.13) has a much smaller scale than multi-RABS case (5.10) and can be solved by Lagrangian heuristic algorithm efficiently. In view of this, a polynomial-time decomposition strategy is proposed based on the minimum-weight perfect matching problem to decompose the multi-RABS problem (5.10) into several single-RABS cases.

Instead of considering the energy consumption as a constraint in (5.10), the basic idea of the decomposition strategy is to minimise the total energy consumption with the guarantee of achieving the highest traffic load. In other words, the energy

when RABSs visit all the selected locations $\{\hat{\mathbf{w}}_{ti} \big| \forall t \in \{1,...,T\}, \forall i \in \{1,...,N\}\}$ is minimised. By taking the energy constraint (5.8) as the objective function, the problem formulation can be extended from (5.10) straightforwardly,

$$\min_{\{x_t^n\}\{y_{ti\to t'i'}^n\}\{z_{ti}^n\}} \sum_{n=1}^{N} E^n, \tag{5.24a}$$

$$s.t.\ (5.4), (5.5a) - (5.5b), \tag{5.24b}$$

$$\sum_{n}^{N} z_{ti}^n = 1, \quad \forall t \in \{1,...,T\}, \forall i \in \{1,...,N\}, \tag{5.24c}$$

$$(5.10c) - (5.10e). \tag{5.24d}$$

The objective function (5.24a) minimises the total energy consumption. The constraints in (5.24c) guarantee that all selected locations can be visited by RABSs, which is obtained by changing the inequality in (5.9) to strict equality. Although the problem (5.24) seems to be the dual problem of (5.10), it is actually not the dual, but obtained by swapping the objective function (5.10a) and the constraint (5.8), thereby minimising the total energy consumption with the guarantee of achieving the highest traffic load. It is worth noting that the solution of (5.24) is not feasible in practice because it does not take the capacity of the RABS onboard batteries into consideration. However, it can decompose the multi-RABS problem (5.10) into a group of single-RABS cases, as discussed in the following.

To solve (5.24), the first observation is that both (5.10) and (5.24) can be modelled on a multi-layer directed graph. A multi-layer graph is constructed as follows: Generate T layers, each of which represents an epoch. In each layer, there are N vertices and each of them corresponds to a selected location at this epoch. Two vertices $\hat{\mathbf{w}}_{ti}$ and $\hat{\mathbf{w}}_{t'i'}$ are connected by a directed edge if $t' > t$, as required by footnote 2 to satisfy the order of precedence. Each edge is assigned an energy consumption value of the RABS flying along this route. Each vertex is associated with an energy consumption level $E^{\text{active}} - E^{\text{sleep}}$ as well as the corresponding traffic load $\hat{V}_{ti}$. Fig. 5.3 shows an example graph when setting $T = 3$ and $N = 2$. Recalling that problem (5.10) aims to maximise the volume of served traffic under the limitation of the RABS onboard battery. Mapping (5.10) to the generated graph in Fig. 5.3, it can be observed that solving (5.10) is equivalent to obtaining N paths from the first layer to T^{th} layer covering a subset of vertices with the largest traffic volume and guaranteeing that the energy consumption of each path is less or equal to $E^{\max} - T(E^{\text{sleep}} + E^{\text{grasp}})$. The red and blue lines in Fig. 5.3(a) present two routes for RABSs, i.e., $\hat{\mathbf{w}}_{11} \to \hat{\mathbf{w}}_{31}$ and $\hat{\mathbf{w}}_{12} \to \hat{\mathbf{w}}_{21} \to \hat{\mathbf{w}}_{32}$, which are corresponding to the toy example illustrated in Fig. 5.1.

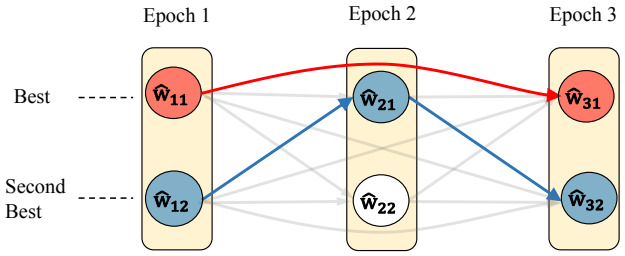

(a) A possible solution for (5.10) corresponding to Fig. 5.1.

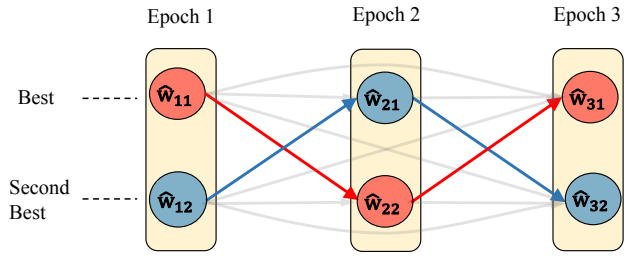

(b) A possible solution for (5.24).

Fig. 5.3 Model the problems (5.10) and (5.24) on a multi-layer directed graph.

On the other hand, considering the problem (5.24) minimises the energy consumption when all the selected candidate locations are being visited, the corresponding map in the graph is to obtain N paths with the minimal total energy consumption and all vertices are required to be covered. Fig. 5.3(b) shows an example solution for (5.24) including two routes, i.e., $\hat{\mathbf{w}}_{11} \rightarrow \hat{\mathbf{w}}_{22} \rightarrow \hat{\mathbf{w}}_{31}$ and $\hat{\mathbf{w}}_{12} \rightarrow \hat{\mathbf{w}}_{21} \rightarrow \hat{\mathbf{w}}_{32}$. Hereafter, the graph version of problem (5.24) is named as multi-source Shortest Paths problem with Edge Covering (MSPEC) for notational convenience, in which 'shortest paths' means the minimal energy consumption and 'edge covering' means that a subset of edges should be chosen to cover all vertices.

To solve the MSPEC problem, some definitions from graph theory are first revised. A *perfect matching* on a graph is a subset of edges such that each node in this graph is met by exactly one edge in the subset. Assigning each edge with a weight, the *minimum-weight perfect matching problem* is to find a perfect matching with the minimum total weight. Besides, a graph is called *bipartite* if there is a partition of vertices into two disjoint subsets, such that every edge in the graph joins the vertices in one subset to another. The following lemma and proposition prove that the MSPEC problem can be solved in a timely manner.

Lemma 2: *In the multi-layer graph, select the vertices in two adjacent layers, i.e., t and $t+1$, as well as all joint edges, and construct a subgraph denoted by $\mathcal{G}_t$, as shown in Fig. 5.4. There exists a perfect matching on $\mathcal{G}_t$.*

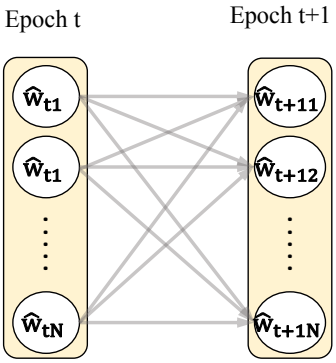

Fig. 5.4 Generate a subgraph $\mathcal{G}_t$ by selecting two adjacent layers.

Algorithm 5 Decomposition strategy by solving (5.24)

1: Generate a multi-layer graph as Fig. 5.3 shows.
2: **for** $t \in \{1,2,...,T-1\}$ **do**
3: Select two adjacent layers t and $t+1$, and construct a subgraph $\mathcal{G}_t$.
4: Solve the minimum-weight perfect matching problem on $\mathcal{G}_t$ by Hungarian Algorithm.
5: **end for**
6: Link the solutions and obtain N paths from layer 1 to layer T.

Proof: Partition the vertices into two disjoint sets, i.e., $\mathcal{V}_t = \{\hat{\mathbf{w}}_{ti} \big| \forall i \in \{1,...,N\}\}$ and $\mathcal{V}_{t+1} = \{\hat{\mathbf{w}}_{t+1i} \big| \forall i \in \{1,...,N\}\}$. It can be easily observed that $\mathcal{G}_t$ is bipartite. For each subset of $\mathcal{V}_t$, denoted by $\mathcal{V}_t^{sub} \subseteq \mathcal{V}_t$, the equation $|\Gamma(\mathcal{V}_t^{sub})| = N$ always holds, where $\Gamma(\mathcal{V}_t^{sub})$ denotes the neighborhood of $\mathcal{V}_t^{sub}$, i.e., the set of all vertices in $\mathcal{G}_t$ adjacent to the elements of $\mathcal{V}_t^{sub}$. It is clear that the inequality $|\Gamma(\mathcal{V}_t^{sub})| \geq |\mathcal{V}_t^{sub}|$ is always satisfied for every $\mathcal{V}_t^{sub}$, which is required by the Hall's Marriage Theorem [137]. Thus, there exists a matching covering all elements in $\mathcal{V}_t$. Moreover, the matching is perfect since $|\mathcal{V}_t| = |\mathcal{V}_{t+1}| = N$. This completes the proof of Lemma 2. □

Proposition 2: *The MSPEC problem can be solved by solving the minimum-weight perfect matching problems on all subgraphs $\mathcal{G}_t$, where $t \in \{1,2,...,T-1\}$.*

Proof: Lemma 2 shows that there exists a perfect matching on the subgraph. Solving the minimum-weight perfect matching problems for all subgraphs and linking the optimal solutions ensures obtaining N paths from layer 1 to layer T which cover all vertices exactly once and have the minimum weight. This completes the proof of Proposition 2. □

Hereafter, the minimum-weight perfect matching problem in the subgraph $\mathcal{G}_t$ remains to be the last challenge. Fortunately, $\mathcal{G}_t$ is a bipartite graph and $|\mathcal{V}_t| = |\mathcal{V}_{t+1}| = N$. Thus, the minimum-weight perfect matching problem can be seen as

Table 5.2 Parameter Settings

Parameter	Value	Parameter	Value
$E^{\max}$	333792 J	v	30 m/s
P^{fly}	100 W [26]	η	2.6 [118]
P^{grasp}	0.5 W	P^{tra}	0.1 W
P^{active}	1 W	P^{sleep}	0.6 W

the assignment problem and solved by the Hungarian Algorithm in polynomial time [138]. The decomposition method illustrated in Position 2 is summarised in Algorithm 5. Afterwards, the N paths returned from Algorithm 5 can be then solved by the single-RABS problem (5.13) and a near-optimal solution of multi-RABS problem (5.10) is captured.

Remark 3: (Computation complexity) The complexity of solving the minimum-weight perfect matching problem by Hungarian Algorithm is $\mathcal{O}(N^3)$. Besides, there are $T-1$ subgraphs that would be processed, as shown in step 2 of Algorithm 5. Therefore, the computational complexity of Algorithm 5 is $\mathcal{O}\big((T-1)\cdot N^3\big)$.

5.5 Numerical Investigations

In this section, simulation results are presented to evaluate the proposed deployment and operation strategies for RABS, as well as the convergence of the proposed algorithms. The parameter settings are summarised in Table 5.2. In a similar manner with Fig. 5.2(c) and Fig. 5.2(b), there are 121 candidate locations evenly distributing in a $5\times 5\,\text{km}^2$ area. To generalise the following simulation results to a wide range of possible traffic manifestations, the amplitudes $[a_0,a_1,a_2,a_3]$ and phases $[\varphi_1,\varphi_2,\varphi_3]$ in (5.1) are assumed to take random values following the Gaussian distribution, which mean takes the value of the whole area as shown in Fig. 5.2 and the deviation is set to 1. The value of σ in (5.2) is set to 1.3 unless otherwise specified [133]. It should be noted that all the following numerical results are averaged by 1000 Monte Carlo simulations except Fig 5.9. Besides, assume that the RABSs is powered by a *Zappers SG4* battery and its capacity can be calculated as $15.2\,\text{V}\times 6100\,\text{mAh}\times 3.6 = 333792\,\text{J}$ [107]. This onboard battery capacity can be deemed as of a nominal value, however, other types of batteries with different capacities can be utilised with the proposed set of optimisation algorithms without loss of generality.

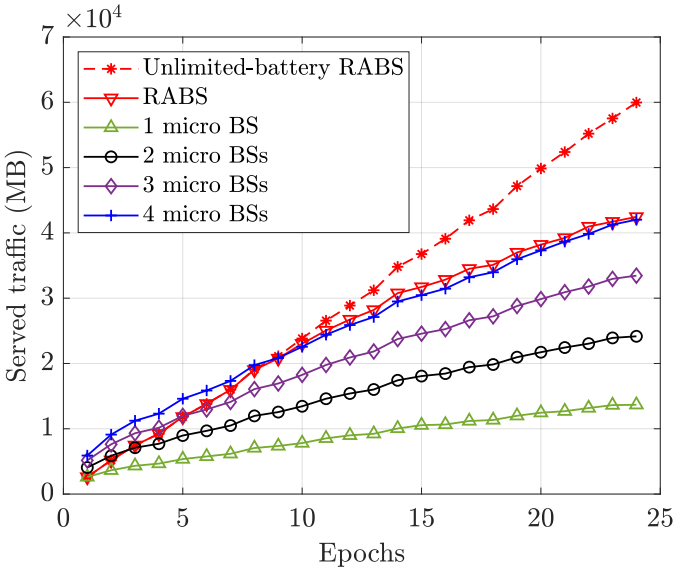

Fig. 5.5 Comparing RABS with fixed micro cells.

5.5.1 Single-RABS Case

Fig. 5.5 compares the system performance of the RABS and different numbers of fixed micro BSs when the serving period ranges from 1 hour to 24 hours. Assume that the fixed micro BSs are deployed greedily according to the predicted traffic distribution, i.e., when there is one fixed micro BS in the system, It would be deployed in the candidate location with the largest volume of traffic over the whole serving period, select the two best locations when there are two micro BSs in the system and so on. Note that fixed micro BSs are normally powered by cable, and thus can provide connectivity at all times. When relaxing the energy constraint (5.13d), the dotted line in Fig. 5.5 presents the traffic load served by an ideal RABS; this can be assumed as the upper bound on the performance. However, even when the limited capacity of the battery prevents the realisation of this optimal case, a single RABS still serves a larger volume of traffic load than four fixed small cells when $T \geq 10$. Overall, Fig. 5.5 illustrates the fact that compared with fixed micro BSs, the flexibility of RABSs offers a significant benefit even though its onboard battery can be deemed as limited. However, it should be noted that, in this chapter, to study the deployment of RABSs from a network perspective, RABSs are assumed to be able to satisfy all traffic demands generated from their deployed locations. However, in practice, the performance of RABSs would be limited by various constraints, such as transmission power, subcarrier allocation, and the capacity of backhaul links. Therefore, the simulation results in Fig. 5.5 can be regarded as an upper bound under

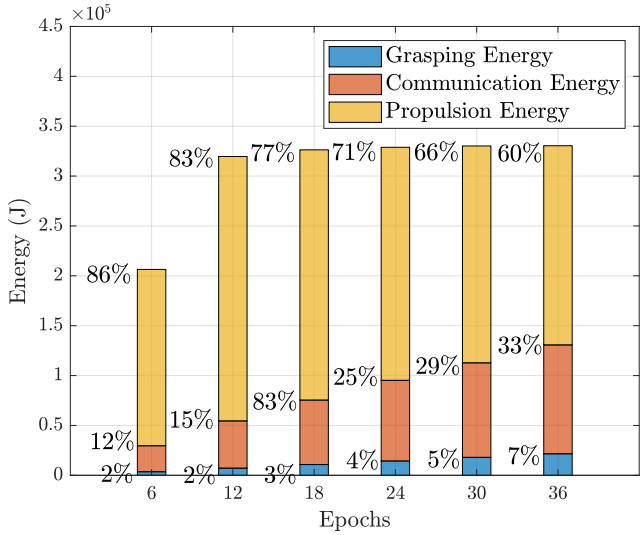

Fig. 5.6 Comparison on energy consumption for propulsion, communication and grasping.

the assumption that RABSs can satisfy all traffic demands. The following Section 6.3 further discusses the performance of RABSs under the constraint of backhaul link capacity.

Fig. 5.6 investigates the three main components of energy consumption as detailed in Section 5.2.2, i.e., the propulsion energy, the grasping energy and the communication energy. Observe that the flying (or hovering) consumes significantly more energy than grasping. This also provides a numerical explanation about why RABS operates a significantly longer endurance than nominal ABS serving in the air. Furthermore, note that for an energy-neutral grasping end effector, the perching energy consumption can be completely eliminated. Comparing the propulsion and communication power in Fig. 5.6, it can be observed that the proportion of communication energy increases when the value of T grows, whereas the percentage of the propulsion power shows a decreasing trend. Numerically, when $T = 6$, the propulsion and communication consume 13% and 86% of the total energy, respectively, while the proportions change to 33% and 60% when T grows to 36.

Fig.5.7 compares system performance served by the RABS and the micro BS under different traffic distribution deviations. Fig.5.7 shows that RABS always serves increased levels of volume of traffic load than fixed BS even though its endurance is limited by an onboard battery. Comparing the volume of served traffic under different traffic distributions, it can also be observed that the gain of RABS grows in the case when the traffic distribution shows a higher heterogeneity in the spatial domain. Taking the $T = 24$ as an example, the RABS can serve 3.0 times more

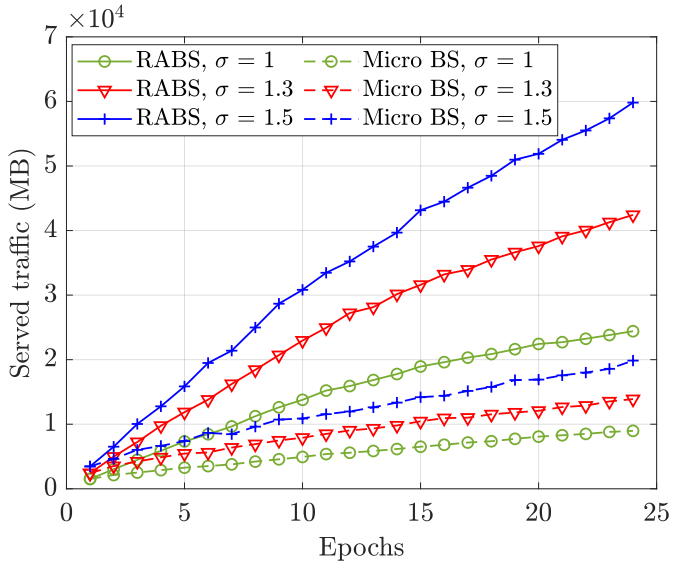

Fig. 5.7 Performances of the RABS and the micro BS under different σ.

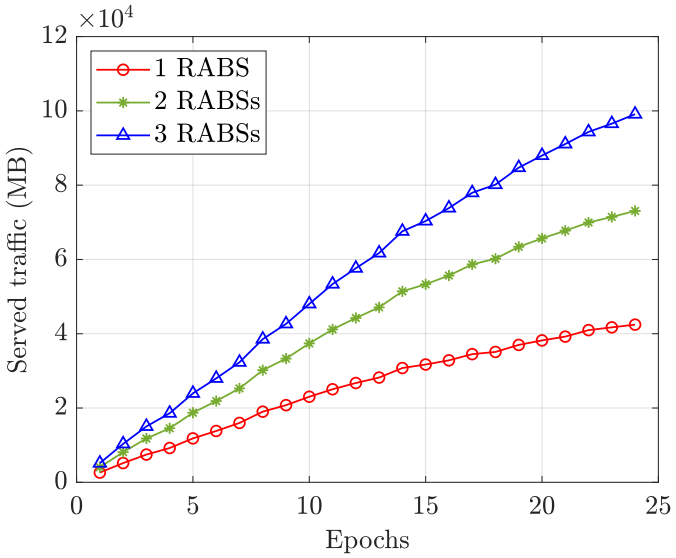

Fig. 5.8 Comparing different numbers of RABSs.

volume of traffic than fixed BS when $\sigma = 1.5$, while this gain rate decreases to 2.7 when $\sigma = 1.0$.

5.5.2 Multi-RABS Case

Fig. 5.8 illustrates the served traffic load versus different sizes of RABS swarm. It can be observed that the volume of served traffic grows as N increases since more candidate locations can be selected to deploy RABSs. However, the growth rate decreases as N increases. For instance, when there are 24 epochs, two RABSs show

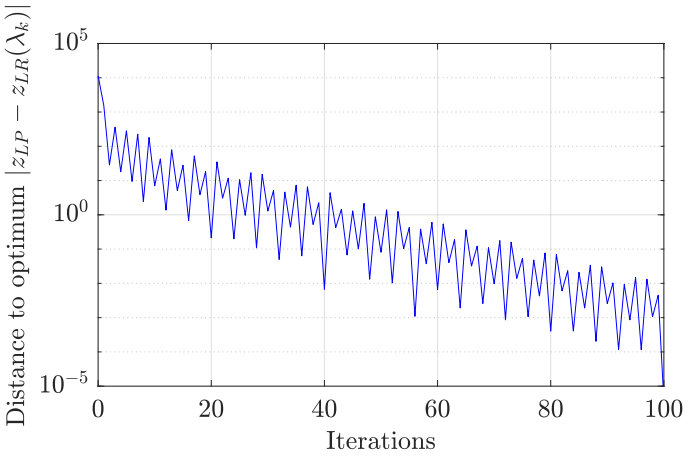

(a) Convergence of subgradient method.

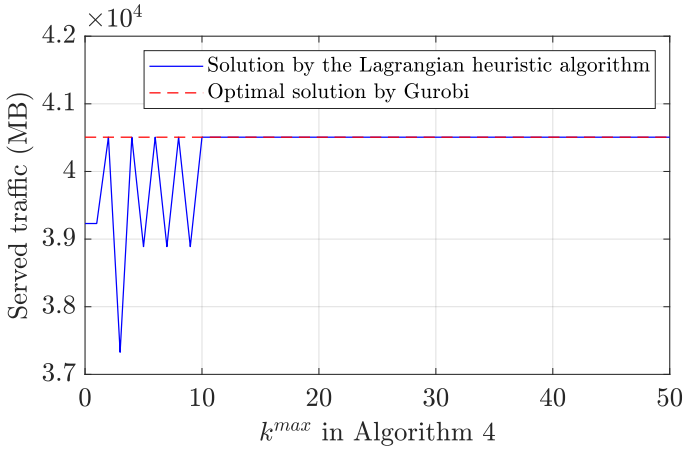

(b) Optimality of Algorithm 4.

Fig. 5.9 Convergence and optimalitiy of Algorithm 4.

a 74% larger traffic than one RABS, while the growth rate decreases to 35% when N increases from 2 to 3. In other words, and as expected, the economic benefit of employing more RABSs decreases as the RABS swarm grows.

5.5.3 Algorithm Convergence and Performance

The convergence and optimality of the proposed Algorithm 4 is investigated in Fig. 5.9. Fig. 5.9(a) shows the convergence behaviour of the subgradient method when iterating 100 times. It can be seen that the value of the Lagrangian problem $z_{\mathrm{LR}}(\lambda_k)$ in (5.16) convergences to z_{LP} as the number of iterations k increases. Reviewing that proposition 1 shows the fact $z_{\mathrm{LD}} = z_{\mathrm{LP}}$, dual problem (5.17) can be solved approximately by subgradient method in a finite number of iterations. Moreover,

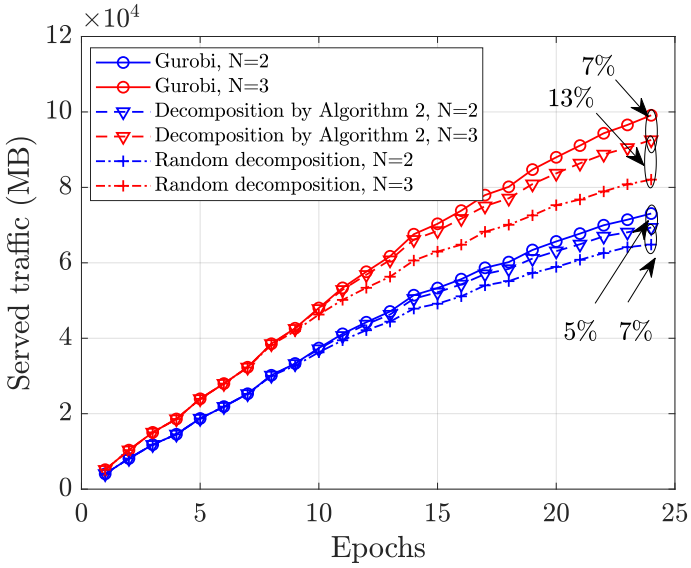

Fig. 5.10 Performance of the proposed decomposition strategy.

Fig. 5.9(b) evaluate the quality of solution captured by Algorithm 4, in which the red dotted line represents the optimal value of problem (5.13) solved by Gurobi [67] and the blue solid line indicates the solution of Algorithm 4 when setting different values of stopping criteria $k^{\max}$. It is shown that Algorithm 4 can achieve the globally optimal solution of (5.13) when $k^{\max} \geq 10$. Considering the Fig. 5.9(a) and Fig. 5.9(b) together, it is shown that a high-quality solution of (5.13) can be refined even when the dual problem (5.17) is not solved to a high degree of accuracy. For instance, when setting $k^{\max} = 10$, an optimal solution of (5.13) can be captured while the gap between $z_{\mathrm{LR}}(\lambda_k)$ and z_{LP} is still nearly 10^2.

Fig. 5.10 compares the proposed decomposition algorithm with the global optimal solution solved by Gurobi [67] solver and the random decomposition method. In the random decomposition strategy, the selected locations $\hat{\mathbf{w}}_{ti}$ are assigned to RABSs at each epoch randomly, i.e., generate a solution which is feasible for the constraints (5.24b)-(5.24d) without minimizing the energy consumption (5.24a), and then solve a group of single-RABS problems. Comparing Algorithm 2 with the random decomposition strategy, the proposed method shows a better performance especially when T is large, e.g., when setting $T = 24$, Algorithm 2 shows 13% and 7% gain than the random decomposition when $N = 3$ and $N = 2$, respectively. Afterwards, comparing Algorithm 2 with the global optimal solution, it is shown that the optimum gap increases as the number of epochs T grows. However, the running time decreases significantly when applying the proposed decomposition method, e.g., when setting $T = 24$ and $N = 3$, the average solving time of the decomposition

method is about 7s while the Gurobi running time is nearly 40s. This comes as a result of remark 2 and remark 3 which show that the computational complexity of all of the proposed algorithms is in polynomial time. In contrast, the worst-case complexity of utilizing standard ILP solvers like Gurobi [67] to solve problem (5.10) is exponential, which makes it unsuitable for medium to large network instances.

5.6 Conclusion

In Chapter 4, RABS is proposed as a novel ABS prototype to overcome the endurance limitation of conventional ABSs due to significant energy consumption for flying/hovering. To further explore the advantages of RABS in energy efficiency, an efficient optimisation model is formulated to optimally orchestrate the deployment and operation strategy for RABSs based on the underlying traffic demand in this chapter. To solve the aforementioned problem, a special case with a single RABS is first investigated and solved by a Lagrangian heuristic algorithm by exploiting the totally unimodularity structure. A polynomial-time method is then proposed to decompose the multi-RABS problem into several single-RABS cases based on the Hungarian algorithm. A wide set of numerical investigations reveals that RABSs can significantly outperform the nominal fixed small cells thanks to the inherent mobility, and their gain rate increases in the case where the traffic spatial distribution is highly heterogeneous.

Chapter 6

Incorporating Robotic Aerial Base Stations in Next-Generation Applications

6.1 Introduction

The study in Chapter 5 demonstrates that robotic aerial base stations (RABSs) can satisfy wireless demands that show high inhomogeneity in both spatial and temporal domains, primarily attributed to their inherent flexibility. Afterwards, the advent of B5G/6G technologies introduces new requirements for RABSs, urging them to play different roles in future networks. This chapter explores two novel application scenarios for RABSs in the upcoming 6G era. In Section 6.2, RABS is used as a flexible radio device performing both sensing and communication tasks. In Section 6.3, a swarm of RABSs are utilised to construct a flexible multi-hop backhauling network to satisfy the heterogeneous traffic demands.

6.2 RABS-assisted Integrated Sensing and Communications

In the upcoming 6G era, reliable wireless coverage and accurate remote sensing capabilities are crucial for emerging applications such as intelligent transport systems and smart manufacturing. This has led to the recent surge in the development of integrated sensing and communication (ISAC) techniques [139]. In this section, to further explore potential application scenarios of RABS, it is used to perform sensing

and communication tasks to bring further flexibility and agility to conventional ISAC systems.

A number of works are devoted to performing ISAC tasks to improve spectrum efficiency and reduce the expenditure cost. In [140], the sensing and communication performances, evaluated by mutual information (MI) and data rate respectively, are maximised jointly under the limitation of transmission power. The work [141] extends this approach by incorporating channel uncertainty, while in [142], the transmission power is minimised while ensuring predefined thresholds for both MI and data rate. The subcarrier assignment problem is considered in [143, 144] to optimise the transmission power and satisfaction utility, respectively. Besides the conventional terrestrial cells, unmanned aerial vehicle (UAV) is expected to improve the flexibility of next-generation cellular networks. The work [145] employs UAVs to perform ISAC tasks to improve the security and reliability of networks. The communication throughput and energy efficiency are optimised in the UAV-assisted ISAC systems in [146, 147], respectively. However, to overcome the issue that the serving endurance of UAVs is severely confined by the on-board battery capacity, this work employs the prototype of RABS carried by a UAV and mounted with a mechanical grasper so that it can attach on lampposts when providing wireless coverage and agilely relocate to another hot-spot to adapt to the traffic dynamic. The service time is significantly increased due to the lower grasping power (tens of Watts) compared to the hovering/flying power of UAV base stations (hundreds of Watts), as illustrated in Fig. 4.3 of Chapter 4.

In this section, an RABS is utilised to perform ISAC tasks in a flexible and energy-efficient manner. Moreover, instead of assuming that the users' locations are fixed and known as [140–147], this work is based on the spatial traffic distribution in which the traffic demand in a certain area can be predicted and seen as fixed during a certain period, even though the users keep moving and have dynamic demand. The performance metric of satisfaction rate (SR), introduced by [148], is employed to evaluate the degree of satisfaction for sensing and communication demand. However, rather than treating the user/terminal as a point with specific coordinates, this grid-based model considers the traffic demand generated from a defined area encompassing a range of coordinates. To address the limitations of the point-to-point communication model within this innovative context, robust optimisation tools are introduced to maximise the minimum SR and employ the cardinality constrained uncertainty set to control the robustness. The problem is then reformulated as a mixed integer linear programming (MILP) via duality theory and solved by the proposed iterative linear programming (LP) rounding algorithm

in polynomial time. Numerical results show that RABS can improve the system performance by 28.61% on average compared to fixed small cells.

6.2.1 Application Scenario and System Model

By integrating enhanced connectivity and accurate sensing, ISAC technology is regarded as a key enabler for several emerging applications in the 6G era, such as connected vehicles, smart city, and environmental monitoring. In this section, an RABS is employed as a flexible road side unit to perform both sensing and communication tasks in intelligent vehicular networks. Particularly, the RABS could transmit radio frequency signals to its surroundings and detect the range of targets by analysing the reflected signals. Based on the detected environmental information, RABS rapidly generates a real-time map including information on traffic congestion, vehicle accidents and obstacle density, and transmits this updated map to wireless users such as connected and autonomous vehicles, traffic light controllers, and accident rescue systems. As will be explained later, to improve spectrum efficiency, orthogonal frequency division multiplexing (OFDM) waveforms are used to simultaneously perform communication and sensing tasks. In other words, the ISAC waveform periodically senses the current environmental information and transmits the map information updated in the last time slot to wireless users. As indicated by Table 1 in [149], different types of application scenarios require various update latency ranging from milliseconds to seconds.

However, when determining the deployment and resource allocation strategy for RABS, prior knowledge of the sensing targets' locations is required, which cannot be obtained in advance before detecting the targets. To overcome this issue, a method is proposed in this section based on the grid-based model, which is a widely used model to characterise the spatial traffic distribution [150], and first introduced to aerial networks in [52]. To employ the grid-based model, an urban geographical area is divided into several grids, in each grid the sensing and communication demand generated within a certain time interval (e.g., half an hour or an hour) could be predicted from experience data [132]. Subsequently, the robust optimisation tool is employed to determine the RABS deployment and resource allocation, ensuring that the solution obtained is resilient and robust to accommodate variations in the real-time locations of sensing targets and wireless users. Additionally, this section focuses on a specific time period, aiming to determine RABS deployment and resource allocation for this period. The inherent flying function of RABS allows

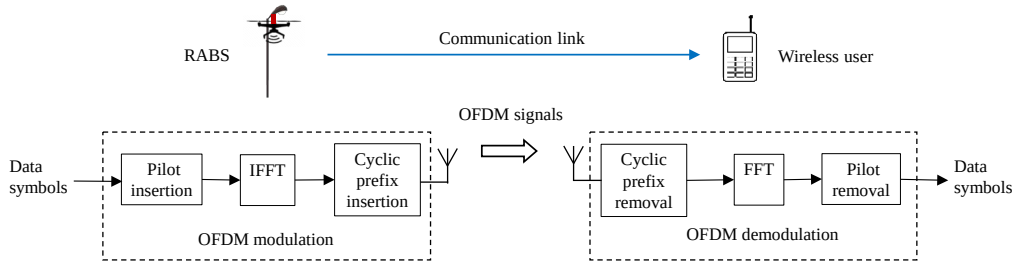

(a) Communication system based on OFDM signals.

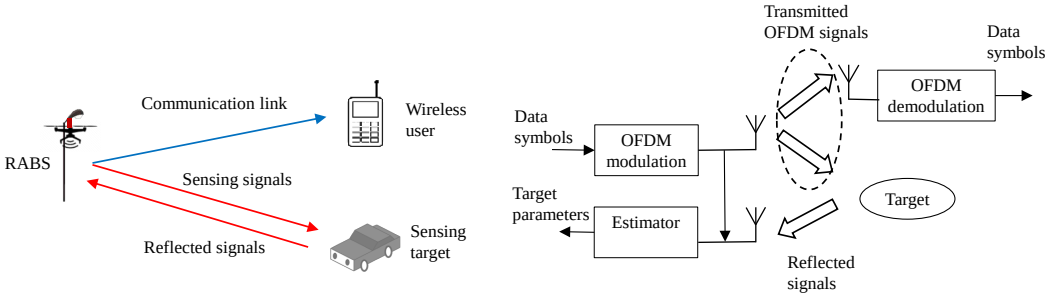

(b) ISAC system based on OFDM signals.

Fig. 6.1 Comparison of the OFDM-based ISAC and communication systems. (Inspired by the Fig. 6 in [139])

them to relocate to different lampposts as traffic patterns change in subsequent time periods.

The concept of employing OFDM waveform for ISAC tasks is originally proposed by [151], which system model is used in this chapter for RABS. As depicted in Fig. 6.1(b), data bits are firstly mapped to symbols and then modulated via a series of OFDM modulation processes, such as pilot insertion, inverse fast Fourier transform (IFFT), and cyclic prefix insertion. The generated OFDM signals are then transmitted to wireless users. It is worth pointing out that at the same time, the transmitter also replicates OFDM signals to the sensing module for processing the reflected signals later. When the broadcast signals are received by communication users, OFDM demodulation is used to demodulate signals to data symbols. Meanwhile, the transmitted OFDM signals are also reflected by sensing targets, following which the reflected signals are received by the onboard radar receiver. The sensing module mounted on RABS can calculate the range of the target by simply correlating the transmitted signals (shared with the sensing module before transmission) with the reflected signals. The system proposed in reference [151] achieves an accuracy of 1.9 m, and the subsequent work [152] improves the sensing accuracy to 0.3 m and the communication rate to 8.96 Mbps. Moreover, Fig. 6.1(a) also illustrates

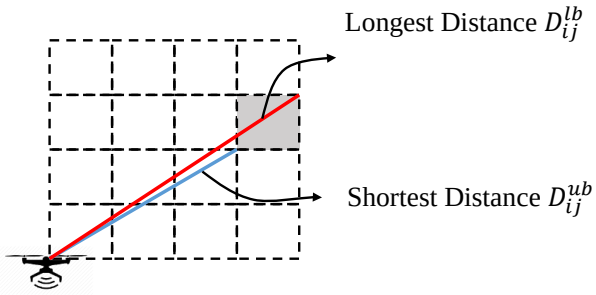

Fig. 6.2 The longest and shortest distance between a grid and RABS.

the system design of OFDM communication that cannot detect information from reflected signals.

Suppose there are K available OFDM subcarriers, denoted by $\mathcal{K} = \{1, 2, ..., K\}$, are utilised to perform ISAC. Therefore, the sensing signal performed on the subcarrier k with M consecutive integrated OFDM symbols can be described as [140, 141],

$$s_k(t) = e^{j2\pi f_k^c t} \sum_{n=0}^{N_s-1} a_k c_{kn} e^{j2\pi k\Delta f(t-nT_s)} \cdot \text{rect}[\frac{t-nT_s}{T_s}], \tag{6.1}$$

where t is the continuous-time independent variable, f_k^c and Δf are the frequency and bandwidth of subcarrier k, a_k and c_{kn} denotes the amplitude and phase code, respectively, T_s is the duration of each completed OFDM symbol including both the guard intervals and elementary symbol, and rect$[x]$ is the rectangle function that is equal to one when $x \in [0, 1]$, and zero, otherwise. Accordingly, supposing the impulse response of a sensing target on subcarrier k is characterised by $g_k(t)$, and the impulse response of the propagation channel between the transmitter and target is $h_k(t)$, the received signals can be written as $u_k(t) = s_k(t) * h_k(t) * g_k(t) + n(t)$, where $*$ is the convolution operator. An RABS is considered to be deployed in a certain area, which is divided into I grids denoted by the set $\mathcal{I} = \{1, 2, ..., I\}$. There are a group of candidate locations distributed in that geographical area which can be chosen by RABSs for grasping; this set is denoted by $\mathcal{J} = \{1, 2, ..., J\}$. Besides, it should be noted that one grid can be provisioned by one or multiple subcarriers while one subcarrier can only be assigned to at most one grid to avoid intra-cell interference.

Different performance metrics are employed to evaluate the sensing performance in aerial networks, such as Cramér–Rao lower bound and range resolution. In order to investigate the impact of RABS deployment and bandwidth allocation on the performance of ISAC systems, the conditional MI metric is utilised to assess the

radar performance, similar to [140–144]. Particularly, as mentioned above, the sensing task involves the transmitter broadcasting OFDM signals to the area of interest and recovering environmental information from the reflected signals. To quantify the amount of environmental information that can be extracted, the sensing MI is defined as the conditional MI between the target response and the reflected signal conditioned on the pre-designed sensing signal and propagation channel. Further discussions and derivation of MI can be found in Appendix B. As proposed in [140], when the sensing demand generated from grid i is served by an RABS deployed at candidate location j and operating on the subcarrier k, the lower bound value of MI will be achieved if there is a user, distributed in grid i, having the worst channel gain,

$$M_{ijk}^{\mathrm{lb}} = \frac{1}{2}\Delta f T_s N_s \log_2\left(1 + \frac{|a_k|^2 T_s^2 N_s H_{ijk}^{\mathrm{sen,lb}}}{\sigma^2}\right), \tag{6.2}$$

where $|a_k|^2$ calculates the transmission power of the subcarrier k, and $H_{ijk}^{\mathrm{sen,lb}}$ represents the lower bound of the path loss value of the surveillance channel calculated by [142],

$$H_{ijk}^{\mathrm{sen,lb}} = \frac{G_t^s G_r^s \eta \lambda_k^2}{(4\pi)^3 {D_{ij}^{\mathrm{lb}}}^4}, \tag{6.3}$$

where G_t^s and G_r^s are the transmitting and receiving antenna gain, respectively, η denotes the mean of radar cross-section of the targets distributed in the grid, λ_k is the wavelength in the subcarrier k that could be calculated by $\lambda_k = c/f_k^c$ where c is the speed of light, D_{ij}^{lb} denotes the longest distance between the grid i and candidate location j. Similarly, introducing the shortest distance D_{ij}^{ub} into (6.2) and (6.3), the upper bound value of channel gain and MI can be calculated in the best case, denoted by $H_{ijk}^{\mathrm{sen,ub}}$ and M_{ijk}^{ub}. An illustration of the lower and upper bounds of the distance is shown in Fig. 6.2. For notational convenience, the average MI can be calculated as $\overline{M}_{ijk} = (M_{ijk}^{\mathrm{ub}} + M_{ijk}^{\mathrm{lb}})/2$ and bias as $\hat{M}_{ijk} = (M_{ijk}^{\mathrm{ub}} - M_{ijk}^{\mathrm{lb}})/2$. Consequently, for any user distributed in the grid i, the MI should take value from the range $[\overline{M}_{ijk} - \hat{M}_{ijk}, \overline{M}_{ijk} + \hat{M}_{ijk}]$.

Moreover, the data rate is applied as the metric to evaluate the communication performance. The lower bound of the achievable rate can be calculated by,

$$R_{ijk}^{\mathrm{lb}} = \Delta f \log_2\left(1 + \frac{|a_k|^2 H_{ijk}^{\mathrm{com,lb}}}{\sigma^2}\right), \tag{6.4}$$

$$\begin{cases} \widetilde{M}_i \triangleq \dfrac{1}{M_i}\Big(\underbrace{\sum\limits_{j\in\mathcal{J}}\sum\limits_{k\in\mathcal{K}} \overline{M}_{ijk}x_{ijk} -}_{\substack{\text{The total satisfied MI when}\\ \text{all grids have the average MI.}}} \\ \underbrace{\max\limits_{\substack{\{\mathcal{J}_i\times\mathcal{K}_i\cup(j_i,k_i)\,|\,\mathcal{J}_i\subseteq\mathcal{J},\mathcal{K}_i\subseteq\mathcal{K},\\ |\mathcal{J}_i\times\mathcal{K}_i|\le\lfloor\Gamma_i\rfloor,(j_i,k_i)\in\mathcal{J}\times\mathcal{K}-\mathcal{J}_i\times\mathcal{K}_i\}}} \Big\{ \sum\limits_{j\in\mathcal{J}_i}\sum\limits_{k\in\mathcal{K}_i} \hat{M}_{ijk}x_{ijk} + (\Gamma_i - \lfloor\Gamma_i\rfloor)\hat{M}_{ij_ik_i}x_{ij_ik_i} \Big\}}_{\substack{\text{Robust bias of the total satisfied MI which means up to } \lfloor\Gamma_i\rfloor \text{ of these coefficients}\\ \text{are allowed to change to the worst MI, and one coefficient changes by}\\ \text{at most } (\Gamma_i-\lfloor\Gamma_i\rfloor)\hat{M}_{ij_ik_i}. \text{ Defined as the protection function in (6.8).}}} \Big), \quad (6.6a) \\ \widetilde{R}_i \triangleq \dfrac{1}{R_i}\Big(\sum\limits_{j\in\mathcal{J}}\sum\limits_{k\in\mathcal{K}} \overline{R}_{ijk}y_{ijk} - \\ \max\limits_{\substack{\{\mathcal{J}_i\times\mathcal{K}_i\cup(j_i,k_i)\,|\,\mathcal{J}_i\subseteq\mathcal{J},\mathcal{K}_i\subseteq\mathcal{K},\\ |\mathcal{J}_i\times\mathcal{K}_i|\le\lfloor\Lambda_i\rfloor,(j_i,k_i)\in\mathcal{J}\times\mathcal{K}-\mathcal{J}_i\times\mathcal{K}_i\}}} \Big\{ \sum\limits_{j\in\mathcal{J}_i}\sum\limits_{k\in\mathcal{K}_i} \hat{R}_{ijk}y_{ijk} + (\Lambda_i - \lfloor\Lambda_i\rfloor)\hat{R}_{ij_ik_i}y_{ij_ik_i} \Big\}\Big), \quad (6.6b) \end{cases}$$

where $H_{ijk}^{\text{com,lb}}$ indicates the lower bound of the communication channel gain calculated as follows[142, 143],

$$H_{ijk}^{\text{com,lb}} = \frac{G_t^c G_r^c \lambda_k^2}{(4\pi)^2 D_{ij}^{\text{lb}2}}, \quad (6.5)$$

where G_t^c and G_r^c is the transmitting and receiving antenna gain.[1] It is worth pointing out that the concept of the worst channel gain is investigated in [153] for reliable communications. The upper bound of communication channel gain and data rate, denoted by $H_{ijk}^{\text{com,ub}}$ and R_{ijk}^{ub}, can be then obtained by introducing the shortest distance D_{ij}^{ub} into (6.4) and (6.5). The average rate and bias can be calculated as $\overline{R}_{ijk} = (R_{ijk}^{\text{ub}} + R_{ijk}^{\text{lb}})/2$ and $\hat{R}_{ijk} = (R_{ijk}^{\text{ub}} - R_{ijk}^{\text{lb}})/2$, respectively. Accordingly, the data rate for any user distributed in the grid i would be within the range $[\overline{R}_{ijk} - \hat{R}_{ijk}, \overline{R}_{ijk} + \hat{R}_{ijk}]$.

Three sets of binary variables are utilised to formulate the subcarrier allocation, grid association and RABS deployment. Specifically, $x_{ijk} \in \{0,1\}$ indicates whether an RABS located at location j performs sensing operations to the user i by the subcarrier k or not; $y_{ijk} \in \{0,1\}$ denotes whether an RABS located at location j communicate with the user i on the subcarrier k or not; $z_j \in \{0,1\}$ indicates whether the RABS would be deployed at location j. Because the objective is to satisfy these demands as much as possible under resource constraints, the satisfaction rate (SR) is used to evaluate the degree of satisfaction for sensing and communication demand

[1] Similar as [142, 143], the free-space channel model is used for simplicity. Other models can be employed in the proposed formulation straightforwardly.

[148]. Accordingly, the SR for sensing demand in grid i is defined by (6.6a) shown on the top of this page. A parameter Γ_i, normally called the protection level for the i^{th} constraint, is introduced to control the conservatism of the robust optimisation model. Specifically, in the numerator of (6.6a), the first part calculates the total served sense MI when all grids perform the average channel gain, i.e., have the average MI. The second part is the robust bias, which indicates that there are up to $\lfloor \Gamma_i \rfloor$ coefficients allowed to change within the range $[\overline{M}_{ijk} - \hat{M}_{ijk}, \overline{M}_{ijk} + \hat{M}_{ijk}]$, and one coefficient can at most change by $(\Gamma_i - \lfloor \Gamma_i \rfloor)\hat{M}_{ijk}$. This kind of uncertainty set is referred to as the cardinality constrained uncertainty set in [154], which reflects the inherent nature that only a subset of grids perform the worst channel gain in order to adversely affect the MI performance. Considering two extreme cases, setting $\Gamma_i = 0$ is the most ideal scenario when all grids have the average sensing performance. In contrast, setting $\Gamma_i = |\mathcal{J}_i \times \mathcal{K}_i|$ is the most conservative case in which all grids perform the worst channel gain and therefore have the lowest MI. Overall, the numerator in (6.6a) calculates the satisfied sensing demand under the cardinality constrained uncertainty set and the denominator M_i denotes the sensing demand of the grid i. Therefore, (6.6a) defines the sensing SR $\widetilde{M}_i$. Similarly, the communication SR $\widetilde{R}_i$ is defined by (6.6b) where Λ_i and R_i are the protection level and communication demand, respectively.

Hereafter, the proposed bi-objective optimisation problem is formulated to maximise the weighted sum of minimum sensing and communication SR,

$$\max_{\mathbf{X},\mathbf{Y},\mathbf{Z},\widetilde{M},\widetilde{R}} \ \mu\widetilde{M} + (1-\mu)\widetilde{R} \tag{6.7a}$$

$$s.t.\ \widetilde{M}_i \geq \widetilde{M},\ \widetilde{R}_i \geq \widetilde{R}, \quad \forall i, \tag{6.7b}$$

$$\sum_{i\in\mathcal{I}}\sum_{j\in\mathcal{J}} x_{ijk} \leq 1,\ \sum_{i\in\mathcal{I}}\sum_{j\in\mathcal{J}} y_{ijk} \leq 1, \quad \forall k, \tag{6.7c}$$

$$\sum_{i\in\mathcal{I}}\sum_{k\in\mathcal{K}} x_{ijk} \leq IKz_j,\ \sum_{i\in\mathcal{I}}\sum_{k\in\mathcal{K}} y_{ijk} \leq IKz_j,\ \forall j, \tag{6.7d}$$

$$\sum_{j\in\mathcal{J}} z_j \leq 1, \tag{6.7e}$$

$$x_{ijk}, y_{ijk}, z_j \in \{0,1\}, \quad \forall i,j,k, \tag{6.7f}$$

$$\widetilde{M}, \widetilde{R} \in [0,1], \tag{6.7g}$$

where $\mathbf{X} \triangleq \{x_{ijk}\}$, $\mathbf{Y} \triangleq \{y_{ijk}\}$ and $\mathbf{Z} \triangleq \{z_j\}$ are the set of variables, $\mu \in [0,1]$ is a predefined weight parameter. Eq. (6.7b) denotes the minimum sensing and communication SR by $\widetilde{M}$ and $\widetilde{R}$. The constraints in (6.7c) denote that each orthogonal subcarrier can at most allocated to one grid for sensing or communication to avoid

intra-cell interference, respectively. Eq. (6.7d) ensures that only when an RABS has been deployed at the location j then the grids can be associated with it for joint sensing and communication. Eq. (6.7e) indicates that there is only one RABS that can be deployed.

6.2.2 MILP Reformulation and Algorithm Design

In this section, the robust optimisation problem (6.7) is reformulated to a MILP problem via dual theory, following which an iterative LP rounding algorithm is developed to obtain a near-optimal solution in polynomial time.

To convert the constraints in (6.6a) into linear constraints, firstly define the protection function with a given $\mathbf{X}^*$ as,

$$\gamma_i(\mathbf{X}^*) = \max_{\substack{\{\mathcal{J}_i\times\mathcal{K}_i\cup(j_i,k_i)\,|\,\mathcal{J}_i\subseteq\mathcal{J},\mathcal{K}_i\subseteq\mathcal{K},\\ |\mathcal{J}_i\times\mathcal{K}_i|\leq\lfloor\Gamma_i\rfloor,(j_i,k_i)\in\mathcal{J}\times\mathcal{K}-\mathcal{J}_i\times\mathcal{K}_i\}}} \Big\{ \sum_{j\in\mathcal{J}_i}\sum_{k\in\mathcal{K}_i} \hat{M}_{ijk}x^*_{ijk} + (\Gamma_i - \lfloor\Gamma_i\rfloor)\hat{M}_{ij_ik_i}x^*_{ij_ik_i} \Big\}, \tag{6.8}$$

which can be written as the following problem:

$$\gamma_i(\mathbf{X}^*) = \max_{\mathbf{w}_i} \sum_{j\in\mathcal{J}}\sum_{k\in\mathcal{K}} \hat{M}_{ijk}x^*_{ijk}w_{ijk} \tag{6.9a}$$

$$s.t. \sum_{j\in\mathcal{J}}\sum_{k\in\mathcal{K}} w_{ijk} \leq \Gamma_i, \tag{6.9b}$$

$$0 \leq w_{ijk} \leq 1,\ \forall j,k, \tag{6.9c}$$

where $\mathbf{w}_i \triangleq \{w_{ijk}|\forall j\in\mathcal{J},\forall k\in\mathcal{K}\}$ is the introduced variable. The equality between (6.8) and (6.9) can be proved by the observation that the optimal solution of (6.9) must include $\lfloor\Gamma_i\rfloor$ variables taking the value of one and one variable at $\Gamma_i - \lfloor\Gamma_i\rfloor$. The detailed proof can be found in the Proposition 1 of [154]. Write the dual of (6.9) as follows,

$$\gamma_i(\mathbf{X}^*) = \min_{\alpha_i,\{\beta_{ijk}\,|\,\forall j,k\}} \sum_{j\in\mathcal{J}}\sum_{k\in\mathcal{K}} \beta_{ijk} + \Gamma_i\alpha_i \tag{6.10a}$$

$$s.t.\ \alpha_i + \beta_{ijk} \geq \hat{M}_{ijk}x^*_{ijk},\ \forall j,k, \tag{6.10b}$$

$$\alpha_i \geq 0, \tag{6.10c}$$

$$\beta_{ijk} \geq 0,\ \forall j,k, \tag{6.10d}$$

where $\{\alpha_i\}$ and $\{\beta_{ijk}\}$ are dual variables. It can be observed that problem (6.9) is linear programming thus the strong duality is held between (6.9) and (6.10), i.e., they have equal optimal solutions if feasible. Introducing (6.10) into (6.6a), the

constraints $\widetilde{M}_i \geq \widetilde{M}$ in (6.7b) can be rewritten as the following constraint set,

$$\begin{cases} \frac{1}{M_i}\Big(\sum\limits_{j\in\mathcal{J}}\sum\limits_{k\in\mathcal{K}}(\overline{M}_{ijk}x_{ijk}-\beta_{ijk})-\Gamma_i\alpha_i\Big) \geq \widetilde{M},\ \forall i, & (6.11a)\\ \alpha_i+\beta_{ijk} \geq \hat{M}_{ijk}x_{ijk},\ \forall i,j,k, & (6.11b)\\ \alpha_i \geq 0,\ \forall i, & (6.11c)\\ \beta_{ijk} \geq 0,\ \forall i,j,k. & (6.11d) \end{cases}$$

Applying the same procedure to the constraints $\widetilde{R}_i \geq \widetilde{R}$ in (6.7b), the problem (6.7) can be then reformulated as a MILP without loss of optimality.

To overcome the curse of dimensionality, an iterative LP rounding algorithm proposed in [155] is employed to solve the reformulated MILP problem approximately. Firstly, focus on a selected location and use the same method to traverse all candidate locations at subsequent stages to obtain the best one. It can be observed that the sensing and communication decisions in (6.7) can be decoupled once the variable $\mathbf{Z}$ is determined. Setting $z_{j'}=1$ and all other elements in $\mathbf{Z}$ are zero, a MILP problem including only the variables related to the sensing task can be written from (6.7) and (6.11) as,

$$\begin{aligned} &\max_{\mathbf{X_{j'}},\widetilde{M},\mathbf{A},\mathbf{B_{j'}}} \quad \mu\widetilde{M} && (6.12a)\\ s.t.\ &\frac{1}{M_i}\Big(\sum_{k\in\mathcal{K}}(\overline{M}_{ij'k}x_{ij'k}-\beta_{ij'k})-\Gamma_i\alpha_i\Big) \geq \widetilde{M},\ \forall i, && (6.12b)\\ &\alpha_i+\beta_{ij'k} \geq \hat{M}_{ij'k}x_{ij'k},\ \forall i,k, && (6.12c)\\ &\sum_{i\in\mathcal{I}} x_{ij'k} \leq 1,\ \forall k, && (6.12d)\\ &\widetilde{M}\in[0,1],\ \alpha_i\geq 0,\ \beta_{ij'k}\geq 0,\ \forall i,k, && (6.12e)\\ &x_{ij'k}\in\{0,1\},\ \forall i,k, && (6.12f) \end{aligned}$$

where $\mathbf{X_{j'}} \triangleq \{x_{ij'k}\big|\forall i\in\mathcal{I},\forall k\in\mathcal{K}\}$, $\mathbf{A}\triangleq\{\alpha_i\}$ and $\mathbf{B}\triangleq\{\beta_{ij'k}\big|\forall i\in\mathcal{I},\forall k\in\mathcal{K}\}$ are the sets of variables.

To apply the iterative LP rounding algorithm [155], the linear relaxation of the problem (6.12) is first proposed, that is, replacing the constraints in (6.12f) by $x_{ij'k}\in[0,1]$, and denote the solution as $(\mathbf{X}^*_{\mathbf{j'}},\widetilde{M}^*,\mathbf{A}^*,\mathbf{B}^*)$. If $\mathbf{X}^*_{\mathbf{j'}}$ is binary, the optimal solution for (6.12) is obtained. Otherwise, introduce $x_{ij'k}=1$ to (6.12) if $x^*_{ij'k}=1$ as

[2]Because the objective is to maximise the minimum SR, it is suggested that in step 5, prioritise selecting the elements in $\mathbf{X}^*_{\mathbf{j'}}$ corresponding to the grids that have not allocated any subcarriers to guarantee the fairness.

Algorithm 6 Iterative LP Rounding Algorithm for (6.12)

1: Initialise the set $\mathcal{C} = \varnothing$.
2: Solve the linear relaxation of (6.12). Denote the solution as $(\mathbf{X}^*_{\mathbf{j}'}, \widetilde{M}^*, \mathbf{A}^*, \mathbf{B}^*)$.
3: **while** There is fractional value in $\mathbf{X}^*_{\mathbf{j}'}$. **do**
4: For all $x^*_{ij'k} = 1$, add the constraint $x_{ij'k} = 1$ into $\mathcal{C}$.
5: Choose the element with the largest fractional value in $\mathbf{X}^*_{\mathbf{j}'}$ and denote it as $x_{i_0j'k_0}$.[2]Add the constraint $x_{i_0j'k_0} = 1$ into $\mathcal{C}$.
6: Add all the constraints in $\mathcal{C}$ to the linear relaxation of (6.12). Solve this modified LP.
7: If the modified LP is feasible, denote the solution as $(\mathbf{X}^*_{\mathbf{j}'}, \widetilde{M}^*, \mathbf{A}^*, \mathbf{B}^*)$ and go to step 3. If it is infeasible, replace the constraint $x_{i_0j'k_0} = 1$ by $x_{i_0j'k_0} = 0$ in $\mathcal{C}$ and go to step 6.
8: **end while**

Table 6.1 Parameter Settings

Parameter	Value	Parameter	Value
K	64	T_s	5 μs
G^s_t, G^s_r	30 dB [142]	N_s	16 [141]
G^c_r	30 dB [142]	σ^2	-174 dBm/Hz
G^c_s	0 dB	$\lvert a_k\rvert^2$	1 W
η	1 m^2 [147]	μ	0.5

new constraints. Afterwards, it should decide to round the variables with fractional values in $\mathbf{X}^*_{\mathbf{j}'}$ to binary values via a procedure of verifying feasibility. Firstly, select one variable with the largest fractional value in $\mathbf{X}^*_{\mathbf{j}'}$ and denote it as $x_{i_0j'k_0}$. Add the constraint $x_{i_0j'k_0} = 1$ to (6.12) and try to solve this modified LP. If it is infeasible, set $x_{i_0j'k_0} = 0$ and round other variables according to $\mathbf{X}^*_{\mathbf{j}'}$. If the modified LP is feasible, add the constraint $x_{i_0j'k_0} = 1$ to (6.12) and repeat the above procedure until a binary $\mathbf{X}_{\mathbf{j}'}$ is achieved or there is no more subcarrier can be allocated. The iterative LP rounding algorithm is summarised in Algorithm 6 and more details can be found in [155].

In the section 6.6.1 of [136], the worst case of solving a linear programming is $\mathcal{O}\big((n^v + n^c)^{1.5} n^{v2}\big)$, where n^v and n^c are the number of variables and constraints, respectively. In the iterative LP rounding algorithm, the number of iterations is upper bounded by $I \times K$, thus the complexity of the proposed algorithm is approximate $\mathcal{O}\big(IK \cdot (n^v + n^c)^{1.5} n^{v2}\big)$, where $n^c = 2IK + I + K + 1$ and n^v is upper bounded by $2IK + I + 1$ for the linear relaxation of (6.12).

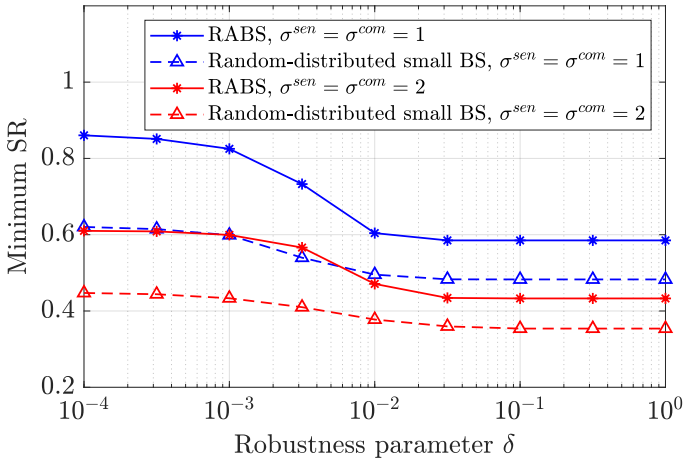

Fig. 6.3 Achievable minimum SR (objective function) versus robustness.

6.2.3 Numerical Investigations

A geographical area of 100×100 m^2 is divided into 25 small square grids with the size of 20×20 m^2, where 10 candidate locations are distributed randomly for RABS grasping. The sensing and communication demand of grids follows the log-normal distribution [133], where the mean value and standard deviation are denoted by $[m^{\text{sen}}, m^{\text{com}}]$ and $[\sigma^{\text{sen}}, \sigma^{\text{com}}]$ [133]. Hereafter, set $m^{\text{sen}} = 15$ bit, $m^{\text{com}} = 20$ Mbps and $\sigma^{\text{sen}} = \sigma^{\text{com}} = 1$ for simulation unless otherwise stated. Moreover, the carrier frequency of the ISAC signals is $f_0^c = 3$ GHz and each subcarrier has the spacing $\Delta f = 0.25$ MHz. Accordingly, the frequency of the k^{th} subcarrier is calculated by $f_k^c = f_0^c + k\Delta f$ [140]. For notational convenience, a robustness parameter δ is introduced to control the protection level $\{\Gamma_i\}$ and $\{\Lambda_i\}$, that is, $\Gamma_i = \Lambda_i = \delta \times J \times K$. Taking $\delta = 10^{-1}$ as an example, it means that 10% of the coefficients in (6.6a)-(6.6b) are allowed to take values from $[\overline{M}_{ijk} - \hat{M}_{ijk}, \overline{M}_{ijk} + \hat{M}_{ijk}]$ and $[\overline{R}_{ijk} - \hat{R}_{ijk}, \overline{R}_{ijk} + \hat{R}_{ijk}]$. Other simulation parameters are reported in Table 6.1.

By adjusting the robustness parameter δ, the protection level $\{\Gamma_i\}$ and $\{\Lambda_i\}$, as well as the robustness of the problem (6.7), can be controlled. It can be observed from Fig. 6.3 that the minimum SR decreases as the robustness increases. This is in accordance with the intuition that the growth of system robustness comes at the expense of system performance. Taking a fixed small cell distributed randomly as a benchmark, it is shown from Fig. 6.3 that the RABS can improve the system performance by 28.61% and 21.46% on average when setting the standard deviation to 1 and 2, respectively. Moreover, comparing the results for different standard deviation values of traffic distribution, it can be seen that the robustness has less

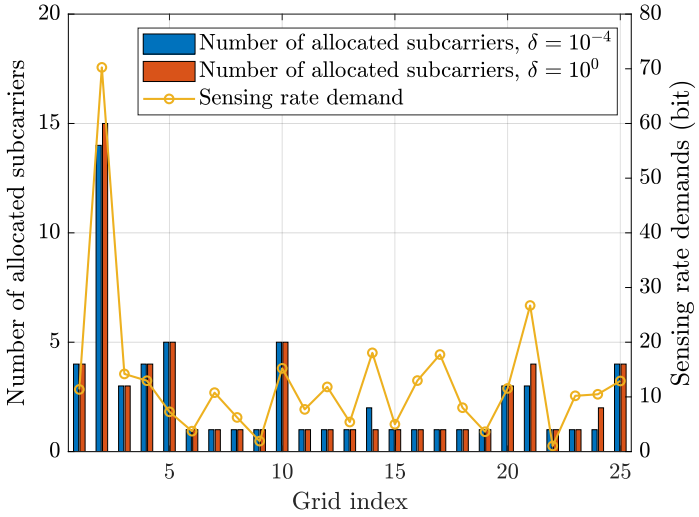

Fig. 6.4 Subcarrier allocation versus sensing rate demand.

impact on the system performance when the traffic spatial distribution is highly heterogeneous, represented as smoother curves in Fig. 6.3.

Fig. 6.4 investigates the number of subcarriers allocation versus the sensing traffic distribution. Note that more subcarriers are biased to grids with higher traffic demand. The reason is that the objective is to maximise the minimum SR to guarantee fairness. Moreover, Fig. 6.4 shows that the robustness parameter δ also affects the subcarrier allocation decisions. Comparing the results when setting $\delta = 10^{-4}$ and $\delta = 10^{0}$, the number of allocated subcarriers differs in grids 2, 14, 21, and 24.

The performance of the proposed iterative LP rounding algorithm is analysed in Fig. 6.5. Although the maximum number of iterations is upper-bounded by $I \times K$, as alluded in Section 6.2.2, in practice, the stopping criteria is satisfied after solving a limited number of LP problems as shown in Fig. 6.5(a). Moreover, Fig. 6.5(b) presents the optimal gap of the iterative LP rounding algorithm by comparing it with the globally optimal solution solved by Gurobi [67]. Numerically, the optimality gap of the proposed method is at least 2% when the robustness parameter is 10^{-4}, and 22% at most when the robustness parameter is $10^{-2.5}$. However, as shown in Section (6.2.2), the complexity of the proposed algorithm is in polynomial time, in contrast to the exponential worst-case complexity of Gurobi [67]. Besides, it can be observed that the optimality gap tends to be larger when the solution of (6.7) is more sensitive to the robustness parameter δ. Considering the iterative LP rounding algorithm is employed to generate a feasible integer solution based on the solution of the linear relaxation, when the problem (6.7) is more sensitive to the robustness parameter δ, even a minor deviation during this rounding process can result in a

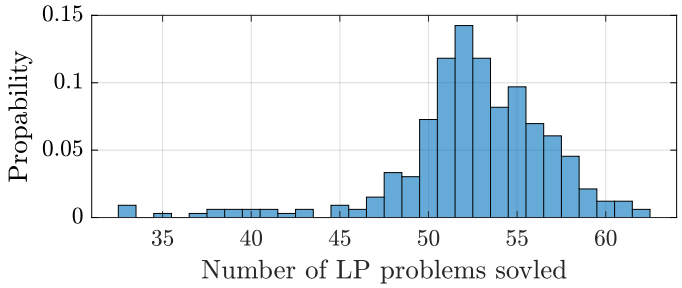

(a) Convergence behaviour of the proposed algorithm.

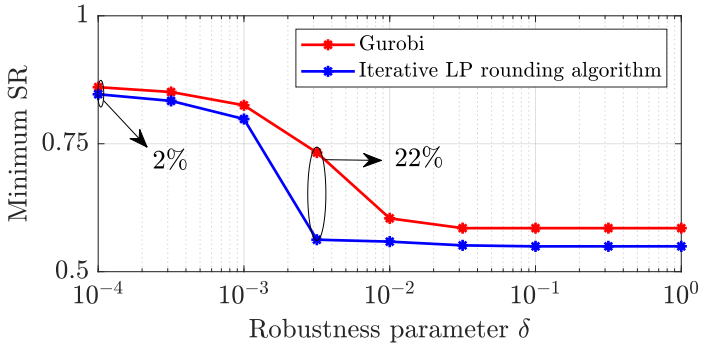

(b) Optimality gap of the proposed algorithm.

Fig. 6.5 Performance analysis of the iterative LP rounding algorithm.

significant gap from the optimal results. This explains why the largest optimality gap shows at $\delta = 10^{-2.5}$.

In conclusion, a flexible ISAC system assisted by RABS is proposed in this section. To represent the users' mobility and changing channel conditions, the grid-based model is employed to characterise the spatial traffic distribution. A robust optimisation problem is formulated on the cardinality constrained uncertainty set to determine the RABS deployment and resource allocation. which is reformulated as a MILP via duality theory and solved by a proposed iterative LP rounding algorithm in polynomial time. Numerical results indicate that the conservatism of the solution can be controlled by changing the value of the robustness parameter, i.e., a more conservative solution under the condition that most users experience poor channel conditions can be obtained by setting a greater robustness parameter. Also, compared to the randomly deployed ground base station, RABS can improve the minimum SR by 28.61% on average thanks to the flexible mobility.

6.3 Swarm of RABSs for mmWave Multi-Hop Backhauling

Network densification is inevitably required to satisfy the rapidly growing traffic demands in future 6G networks. However, a well-recognised predicament that this process entails is the high capital and operational expenditure cost. With this in mind, RABSs are introduced as a flexible and cost-effective solution to densify the network. However, unlike terrestrial base stations connecting with the core network through a high-capacity fibre link, RABSs require wireless backhaul due to their frequent movement. Therefore, this section builds upon this concept and proposes a novel multi-hop backhaul network operated by a swarm of RABSs for efficient network densification.

To satisfy the rapidly growing traffic demand in mobile networks, the use of a millimetre wave (mmWave) spectrum is expected to offer high-throughput wireless access. The authors in [156] verify the feasibility of deploying fixed mmWave ultra-dense outdoor small cells installed on street-level fixtures, e.g., streetlights, lampposts and/or rooftops. The works [157] utilise the wall-mounted mmWave base station to provide line-of-sight (LoS) coverage in urban environments. The benefits of mmWave backhauling come with the cost of considerably higher propagation losses, resulting in a reduced transmission range compared to sub-6 GHz networks. This limitation can be addressed by establishing a multi-hop topology using relay nodes. In a closely related work, the resource allocation for multi-hop backhaul networks is optimised according to the traffic demands in [158, 159]. In [160], by deploying small cells densely on a Manhattan-type geometry, the network flow of the backhaul network is maximised by route formation. An optimal route scheduling strategy is proposed in [161] to maximise the number of flows satisfying the LoS and transmission rate requirements. Furthermore, to address the fluctuations in dynamic traffic, several studies employ UAVs as movable base stations to perform wireless backhaul tasks. For instance, the authors of [162] measure the system performance when considering both the heterogeneous mobility of blockers and UAVs. The utility function of a UAV-assisted multi-hop backhaul network is maximised in [163] and the authors of [164] study the deployment strategy for UAVs.

In this section, a flexible mmWave multi-hop backhaul network operated by a swarm of RABSs is proposed. The approach is inspired by and developed from the work in [160]. This section mainly demonstrates how movable RABSs can enhance the system performance, especially in a heterogeneous and dynamic environment.

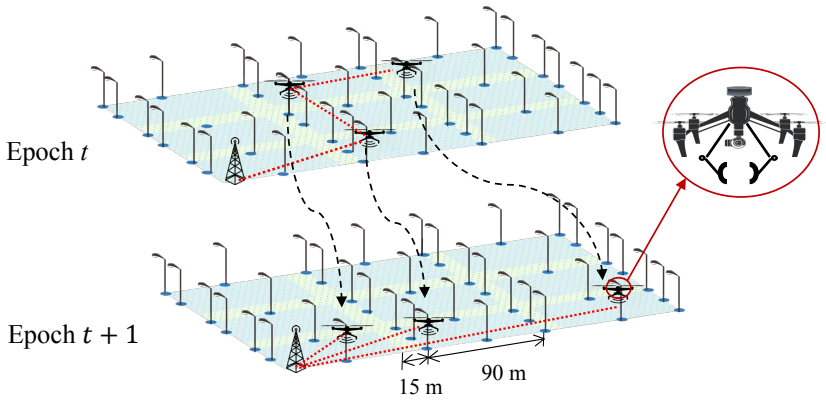

Fig. 6.6 A mmWave backhaul network constructed by a swarm of RABSs: blue squares represent obstacles, the small blue circles are the candidate locations, the red and black lines represent the backhaul channels and the flying trajectory when relocating.

Specifically, the contribution of this section is summarised as follows. Firstly, to overcome the endurance issue of the conventional UAV base stations studied in [162–164], a flexible backhaul network configuration operated by a swarm of RABSs is studied in this section. It could prolong the service time because the grasping power is much lower than the hovering/flying power of conventional hovering-based UAV base stations [27]. Secondly, instead of the uniform traffic distribution assumed in [160, 159], this section focuses on the heterogeneous distribution and dynamic changes of traffic demand in spatial and temporal domains [133]. Furthermore, thanks to their inherent grasping and flying capabilities, RABSs can establish a backhaul network while anchoring on lampposts and relocate their grasping positions to adapt to traffic dynamics. Simulation results demonstrate that only half the number of RABSs is required to meet the same volume of traffic demands compared to densely deployed small base stations. Thirdly, a mixed-integer linear fractional programming (MILFP) is formulated to maximise energy efficiency, defined as the ratio of achievable network flow to energy consumption, by determining the optimal deployment, movement, and multi-hop routing of RABSs. A two-stage method, which includes the column generation technique, the truncated Bellman-Ford algorithm, and the total unimodularity analysis, is proposed to efficiently solve the problem. Simulation results demonstrate that the proposed method achieves a favourable trade-off between high solution quality and low computational complexity.

6.3.1 System Model and problem formulation

The set of all candidate locations for RABSs grasping is denoted as $\mathcal{V}$. A Manhattan-type map is characterised by a graph $\mathcal{G} = (\mathcal{V}^a, \mathcal{E})$, where $\mathcal{V}^a = \{0\} \cup \mathcal{V}$ and 0 is the index of the macro base station (MBS), $\mathcal{E}$ is the set of edges, where the two endpoints can be connected through an unobstructed link. Because the mmWave transmission is dominated by LoS links, the backhaul connections cannot be successfully established when obstructed by buildings. Therefore, as shown in Fig. 6.6, RABSs deployed in the middle of a street have links along and across the street, and RABSs on the corners have diagonal links.

Even if the link between two RABSs is not obstructed by buildings, communication between them is inevitably occasionally blocked by vehicles or other human activities, as RABSs are fixed on lampposts and work at relatively low altitudes. Therefore, the authors of [165, 166] suggest that the probabilistic LoS channel model should be employed for UAVs operating at low altitudes, because this channel model accounts for the fact that the probability of LoS is location-dependent in urban areas, i.e., LoS links are more likely to be obstructed by human activities as the distance between RABSs increases. Hereafter, the achievable data rate is calculated based on the probabilistic LoS channel model. Suppose that whether the backhaul link (i, j) is LoS or NLoS follows a Bernoulli distribution and the LoS probability is given by $p^{\text{LoS}}_{(i,j)} = \min(18/d_{(i,j)}, 1)(1 - \exp(-d_{(i,j)}/36)) + \exp(-d_{(i,j)}/36)$ in 3GPP TR 38.901 [167]. Accordingly, the expected data rate can be averaged as follows [159, 165, 166],

$$R_{(i,j)} = p^{\text{LoS}}_{(i,j)} R^{\text{LoS}}_{(i,j)} + (1 - p^{\text{LoS}}_{(i,j)}) R^{\text{NLoS}}_{(i,j)}, \tag{6.13}$$

where $R^{\text{LoS}}_{(i,j)}$ and $R^{\text{NLoS}}_{(i,j)}$ are the data rate for LoS and NLoS links, respectively, and can be calculated by the following (6.14)[160],

$$R^{\zeta}_{(i,j)} = B \min[\log_2(1 + 10^{0.1 \times (\mathsf{SNR}^{\zeta}_{(i,j)} - 3)}), \mathsf{SE}_{\max}], \quad \zeta \in \{\text{LoS, NLoS}\}, \tag{6.14}$$

where B is the available bandwidth, $\mathsf{SE}_{\max}$ is the maximum spectral efficiency in bps/Hz, ζ indicates whether the link is LoS or NLoS, and $\mathsf{SNR}^{\zeta}_{(i,j)}$ is the signal-to-noise ratio in dB. Besides, dividing the entire serving time of RABSs into T epochs with an equal duration denoted by η, the required traffic demand at candidate location $i \in \mathcal{V}$ at epoch t is denoted by D^t_i in bps. During each epoch, there are N RABSs available to construct a multi-hop backhaul network to relay traffic to the MBS based on the spatial traffic distribution. When the traffic pattern changes in the

subsequent time epoch, RABSs could relocate to establish a new network topology. The application scenario is depicted in Fig. 6.6.

As noted in [160], whilst extending the coverage radius, multi-hop backhauling brings an additional challenge due to the increased latency for every hop. To satisfy the latency requirements, the maximum allowed hop needs to be limited and is denoted by H. All feasible routes are traversed satisfying the hop constraints H, flowing from a candidate location and terminating at the MBS, and denote the set of them as $\mathcal{P}$. To formulate the problem, three sets of variables are introduced as follows. The binary variable $x_i^t \in \{0,1\}$ indicates if the candidate location i is selected to deploy an RABS at epoch t. The variables $y_{(i,j)}^{(t-1,t)}$ represents whether an RABS will fly from the lamppost i to j between two adjacent epochs, $t-1$ and t. The continuous variable f_p^t denotes the volume of traffic flow in the route $p \in \mathcal{P}$ at epoch t. Accordingly, the energy efficiency metric is defined as follows,

$$\mathsf{EE} = \frac{\sum_{t=1}^{T} \sum_{p \in \mathcal{P}} \eta f_p^t}{\sum_{t=0}^{T} \sum_{(i,j) \in \mathcal{E}} E_{(i,j)}^{\text{fly}} y_{(i,j)}^{(t-1,t)} + NT(E^t + E^g)}, \tag{6.15}$$

where $E_{(i,j)}^{\text{fly}}$ denotes the propulsion energy consumed by an RABS flying from the candidate location i to j, while E^t and E^g denote the transmission and grasping energy, respectively. It can be observed that the numerator and denominator of (6.15) calculate the achievable network flow in bits and the total energy consumption in Joule, respectively. Furthermore, there are three sets of constraints used to formulate the problem.

1) Capacity constraints for mmWave channels: Initially, define a subset $\mathcal{P}_{(i,j)} \subseteq \mathcal{P}$ denoting all feasible routes including the edge (i,j). The following constraints should be satisfied,

$$\begin{cases} \sum\limits_{p \in \mathcal{P}_{(i,j)}} f_p^t \leq x_i^t R_{(i,j)}, \ \forall (i,j) \in \mathcal{E}, \forall t \in \{1,...,T\}, & \text{(6.16a)} \\ \sum\limits_{p \in \mathcal{P}_{(i,j)}} f_p^t \leq x_j^t R_{(i,j)}, \ \forall (i,j) \in \mathcal{E}, \forall t \in \{1,...,T\}. & \text{(6.16b)} \end{cases}$$

The right-hand side (RHS) of (6.16) indicates that only when both candidate locations i and j are deployed with RABSs, the traffic can traverse the edge (i,j), and the accumulated flows, calculated by the left-hand side (LHS) of (6.16), would not exceed the maximum value $R_{(i,j)}$.

2) Traffic demand constraints: The following constraints guarantee that all flow sourcing from the candidate location i would not exceed its traffic demand,

$$\sum_{p\in\mathcal{P}_i} f_p^t \leq x_i^t D_i^t,\ \forall i \in \mathcal{V}, \forall t \in \{1,...,T\}, \tag{6.17}$$

where $\mathcal{P}_i$ is a subset of $\mathcal{P}$ indicating all feasible routes sourcing from the candidate location i.

3) Degree constraints for RABSs relocating and deployment: Similar to the constraints (5.5), the following degree constraints to link the RABSs relocating process and deployment should be satisfied,

$$\begin{cases} \sum_{i\in\mathcal{V}} y_{(i,j)}^{(t,t+1)} = x_i^t,\ \forall i \in \mathcal{V}, \forall t \in \{0,1,...,T-1\}, & \text{(6.18a)} \\ \sum_{i\in\mathcal{V}} y_{(i,j)}^{(t-1,t)} = x_j^t,\ \forall j \in \mathcal{V}, \forall t \in \{1,2,...,T\}, & \text{(6.18b)} \end{cases}$$

where (6.18a) depicts whether the RABS departs from the candidate location i or not, while (6.18b) indicates the landing process.

Based on the above preliminaries, the energy efficiency maximisation problem can be formulated as follows,

$$\max_{\{x_i^t\},\{y_{(i,j)}^{(t-1,t)}\},\{f_p^t\}} \quad \mathsf{EE} \tag{6.19a}$$

$$s.t.\ (6.16), (6.17), (6.18), \tag{6.19b}$$

$$\sum_{i\in\mathcal{V}} x_i^t \leq N,\ \forall t \in \{1,2,...,T\}, \tag{6.19c}$$

$$x_i^t \in \{0,1\},\ \forall i \in \mathcal{V}, \forall t \in \{1,2,...,T\}, \tag{6.19d}$$

$$y_{(i,j)}^{(t-1,t)} \in \{0,1\},\ \forall (i,j) \in \mathcal{E}, \forall t \in \{1,2,...,T\}, \tag{6.19e}$$

$$f_p^t \geq 0,\ \forall p \in \mathcal{P}, \forall t \in \{1,2,...,T\}, \tag{6.19f}$$

where the constraints (6.19c) indicate that there are at most N RABSs that can be deployed. It can be observed that the problem (6.19) is a MILFP. Although the Lemma 4 in [168] proves that the MILFP can be solved to optimality via Dinkelbach's algorithm, solving (6.19) is still challenging for the following two main reasons. First, a mixed integer linear programming needs to be solved at each iteration of Dinkelbach's algorithm, which is still NP-hard. Second, the scale of the problem (6.19) grows sharply because the cardinality of the set $\mathcal{P}$, denoted by $|\mathcal{P}|$, increases

exponentially as H and $|\mathcal{V}|$ increase. To this end, a two-stage method is developed in the following Section 6.3.2 to overcome the curse of dimensionality.

6.3.2 The Proposed Two-stage Method

The problem (6.19) is decoupled into two sub-problems and solved separately. Firstly, the traffic flow on the backhaul network is maximised via column generation and the truncated Bellman-Ford algorithm, and then the energy consumption is minimised through linear programming by exploring the total unimodularity structure of the problem.

Hereafter the numerator of (6.15), i.e., the accumulated traffic flow of the backhaul network, is maximised. Observe that when only the traffic flow is considered, the problem can be decoupled into T sub-problems for each epoch and solved separately. Numerically, the network flow maximisation problem for epoch t can be simplified from (6.19) as,

$$\max_{\{x_i^t|\forall i\in\mathcal{V}\},\{f_p^t|\forall p\in\mathcal{P}\}} \sum_{p\in\mathcal{P}} \eta f_p^t \tag{6.20a}$$

$$s.t. \sum_{p\in\mathcal{P}_{(i,j)}} f_p^t \leq x_i^t R_{(i,j)},\ \forall (i,j)\in\mathcal{E}, \tag{6.20b}$$

$$\sum_{p\in\mathcal{P}_{(i,j)}} f_p^t \leq x_j^t R_{(i,j)},\ \forall (i,j)\in\mathcal{E}, \tag{6.20c}$$

$$\sum_{p\in\mathcal{P}_i} f_p^t \leq x_i^t D_i^t,\ \forall i\in\mathcal{V}, \tag{6.20d}$$

$$\sum_{i\in\mathcal{V}} x_i^t \leq N, \tag{6.20e}$$

$$x_i^t \in \{0,1\},\ \forall i\in\mathcal{V}, \tag{6.20f}$$

$$f_p^t \geq 0,\ \forall p\in\mathcal{P}. \tag{6.20g}$$

The main challenge for solving (6.20) is the extremely large sise of the set $\mathcal{P}$. Fortunately, there is a key observation that only a limited number of routes in $\mathcal{P}$ will be activated when solving (6.20). Therefore, the column generation approach is employed to activate a subset of routes in $\mathcal{P}$ iteratively [169].

The column generation is employed to solve the linear relaxation of (6.20), which is denoted as (6.20-LR) for ease of notation. Select and activate a subset $\mathcal{P}'\subseteq\mathcal{P}$, and relax the binary variables in (6.20f) into continuous variables. This problem is

referred to as the restricted master problem for (6.20-LR) and can be written as,

$$\max_{\{x_i^t|\forall i\in\mathcal{V}\},\{f_p^t|\forall p\in\mathcal{P}'\}} \sum_{p\in\mathcal{P}'} \eta f_p^t \tag{6.21a}$$

$$s.t. \sum_{p\in\mathcal{P}'_{(i,j)}} f_p^t \le x_i^t R_{(i,j)},\ \forall (i,j)\in\mathcal{E}, \tag{6.21b}$$

$$\sum_{p\in\mathcal{P}'_{(i,j)}} f_p^t \le x_j^t R_{(i,j)},\ \forall (i,j)\in\mathcal{E}, \tag{6.21c}$$

$$\sum_{p\in\mathcal{P}'_i} f_p^t \le x_i^t D_i^t,\ \forall i\in\mathcal{V}, \tag{6.21d}$$

$$\sum_{i\in\mathcal{V}} x_i^t \le N, \tag{6.21e}$$

$$0\le x_i^t\le 1,\ \forall i\in\mathcal{V}, \tag{6.21f}$$

$$f_p^t\ge 0,\ \forall p\in\mathcal{P}', \tag{6.21g}$$

where $\mathcal{P}'_{(i,j)}$ and $\mathcal{P}'_i$ is the activated subset corresponding to $\mathcal{P}_{(i,j)}$ and $\mathcal{P}_i$, respectively. Problem (6.21) is a linear programming and its dual can be written as,

$$\min_{\substack{\{\alpha_{ij}\},\{\beta_{ij}\},\\ \{\gamma_i\},\{\delta\},\{\zeta_i\}}} N\delta+\sum_{i\in\mathcal{V}}\zeta_i \tag{6.22a}$$

$$s.t. \sum_{(i,j)\in p} (\alpha_{ij}+\beta_{ij})+\gamma_{s_p}\ge\eta,\ \forall p\in\mathcal{P}', \tag{6.22b}$$

$$\sum_{j\in\mathcal{V}} (R_{(i,j)}\alpha_i j+R_{(j,i)}\beta_{ji})+D_i^t\gamma_i\le\delta+\zeta_i,\forall i\in\mathcal{V}, \tag{6.22c}$$

$$\alpha_{ij}\ge 0,\beta_{ij}\ge 0,\gamma_i\ge 0,\delta\ge 0,\zeta_i\ge 0,\ \forall i,j, \tag{6.22d}$$

where $\{\alpha_{ij}\},\{\beta_{ij}\},\{\gamma_i\},\{\delta\}$ and $\{\zeta_i\}$ are dual variables corresponding to the constraints in (6.21), $(i,j)\in p$ indicates that the route p passes through the edge (i,j), and $s_p\in\mathcal{V}$ denotes the source node of the route p. Problem (6.22) is normally referred to as the pricing problem. According to the nominal principle of column generation, the following Lemma 1 always holds.

Lemma 1: If the constraints (6.22b) are even satisfied for all $p\in\mathcal{P}$ (i.e., not only for $p\in\mathcal{P}'$), the result solved from the problem (6.21) with the restricted subset $\mathcal{P}'$ is optimal for (6.20-LR).

Proof: Denote the optimal solution for the problem (6.20-LR), (6.21) and (6.22) as OPT(6.20-LR), OPT(6.21) and OPT(6.22), respectively.

$$\mathsf{OPT}(6.22)\overset{(a)}{=}\mathsf{OPT}(6.21)\overset{(b)}{\le}\mathsf{OPT}(6.20\text{-LR}), \tag{6.23}$$

Algorithm 7 Maximise Traffic Flow via Column Generation

Initialise a restricted subset $\mathcal{P}' \subseteq \mathcal{P}$.
repeat
  Solve the pricing problem (6.22).
  Initialise the value of $u_i^{(0)}, \forall i \in \mathcal{V}^a$ by (6.24).
  repeat
    Update the value of $u_i^{(m+1)}$ via (6.25).
  until $m = H-1$.
  for all $i \in \mathcal{V}$ **do**
    if $u_i^{(H)} < \eta - \gamma_i$ **then**
      Add this shortest path to $\mathcal{P}'$.
    end if
  end for
until No path is added to $\mathcal{P}'$ in this iteration.
Solve (6.21) with the restricted subset $\mathcal{P}'$ and denote the result as $\{f_p^{t*}\}$. This solution is also optimal for (6.20-LR).
repeat
  repeat
    Select the route p with the probability f_p^{t*}/D_i^t.
  until The number of candidate locations that passed by the chosen routes is equal to N.
until The maximum number of iterations k^{max}.

where (a) holds because of the strong duality of the LP problem (6.21), and (b) holds because $\mathcal{P}'$ is a restricted subset of $\mathcal{P}$. If the constraints (6.22b) are satisfied for all $p \in \mathcal{P}$, it means these dual values are feasible for the set $\mathcal{P}$. Because these dual values have been maximised when solving the problem (6.22), the equivalence in (b) will be guaranteed. This completes the proof of Lemma 1 and [169] proves Lemma 1 via the concept of reduced cost. □

Lemma 1 illustrates that if there exists a route $p \in \mathcal{P}$ violating the constraints (6.22b), the objective value (6.21a) can be further improved by adding this route to $\mathcal{P}'$ and re-solve the problem (6.21). Otherwise the optimal solution of (6.20-LR) can be achieved with the restricted route set $\mathcal{P}'$.

However, an unresolved challenge remains after Lemma 1 in determining whether all $p \in \mathcal{P}$ satisfy the constraints (6.22b), or if there is a feasible route p that violates (6.22b). Fortunately, this problem can be efficiently solved by regarding it as a hop-constrained shortest path problem. By analysing the constraints (6.22b), it can be observed that after assigning the weight $(\alpha_{ij}+\beta_{ij})$ to the corresponding edge $(i,j) \in \mathcal{E}$, this problem can be converted to find the shortest path from the MBS to the candidate location $s \in \mathcal{V}$ with maximum H hops. If the shortest path is greater than

or equal to $(\eta-\gamma_s)$, then there is no feasible route sourcing from s and hence violates the constraints (6.22b). Normally, the shortest path problem with hop constraints is also NP-hard. Fortunately, because the weights $(\alpha_{ij}+\beta_{ij})$ assigned to edges are non-negative, forced by (6.22d), the hop-constrained shortest path problem can be solved by modifying the Bellman-Ford algorithm [170]. Denote the shortest path from the MBS to the candidate location s, subject to the condition that the path contains no more than m edges, by $u_i^{(m)}$. Initialise the values of $u_i^{(m)}$ via the following Eq. (6.24),

$$\begin{cases} u_0^{(1)} = 0, & \text{(6.24a)} \\ u_i^{(1)} = \alpha_{0i} + \beta_{0i}, \text{ if } (0,i) \in \mathcal{E}, & \text{(6.24b)} \\ u_i^{(1)} = \infty, \text{ if } (0,i) \notin \mathcal{E}. & \text{(6.24c)} \end{cases}$$

It should be noted that the MBS is indexed by 0. The value of $u_i^{(m)}$ can be updated as follows,

$$u_i^{(m+1)} = \min\left\{u_i^{(m)}, \min_{(j,i)\in\mathcal{E}}\{u_j^{(m)} + \alpha_{ji} + \beta_{ji}\}\right\}. \tag{6.25}$$

Because of the hop constraints, the updating of (6.25) should be stopped when $m+1$ is equal to the hop limit H. The length of the shortest path from the candidate location i to the MBS, satisfying the maximum hop constraints, is then obtained by the value of $u_i^{(H)}$. The obtained feasible shortest path would be added to the set $\mathcal{P}'$ if $u_i^{(H)} < \eta-\gamma_i$. Otherwise, there is no feasible route sourcing from i that should be added to $\mathcal{P}'$. According to Lemma 1, the process of column generation would be terminated until the shortest path from all the locations $i \in \mathcal{V}$ is no less than $(\eta-\gamma_i)$.

Although the aforementioned column generation method can reduce the problem scale, the achieved result is optimal for the problem (6.20-LR). A random rounding method is then proposed to generate an integer solution for (6.20). Denote the optimal solution for (6.20-LR) by $\{f_p^{t\,*}\}$, set the probability of route p being selected as $f_p^{t\,*}/D_i^t$, and pick these routes one by one with this probability distribution until the number of candidate locations they passed is equal to N, forced by the constraint (6.20e). Afterwards, repeat this random rounding process k^{max} times and choose the best result.

After maximizing the served traffic via the column generation approach, the energy consumption is subsequently minimised, shown as the denominator of (6.15).

The problem can be written from (6.19) as,

$$\max_{\{y_{(i,j)}^{(t-1,t)}\}} \sum_{(i,j)\in\mathcal{E}} E_{(i,j)}^{\text{fly}} y_{(i,j)}^{(t-1,t)} + NT(E^t + E^g) \tag{6.26a}$$

$$s.t.\ (6.18), (6.19e). \tag{6.26b}$$

It should be noted that the RHS of (6.18a)-(6.18b) has been solved in Section 6.3.2. Also, it can be observed that (6.26) is still an integer linear programming. Fortunately, the following Lemma 2 proves that the optimal solution for (6.26) can be achieved by solving its linear relaxation.

Lemma 2: The set of constraints (6.18) is totally unimodular.

Proof: The constraints (6.18) can be written as follows,

$$\begin{cases} \sum_{i\in\mathcal{V}} y_{(i,j)}^{(t,t+1)} = x_i^t,\ \forall i \in \mathcal{V}, \forall t \in \{0,1,...,T-1\}, & \text{(6.27a)} \\ \sum_{i\in\mathcal{V}} -y_{(i,j)}^{(t-1,t)} = -x_j^t,\ \forall j \in \mathcal{V}, \forall t \in \{1,2,...,T\}. & \text{(6.27b)} \end{cases}$$

The variables $\{y_{(i,j)}^{(t-1,t)}\}$ can be divided into three groups according to their coefficients: (i) Each variable in the set $\{y_{(i,j)}^{(0,1)}\}$ only appears in (6.18a) once and the coefficient is 1. (ii) Each variable in the set $\{y_{(i,j)}^{(t-1,t)} \,|\, \forall t \in \{2,...,T-1\}\}$ appears once in both (6.18a) and (6.18b), and the coefficients are 1 and -1, respectively. (iii) Each variable in the set $\{y_{(i,j)}^{(T-1,T)}\}$ only appears in (6.18b) once and the coefficient is -1. Proposition 2.6 in Section III.1.2 of [84] proves the fact *"If the* $(0,1,-1)$ *matrix A has no more than two nonzero entries in each column, and if* $\sum_j a_{ij} = 0$ *if column j contains two nonzero coefficients, then it is totally unimodular."* Thus, the coefficient matrix for (6.27) is totally unimodular. And proposition 2.1 in [84] shows that *"A matrix obtained by multiplying a row (column) of a totally unimodular matrix by -1 is also totally unimodular."* This completes the proof of Lemma 2. □

Because the Lemma 2 shows that the problem (6.26) includes a set of totally unimodular constraints and binary constraints, the optimal solution can be obtained by solving its linear relaxation, i.e., relax the constraints (6.19e) to $0 \leq y_{(i,j)}^{(t-1,t)} \leq 1$.

6.3.3 Numerical Investigations

The results presented in this section are simulated on a 300×300 m^2 Manhattan-type map as depicted in Fig. 6.6, where there are 9 square buildings with the size 90×90 m^2 and the road width is 15 m. Lampposts are distributed on the roadside that is

Table 6.2 Summary of Notations

Parameters	Value
Carrier frequency and available bandwidth B	73 GHz, 200 MHz
Signal-to-noise ratio $\mathsf{SNR}^{\mathrm{LoS}}_{(i,j)}$, $\mathsf{SNR}^{\mathrm{NLoS}}_{(i,j)}$	Refer to [159]
Maximum spectral efficiency $\mathsf{SE}_{\max}$	4.8 bps/Hz [160]
Flying velocity and propulsion power	18 m/s, 162 W [27]
Transmission and grasping power	10 W, 10 W
Epoch duration η	1 hour

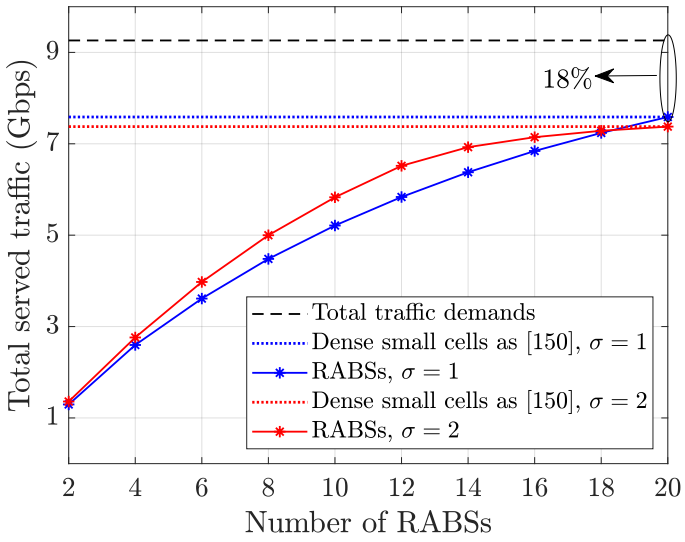

Fig. 6.7 Total traffic demands versus the served traffic volume when $H = 3$.

used for RABSs grasping, as shown in Fig. 6.6. Accordingly, there are 39 candidate locations and 1 MBS. The parameters related to communication and power are summarised in Table 6.2. Similarly to Section 5.2.1, the traffic spatial-temporal distribution model proposed in [133] is used to simulate the traffic demands generated from different candidate locations, where the coefficients of (5.1) are specified by the row of the 'whole area' in the legend of Fig. 5.2(a), and the variance of traffic spatial distribution is denoted by σ in the following simulations. Moreover, it should be noted that all of the following numerical results are averaged by 100 Monte Carlo simulations.

Fig. 6.7 shows the satisfied traffic demand versus the number of RABSs ranging from 2 to 20 at a certain epoch with different deviations of the traffic distribution. Firstly, comparing the served traffic volume versus the total traffic demands, it is shown that deploying only a small group of RABSs can satisfy a large portion of traffic demands. For instance, as marked in Fig. 6.7, selecting 51% candidate

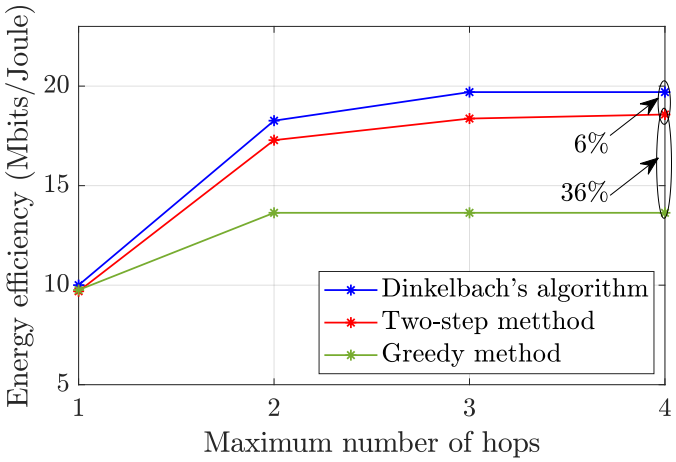

Fig. 6.8 Energy efficiency versus the maximum allowed hops when $N = 10$.

locations, i.e., 20 out of the total 39 locations, to deploy RABSs can meet nearly 82% of the total traffic demand. Secondly, the dotted lines represent the densely deployed small cells studied in [160], that is, deploy small base stations at each candidate location and only determine the route formation. It can be seen that even this dense network cannot satisfy all the traffic demands because of the channel capacity and hop constraints. Also, deploying 20 RABSs can achieve almost the same performance with the dense topology, i.e., using 39 fixed small cells, thanks to their mobility. Thirdly, comparing the results with different σ, it can be observed that for $N \leq 18$ RABS-assisted backhaul network has a better performance when the variance of the traffic demand distribution is increasing.

Fig. 6.8 presents the energy efficiency versus the maximum allowed number of hops solved by different methods. Observe that the energy efficiency grows with the increase of H when $H \leq 3$. The reason is that a larger H brings a wider coverage to the multi-hop networks so that the candidate locations having high traffic demands but far from MBS have the opportunity to offload data to MBS via multi-hop routes. This growth trend reaches a plateau when $N \geq 3$ because RABSs can freely choose the candidate locations with high traffic demand and always backhaul to MBS when H is large enough. Moreover, the proposed two-step method is compared with Dinkelbach's algorithm [168] and the greedy method in Fig. 6.8. It should be noted that although Dinkelbach's algorithm can solve (6.19) optimally, it requires solving a group of NP-hard integer linear programming problems in each iteration, leading to lengthy computational times when dealing with large-scale problems. In contrast, the proposed two-step method only needs to solve linear programming problems in which scale is reduced by the column generation technique in each step, thus

Table 6.3 Problem scale reduced by column generation

H	$\lvert\mathcal{P}\rvert$	$\lvert\mathcal{P}'\rvert$	**Scale reduction**
1	12	12	0%
2	108	66	39%
3	816	177	78%
4	5802	232	96%
5	40128	273	99%

it could improve the computational efficiency at the cost of a 6% optimality gap. Additionally, the greedy method is employed as a benchmark, i.e., at each epoch, it greedily searches the candidate location with the highest traffic volume, calculates the shortest path from the MBS, and adds this shortest path to the solution if it satisfies the hop constraints H, otherwise continues to search for the second-best candidate location. Repeat this process until the requirements for RABS quantities are met. It can be observed in Fig. 6.8 that the two-step method can achieve a higher-quality solution than the greedy method, e.g., exceeding it by 36% when $H = 4$. Therefore, the proposed two-step method achieves a favourable trade-off between high solution quality and low computational complexity.

As mentioned in Section 6.3.2, the main motivation for employing the column generation is to overcome the exponential growth of the number of feasible routes $|\mathcal{P}|$, shown as the second column in Table 6.3. The results in Table 6.3 show the fact that column generation can reduce the problem scale significantly. Numerically, when $H = 5$, there are only 273 routes activated in the restricted master problem (6.21), compared to the number of total feasible routes which is 40128. In other words, the problem scale is reduced by 99%. This is consistent with intuition because even though the number of feasible routes grows exponentially with an increase in H, the number of RABSs restricts that only a limited set of feasible routes need to be activated. Therefore, the column generation approach can solve the problem (6.20-LR) to optimality with a restricted subset $\mathcal{P}'$ so that it can improve the efficiency for solving large-scale problems.

In conclusion, a novel optimisation framework is proposed in this section for network densification via a swarm of RABSs that construct an efficient mmWave network topology for backhauling. To this end, a mixed-integer linear fractional programming problem is formulated and solved by a two-stage method that involves column generation, the Bellman-Ford algorithm and linear programming. Numerical investigations reveal that compared to fixed small cells, only half of RABSs are required to cover the same volume of traffic demand by being able to follow the

spatio-temporal traffic dynamics. Hence, RABSs could propel efficient network densification by offering a dramatic reduction in the number of network elements (i.e., small cells) that are required to serve a given traffic demand.

6.4 Conclusion

In this chapter, RABS is integrated into the novel applications in next-generation networks, aiming to answer the question that which benefits this novel concept can bring to cellular networks. Specifically, in Section 6.2, RABS is utilised to perform both sensing and communication functions simultaneously, while in Section 6.3, a swarm of RABSs construct an efficient mmWave network topology for backhauling. Through these two studies, RABS demonstrates the advantage of its flexibility. In other words, RABS can dynamically track hotspot areas on a finer time scale, such as half an hour or an hour, compared to conventional ground base stations that are difficult to relocate flexibly and can only consider traffic distribution on coarser time scales during planning. Overall, RABS is expected to bring more flexibility and agility to next-generation applications in both spatial and temporal domains. However, compared with ground base stations, RABS also shows the following shortcomings that require further research.

- Firstly, the payload of the UAV limits RABS to carry large-size antenna arrays. Although operating in higher frequencies helps reduce the antenna size, complex hardware equipment is still required to perform advanced wireless technologies.

- Secondly, the serving performance of RABS is constrained by the capacity of wireless backhaul links, which is not a main consideration for conventional fiber-backhauled ground base stations. Therefore, this imposes extra computational complexity on resource allocation and system design for RABS.

- Lastly, although RABS has advantages in energy efficiency compared to other types of ABS, as demonstrated in Chapter 4, the capacity of onboard batteries is still one of the main limitations and bottlenecks. For example, in Section 6.3, the flight path of RABS needs to be specially designed to reduce energy consumption when relocating, which undoubtedly brings extra complexity when designing the RABS serving strategies.

In summary, although research and applications of RABS still face several challenges, there is no doubt that it indeed brings next-generation applications with more flexibility, thereby enhancing system performance effectively.

Chapter 7

Conclusions and Future Work

7.1 Conclusions

In the context of future 6G cellular networks, aerial base stations (ABSs) are expected to play a crucial role due to their inherent advantages, such as high mobility, flexible 3D deployment, and dominant line-of-sight (LoS) channel conditions. However, deploying such new wireless devices also brings several unprecedented challenges. In this thesis, the conflicting evaluation metrics are first investigated in aerial networks, i.e., age of information (AoI) and energy consumption. Subsequently, a novel ABS model, that is, robotic aerial base stations (RABSs), is proposed to overcome the endurance issues of conventional ABSs and densify the network in an efficient manner. The contributions of this thesis are summarised as follows.

Chapter 3 investigates UAV-assisted trajectory planning for data collection tasks, optimizing both average Age of Information (AoI) and aggregate energy consumption. To capture the trade-off between these metrics and identify the Pareto frontier, a multi-return-allowed serving mode is proposed. This mode enables the UAV to return to the depot at any point during the service cycle and is formulated as a multi-objective mixed-integer linear programming (MILP) problem with flow-based constraints, and solved via Bender's decomposition to distribute the computational burden. Additionally, a more general trajectory planning is studied where the UAV can communicate while flying to further enhance performance. Numerical results demonstrate that the proposed multi-return-allowed mode reveals the trade-off between the competing metrics.

To densify the network in an energy-efficient manner, a novel ABS prototype named robotic aerial base stations (RABSs) is proposed, which are equipped with dexterous end effectors able to grasp onto tall urban landforms. In Chapter 4, the

system architecture of RABSs is discussed in both hardware and communication aspects by gearing two previously disconnected areas, namely non-terrestrial communications and robotic dexterous end effectors with grasping capabilities. Compared with existing ABS solutions such as hovering-based, tethered and laser-powered ABSs, RABSs are shown to be able to provide long-term and flexible wireless service in an energy-efficient, weather-independent and environmentally friendly manner.

Chapter 5 studies the optimal deployment and operation for a group of RABSs. More specifically, when integrated into cellular networks, RABSs can enter sleep mode to conserve energy and dynamically adjust their perching points based on real-time traffic load information. With this consideration, an efficient optimisation model has been formulated to optimally orchestrate the deployment and operation strategy for RABSs based on the underlying traffic demand in the network. To solve the aforementioned problem, a special case with a single RABS and developed a Lagrangian heuristic algorithm to solve it by exploiting the totally unimodularity structure. A polynomial-time method is then proposed to decompose the multi-RABS problem into several single-RABS cases based on the Hungarian algorithm. Numerical investigations demonstrate that RABSs outperform fixed small cells due to their mobility, especially in networks with heterogeneous traffic distributions.

To better explore the application of RABSs, Chapter 6 proposes two novel application scenarios in which RABSs are involved in different types of 6G cellular networks. Firstly, a flexible integrated sensing and communication (ISAC) system assisted by the RABS is studied in Section 6.2. A grid-based model captures users' mobility and changing demand, with a robust programming approach formulated on a cardinality-constrained uncertainty set to determine RABS deployment and resource allocation. After reformulated as a mixed integer linear programming via duality theory, the problem is solved by a proposed iterative linear programming rounding algorithm in polynomial time. Numerical investigations show that the minimum satisfaction rate can be improved by 28.61% on average thanks to the flexible mobility of RABS deployment. Secondly, a novel network densification framework is proposed in Section 6.3, in which a swarm of RABSs construct an efficient mmWave backhauling network topology. To this end, a mixed-integer linear fractional programming (MILFP) is formulated and solved by a two-stage method that involves column generation, the Bellman-Ford algorithm and linear programming. Numerical investigations reveal that compared to fixed small cells, only half of RABSs are required to cover the same volume of traffic demand by adapting to spatio-temporal traffic dynamics. Hence, RABSs could propel efficient

network densification by offering a dramatic reduction in the number of network elements (i.e., small cells) that are required to serve a given traffic demand.

7.2 Researcher Opportunities and Regulation Issues

As studied in the above chapters, RABSs can provide wireless service in a more energy-saving and cost-efficient manner. To explore the full potential that RABS-assisted networks can offer, various potential techniques are illustrated to improve the performance of RABS-assisted networks, provide future research opportunities and point out regulation issues as follows.

7.2.1 Future Researcher Opportunities

1) Reconfigurable intelligent surfaces carried by RABS: Reconfigurable intelligent surfaces (RIS) is an enabling technique to improve the system performance in 6G cellular by reflecting the radio signals intelligently via a large number of controllable reflecting units. Specifically, by adjusting the amplitude and phase shift of the reflected signal by controlling the RIS units, the received signal on the user side, combining the direct and reflection signals, can be then formed passively to achieve a higher signal-to-interference-plus-noise ratio (SINR). Different from the nominal relay system, RIS is a passive beamforming technique and thus does not introduce extra spectrum resource blocks. Moreover, the lightweight and low-cost reflecting units make the RIS a flexible, low-power and cost-efficient paradigm in future cellular networks. The mobility of RABS could introduce increased degrees of freedom, which have not been explored yet, to the RIS system, e.g., RIS can be transported and deployed in the cell edge to cover the users suffering low data rates.

2) Developing experimental simulators and prototypes: Although Chapter 2 reviews that several simulators and prototypes for ABS have been developed to validate system design and algorithms in practical settings, testbeds for RABS still face numerous challenges because of its novel system design. From the perspective of robotics research, RABS is required to detect suitable tall urban landforms for perching in real-time. Therefore, it should be equipped with tactile and/or vision sensors and employ advanced algorithms to detect environmental information. Based on developed prototypes, the feasibility and advantages of RABS in urban environments can be further validated. Similarly, simulators for RABS can also be developed based on the measurement of urban environments, including information on network traffic, suitable grasping locations, and existing ground base stations.

The designed algorithms can be validated on the developed simulator accurately and cost-effectively.

3) Integrated with other non-terrestrial network devices: In the 6G era, non-terrestrial networks (NTNs) are expected to provide seamless coverage to both rural and city areas. RABSs can cooperate with other types of non-terrestrial nodes located at different vertical platforms, such as high-altitude platform stations (HAPSs) at nearly 20-50 km as well as satellites on more than 800 km above the ground, and make it possible to create a dynamic network that covers a wide area and provides enhanced coverage, reliability, and scalability. Such integration also enables RABS to provide a direct connection to remote areas, including areas with difficult terrain or those that are geographically isolated. For example, the devices located in the higher platforms, such as HAPSs and satellites, can be employed as macro BSs. However, due to the long distance and frequent handover of satellites, they are difficult to connect with ground devices with low transmission power, such as mobile users and IoT devices. In this case, RABSs can be deployed much closer to mobile terminals to act as relays and connect with HAPSs or satellites through backhaul links.

4) Integrated access and backhaul (IAB): One of the most critical issues when deploying RABSs as relays is the limited capacity of wireless backhaul links. Due to their inherent mobility, RABSs cannot backhaul through the high-capacity fibre link like most of terrestrial BSs. IAB is a promising technique to enhance the network capacity via allocating limited resources on both access and backhaul links. Normally, there are two types of IAB protocols, namely in-band full-duplex (IBFD) and out-band full-duplex (OBFD). In IBFD mode, both access and backhaul links are connecting on the same frequency carriers simultaneously. Although IBFD mode could improve the spectrum efficiency and does not need to determine the bandwidth allocation strategy, it would introduce extra self-interference when access and backhaul links transmit signals on the same frequencies. In OBFD mode, the access and backhaul links are conducted in orthogonal channels, thus there is no self-interference on the relay side. However, because of the limited spectrum resource, the bandwidth allocation strategies affect the network capacity of the OBFD system significantly. Due to the fact that RABSs could change their perching point, new strategies for joint resource allocation and RABS deployment will need to be introduced to enhance the capacity for both access and backhaul links.

5) Cross-layer optimisation and system design: To demonstrate the flexibility that RABSs bring to cellular networks, most existing research mainly focuses on the network layer, e.g., the optimal operation strategy in Chapter 5 and the routing problem in Section 6.3. By integrating knowledge from multiple layers of the com-

munication protocol stack, including physical, link, and network layers, researchers can explore innovative approaches to optimise the performance of RABS. For example, interference management for RABS is extensive and crucial for ensuring the reliability and efficiency of wireless communication in dynamic networks. By exploring promising techniques such as adaptive beamforming and spectrum management, the network performance of aerial networks can be further enhanced. Furthermore, considering that future networks impose higher requirements on latency, addressing cross-layer optimisation problems poses a new challenge, as existing methods can not solve complex and dynamic problems within an acceptable computation time. In such cases, advanced machine learning and artificial intelligence techniques can be utilised to make agile decisions in dynamic environments.

7.2.2 Regulation Issues

Although the regulation regarding UAV flight and communications have been recently published by several regulators around the world [81], such as the U.S. Federal Aviation Administration (FAA), the UK communications regulator Office of Communications (Ofcom) and the International Civil Aviation Organisation (ICAO), the regulations for RABS need further discussed and published to make sure it can be involved in civil wireless networks.

First, the use of aerial platforms for any application faces increasingly strict - but also increasingly clear - regulation. This regulation is motivated primarily by safety issues, to avoid impacting piloted aviation and to reduce risks to people or property from falling debris. Piloted aviation is avoided by regulations that limit the altitude of platforms, and restrict their use entirely in the vicinity of airports. Increasingly these regulations are automated rather than based on human intervention, specifying locations that must be avoided by platforms with GPS or other GNSS location tracking. This approach suits RABS well, which would anyway support a high degree of automation and be aware of their location for capacity-targeting reasons. For example in the UK, UAVs must fly below 120 m in height above local ground level and away from Flight Restrictions Zones in the vicinity of airports and spaceports [171]. These restrictions should be straightforward to meet without significantly affecting the utility of RABS. More problematic is the requirement to always fly more than 50 m horizontal distance from people, including those in buildings, in the case of UAVs above 250 g in weight. It is acceptable for lighter UAVs to fly above people, but this will be hard to attain for practical RABS. Clearly, this area of regulation will need to evolve for RABS to achieve their potential

in offering capacity enhancements in populated areas. Within that context, the successful deployment of robotic small cells heavily depends on the establishment of low-risk aerial urban corridors to enable ubiquitous roaming of aerial small cells within an urban environment so that they can efficiently change their point of attachment based on the spatio-temporal traffic variations.

Secondly, the RABS application of spectrum will need to be supported by local spectrum management regulations. Spectrum regulations are motivated primarily by the need to avoid harmful interference between users, and RABS operation could present a new interference use case. When the RABS are docked this should be unproblematic, as the spectrum would be used in the same way as for a conventional outdoor small cell, and operation would remain under the control of the relevant mobile network operator who would incorporate the RABS into their network planning procedures. When the RABS is in flight between docking locations, the use of access spectrum in mobile bands may be restricted and only allowed when docked, though other locations may permit in-flight operation for even greater RABS applicability. Spectrum for control of the RABS in flight is more likely to be dedicated to this application; the UK communications regulator Ofcom has consulted on introducing a new spectrum license to allow control and transmission of data and video from UAVs [172].

Finally, the creation of formal policies around aerial urban airspace and their corresponding capacity limitations are still at an embryonic stage. Within that context, the successful deployment of RABSs heavily depends on the establishment of low-risk aerial urban corridors to enable the ubiquitous roaming of aerial small cells within an urban environment so that they can efficiently change their point of attachment based on the spatial-temporal traffic variations.

Appendix A

Propulsion Power Model for Unmanned Aerial Vehicles

In this appendix, the derivation of the propulsion power model for unmanned aerial vehicles (UAVs) is reviewed to support the research in Chapters 3 to 6. Generally speaking, UAVs can be divided into two categories in terms of their wing configuration, i.e., fixed-wing and rotary-wing UAVs. Fixed-wing UAVs always have a higher maximum flying speed and greater payloads. However, they require a runway or launcher for takeoff and landing, and cannot keep hovering at a fixed position. Conversely, rotary-wing UAVs possess the capability for vertical takeoff and landing, as well as the ability to maintain a stationary position while hovering. Hereafter, the closed-form expressions of the propulsion power for fixed-wing and rotary-wing UAVs are reviewed, which are proposed in [26, 27, 173, 174].

A.1 Propulsion Power Model for Fixed-wing UAV

The propulsion power model for fixed-wing UAV proposed in [26] is reviewed in this section. The aircraft is assumed to fly along a constant direction and remain at a certain altitude, while the propulsion power model for complex flight trajectories can be found in the textbook [173].

On the horizontal plane, drag is defined as the aerodynamic force component in the direction of the velocity vector. The magnitude of drag is defined in the equation (4.1) in [173],

$$D = \frac{1}{2} C_D \rho S V^2, \tag{A.1}$$

where C_D is the drag force coefficient, S is the area of the wing projected on the ground, and V denotes the aircraft speed. Moreover, the force component perpendic-

ular to drag, directed upwards, is defined as the lift force,

$$L = \frac{1}{2} C_L \rho S V^2, \tag{A.2}$$

where C_L is the lift force coefficient. The common drag equation for the aircraft with subsonic speeds is given by (4.13) in [173],

$$C_D = C_{D_0} + \frac{C_L^2}{e_0 \pi A_r}, \tag{A.3}$$

where e_0 is the Oswald efficiency depending on the spanwise load distribution, and A_r is defined as the ratio of the wing span to its aerodynamic breadth. Introducing (A.2) and (A.3) into (A.1), the drag can be calculated as,

$$D = \frac{1}{2} C_{D_0} \rho S V^2 + \frac{2L^2}{e_0 \pi A_r \rho S V^2}. \tag{A.4}$$

Consider a fixed-wing aircraft flying with an acceleration of a at a constant altitude. The following two equations analyse the forces in the horizontal and vertical directions,

$$\begin{cases} L = W, & \text{(A.5a)} \\ F - D = ma, & \text{(A.5b)} \end{cases}$$

where (A.5a) states that the lift force is equal to the gravitational force in the vertical direction, while (A.5b) represents the force analysis in the horizontal direction, where F is the thrust force produced by the aircraft engine, and m denotes the weight of the UAV in kilograms. Introducing (A.4) and (A.5a) into (A.5b), the following equation could be achieved,

$$F = \frac{1}{2} C_{D_0} \rho S V^2 + \frac{2W^2}{e_0 \pi A_r \rho S V^2} + ma. \tag{A.6}$$

Accordingly, the propulsion for the fixed-wing UAV can be calculated as follows,

$$P = FV = \frac{1}{2} C_{D_0} \rho S V^3 + \frac{2W^2}{e_0 \pi A_r \rho S V} + maV. \tag{A.7}$$

For notational convenience, two parameters are always defined as $c_1 \triangleq \frac{1}{2} C_{D_0} \rho$ and $c_2 \triangleq \frac{2W^2}{e_0 \pi A_r \rho S}$. This completes the derivation of the propulsion power model for fixed-wing UAVs.

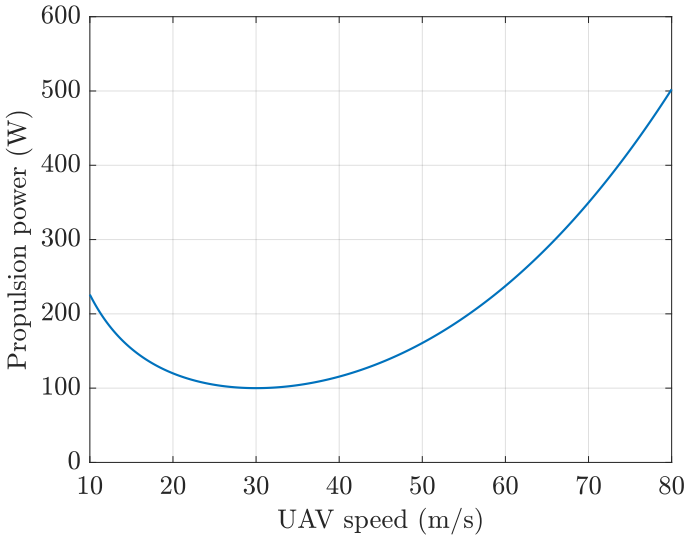

Fig. A.1 Propulsion power versus fixed-wing UAV speed.

The following Fig. A.1 demonstrates the propulsion power versus fixed-wing UAV speed, in which the parameters are from [26], i.e., c_1 and c_2 are set to 9.26×10^{-4} and 2250, respectively.

A.2 Propulsion Power Model for Rotary-wing UAV

The propulsion power model for rotary-wing UAV proposed in [27] is reviewed in this section. The derivation of the flight power of a rotary-wing UAV includes two steps. Considering one of the most significant advantages of rotary-wing UAVs over fixed-wing UAVs is their ability to hover in the air, the hovering power is derived first. Subsequently, the power required for forward flight can be determined under some reasonable approximations. It should be noted that the power required for both hovering and flight is calculated based on the following equation,

$$P = q_c \rho s A \Omega^3 R^3, \tag{A.8}$$

where P is the propulsion power, q_c indicates the torque coefficient that would be further discussed later for different UAV status, ρ, s, A and Ω denote the air density, rotor solidity, rotor disc area and blade angular velocity, respectively.

When rotary-wing UAVs are hovering in the air, the thrust primarily balances the aircraft weight and the torque coefficient q_c is given by the equation (63) in [27],

$$q_c = \frac{\delta}{8} + (1+k)\frac{W^{3/2}}{\sqrt{2}\rho^{3/2}sA^{3/2}\Omega^3 R^3}, \tag{A.9}$$

where W is the gravitational force of aircraft in Newton, δ and k are the profile drag coefficient and incremental correction factor, respectively. Introducing (A.9) into (A.8), the hovering power for rotary-wing UAVs can be calculated by,

$$P_h = \frac{\delta}{8}\rho sA\Omega^3 R^3 + (1+k)\frac{W^{3/2}}{\sqrt{2\rho A}}, \tag{A.10}$$

For notational convenience, the first and second components in (A.10) are indicated by P_0 and P_i, respectively, i.e., $P_0 \triangleq \frac{\delta}{8}\rho sA\Omega^3 R^3$ and $P_i \triangleq (1+k)\frac{W^{3/2}}{\sqrt{2\rho A}}$.

Similarly, the torque coefficient q_c for forward flight is given by the equation (66) in [27],

$$q_c = \frac{\delta}{8}\Big(1+\frac{3V^2}{\Omega^2 R^2}\Big) + \frac{(1+k)F\lambda_i}{\rho sA\Omega^2 R^2} + \frac{1}{2}d_0\frac{V^2}{\Omega^3 R^3}, \tag{A.11}$$

where V, R, and F are the forward speed, rotor radius and rotor thrust, respectively, and λ_i is the mean induced velocity. It is worth noting that the torque coefficient q_c is a function of the forward speed V and the rotor thrust F. Introducing (A.11) to (A.8), the propulsion power for the forward flight can be calculated as,

$$P_f = P_0\Big(1+\frac{3V^2}{\Omega^2 R^2}\Big) + (1+k)Fv_{i0} + \frac{1}{2}d_0\rho sAV^3, \tag{A.12}$$

where $v_{i0} \triangleq \lambda_i \Omega R$ is the mean induced velocity. The textbook [174] indicates that v_{i0} is a function of V and F, and provides a calculation as,

$$v_{i0} = v_0\Big(\sqrt{\tilde{\kappa}^2 + \frac{V^4}{4v_0^4} - \frac{V^2}{4v_0^2}}\Big)^{1/2}, \tag{A.13}$$

where $\tilde{\kappa} \triangleq F/W$ is defined as the thrust-to-weight ratio and $v_0 \triangleq \sqrt{W/(2\rho A)}$ is the mean induced velocity for hovering. Accordingly, the flight power given by (A.12) can be rewritten as,

$$P_f = P_0\Big(1+\frac{3V^2}{\Omega^2 R^2}\Big) + P_i\tilde{\kappa}\Big(\sqrt{\tilde{\kappa}^2 + \frac{V^4}{4v_0^4} - \frac{V^2}{4v_0^2}}\Big)^{1/2} + \frac{1}{2}d_0\rho sAV^3. \tag{A.14}$$

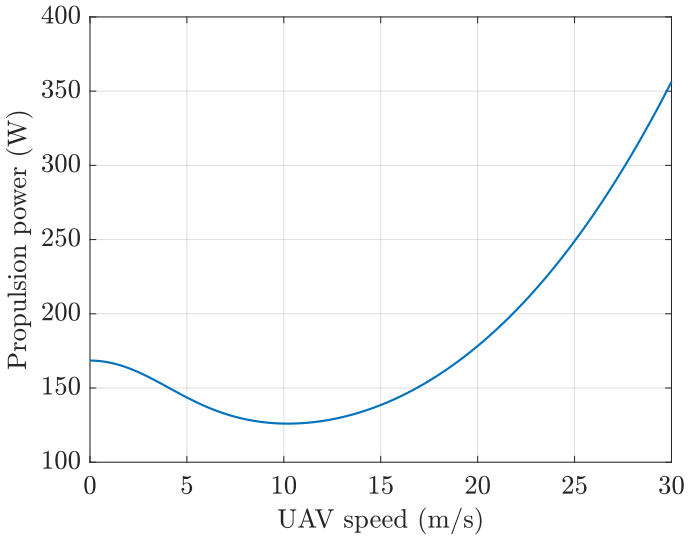

Fig. A.2 Propulsion power versus rotary-wing UAV speed.

As suggested by the textbook [174], the thrust generated by the UAV is always very close to its weight because the aircraft needs to keep balance in the vertical direction, i.e., $F \approx W$ and $\tilde{\kappa} \approx 1$, the propulsion power can be approximated as,

$$P = P_0\left(1+\frac{3V^2}{\Omega^2 R^2}\right) + P_i\left(\sqrt{1+\frac{V^4}{4v_0^4}} - \frac{V^2}{2v_0^2}\right)^{1/2} + \frac{1}{2}d_0\rho sAV^3. \tag{A.15}$$

It should be noted that the flying power (A.15) could converge to the hovering power (A.10) when setting $V = 0$. Therefore, the notation P is used here to indicate both hovering and forward flight power. This completes the derivation of the propulsion power for rotary-wing UAVs.

The following Fig. A.2 presents the propulsion power versus rotary-wing UAV speed, in which the simulation parameters are from [27], i.e., P_0 and P_i are set to 79.86 and 88.63, respectively, the rotor radius R is 0.4 m, the rotor disc area A is 0.503 m^2, mean rotor induced velocity when hovering v_0 is set to 4.03, rotor solidity s is 0.05, fuselage drag ratio d_0 is 0.6, the blade angular velocity Ω is 300 s^{-1}, and the air density is set to 1.225 kg/m^3.

Appendix B

Derivation of the Conditional Mutual Information

In this appendix, the derivation of conditional mutual information (MI) proposed in [140, 141] is reviewed, which is utilised as the performance metric for orthogonal frequency division multiplexing (OFDM) sensing in Chapter 6.

The sensing signal performed on a set of K subcarriers with M consecutive integrated OFDM symbols can be written as,

$$s(t) = e^{j2\pi f_k^c t} \sum_{n=0}^{N_s-1} \sum_{k=0}^{K-1} a_k c_{kn} e^{j2\pi k\Delta f(t-nT_s)} \cdot \text{rect}[\frac{t-nT_s}{T_s}], \tag{B.1}$$

where t is the continuous-time independent variable, f^c and Δf are the frequency and bandwidth of subcarrier k, a_k and c_{kn} denotes the amplitude and phase code, respectively, T_s is the duration of each completed OFDM symbol including both the guard intervals and elementary symbol, and rect$[x]$ is the rectangle function that is equal to one when $x \in [0,1]$, and zero, otherwise.

Accordingly, supposing the impulse response of a sensing target is characterised by $g(t)$ and the impulse response of the propagation channel between the transmitter and target is $h(t)$, the received signal can be written as,

$$y(t) = s(t) * h(t) * g(t) + n(t), \tag{B.2}$$

where $*$ represents the convolution operation and $n(t)$ is additive white Gaussian noise (AWGN) with zero mean and power spectral density $N(f)$. The conditional MI between the target response and the reflected signal conditioned on the sensing probing signal and propagation channel is denoted by $M(y(t); g(t)|\, s(t), h(t))$ and

given by the following (B.3) in [175],

$$M(y(t);g(t)|s(t),h(t)) = \frac{\Delta f N_s T_s}{2} \sum_{k=0}^{K-1} \log_2 \left(1 + \frac{|S(f_k)|^2 |H(f_k)|^2 |G(f_k)|^2}{N(f_k) N_s T_s}\right) \quad \text{(B.3)}$$

where $[f_k, f_{k+1}]$ indicates the frequency interval for the subcarrier k. For the specific subcarrier k, $S(f_k)$, $H(f_k)$ and $N(f_k)$ are approximated by their respective values of the whole signal, i.e., $S(f)$, $H(f)$ and $N(f)$, where $S(f)$ and $G(f)$ are the Fourier transform of $s(t)$ and $h(t)$, respectively. Afterwards, define $Q(f) = |S(f)|^2$ and it can be written as,

$$\begin{aligned} Q(f) =& T_s^2 \cdot \sum_{n=0}^{N_s-1} \sum_{k=0}^{K-1} \sum_{n'=0}^{N_s-1} \sum_{k'=0}^{K-1} a_k a_{k'}^* c_{kn} c_{k'n'}^* \\ & \cdot e^{-j2\pi(f-f_c)(n-n')T_s} \cdot e^{-j\pi(k-k')\Delta f T_s} \\ & \cdot \mathrm{sinc}(\pi(f-f_k)T_s) \cdot \mathrm{sinc}(\pi(f-f_{k'})T_s) \end{aligned} \quad \text{(B.4)}$$

where $(\cdot)^*$ indicates the complex conjugation, and $\mathrm{sinc}(t)$ is the sinc function calculated as $\mathrm{sinc}(t) = \frac{\sin t}{t}$. Generally speaking, the communication code c_{kn} depends on the carried information. By applying the precoding to the transmitted signal [176], the following equation is obtained,

$$\mathbb{E}(c_{kn} c_{k'n'}) = \begin{cases} 1, & k = k', n = n', \\ 0, & \text{otherwise.} \end{cases} \quad \text{(B.5)}$$

where $\mathbb{E}(\cdot)$ calculates the expectation of a random variable. Introducing (B.5) into (B.3), the expectation of $Q(f)$ could be written as,

$$\mathbb{E}(Q(f)) = T_s^2 N_s \sum_{k=0}^{K-1} |a_k|^2 \mathrm{sinc}(\pi(f-f_k)T_s), \quad \text{(B.6)}$$

In practice, the value of $Q(f)$ is reasonable to be approximated via its expectation because the values of N_s and K are generally sufficiently large. Moreover, remember the duration of the OFDM symbol T_s includes the elementary length of the symbol and the guard interval. When $k \neq k'$, the value of $\mathrm{sinc}(\pi(f_k - f_{k'})T_s)$ is equal to zero when there is no guard interval and much less than one when the guard interval is much less than the elementary length. Afterwards, the value of $T_s^2 N_s \sum_{k'=0}^{K-1} |a_{k'}|^2 \mathrm{sinc}(\pi(f_k - f_{k'})T_s)$ can be approximated to zero in most practical cases. Therefore, at the frequency $f = f_k$, the value of $Q(f_k)$ can be approximated

as follows,

$$Q(f_k) \approx T_s^2 N_s |a_k|^2, \tag{B.7}$$

Substituting (B.7) into (B.3), the conditional MI could be calculated by,

$$M(y(t); g(t) | s(t), h(t)) = \frac{\Delta f N_s T_s}{2} \sum_{k=0}^{K-1} \log_2 \Big(1 + \frac{T_s^2 N_s |a_k|^2 |H(f_k)|^2 |G(f_k)|^2}{N(f_k) N_s T_s}\Big). \tag{B.8}$$

In practice, the impulse response $g(t)$ is unknown before detecting the targets. Therefore, the authors of [140] suggest initially estimating $g(t)$ through a preliminary sensing attempt and then designing a more specific resource allocation strategy in subsequent sensing tasks. Also, it should be noted that because the subcarrier allocation is taken into consideration in Section 6.2, the conditional MI for specific subcarrier is calculated separately. This completes the derivation of the conditional MI.

References

[1] Airbus. Zephyr: High Altitude Pseudo-Satellite (HAPS) UAS Solutions. Retrieved from https://www.airbus.com/en/products-services/defence/uas/uas-solutions/zephyr, 2022.

[2] AT&T. Taking 5G to New Heights: AT&T's Drone Program Launches an Industry First with 5G Transmission. Retrieved from https://about.att.com/story/2022/5G-drone-program.html, 2022.

[3] Azade Fotouhi, Haoran Qiang, Ming Ding, Mahbub Hassan, Lorenzo Galati Giordano, Adrian Garcia-Rodriguez, and Jinhong Yuan. Survey on UAV cellular communications: Practical aspects, Standardization Advancements, Regulation, and Security Challenges. *IEEE Communications Surveys & Tutorials*, 21(4):3417–3442, 2019.

[4] Global Times. China's high-tech companies aid Henan flood rescues with drones and satellites. Retrieved from https://www.globaltimes.cn/page/202107/1229309.shtml, 2021.

[5] Cihan Tugrul Cicek, Hakan Gultekin, Bulent Tavli, and Halim Yanikomeroglu. UAV base station location optimization for next generation wireless networks: Overview and future research directions. In *2019 1st International Conference on Unmanned Vehicle Systems-Oman (UVS)*, pages 1–6. IEEE, 2019.

[6] Yong Zeng, Rui Zhang, and Teng Joon Lim. Wireless communications with unmanned aerial vehicles: opportunities and challenges. *IEEE Communications magazine*, 54(5):36–42, 2016.

[7] Jia Ye, Jingping Qiao, Abla Kammoun, and Mohamed-Slim Alouini. Non-terrestrial communications assisted by reconfigurable intelligent surfaces. *Proceedings of the IEEE*, 2022.

[8] Jiangbin Lyu, Yong Zeng, and Rui Zhang. UAV-aided offloading for cellular hotspot. *IEEE Transactions on Wireless Communications*, 17(6):3988–4001, 2018.

[9] Xianzhen Guo, Bin Li, Jiayi Cong, and Ruonan Zhang. Throughput maximization in a UAV-enabled two-way relaying system with multi-pair users. *IEEE Communications Letters*, 25(8):2693–2697, 2021.

[10] Cheng Zhan, Yong Zeng, and Rui Zhang. Energy-efficient data collection in UAV enabled wireless sensor network. *IEEE Wireless Communications Letters*, 7(3):328–331, 2017.

[11] Haiquan Lu, Yong Zeng, Shi Jin, and Rui Zhang. Aerial intelligent reflecting surface: Joint placement and passive beamforming design with 3D beam flattening. *IEEE Transactions on Wireless Communications*, 20(7):4128–4143, 2021.

[12] Nan Cheng, Wenchao Xu, Weisen Shi, Yi Zhou, Ning Lu, Haibo Zhou, and Xuemin Shen. Air-ground integrated mobile edge networks: Architecture, challenges, and opportunities. *IEEE Communications Magazine*, 56(8):26–32, 2018.

[13] Nan Zhao, F Richard Yu, Lisheng Fan, Yunfei Chen, Jie Tang, Arumugam Nallanathan, and Victor CM Leung. Caching unmanned aerial vehicle-enabled small-cell networks: Employing energy-efficient methods that store and retrieve popular content. *IEEE Vehicular Technology Magazine*, 14(1):71–79, 2019.

[14] Weisen Shi, Haibo Zhou, Junling Li, Wenchao Xu, Ning Zhang, and Xuemin Shen. Drone assisted vehicular networks: Architecture, challenges and opportunities. *IEEE Network*, 32(3):130–137, 2018.

[15] Peiran Dong, Xiaojie Wang, Shupeng Wang, Yongjian Wang, Zhaolong Ning, and Mohammad S Obaidat. Internet of UAVs Based Remote Health Monitoring: An Online eHealth System. *IEEE Wireless Communications*, 28(3):15–21, 2021.

[16] Giuseppe Faraci, Christian Grasso, and Giovanni Schembra. Design of a 5G network slice extension with MEC UAVs managed with reinforcement learning. *IEEE Journal on Selected Areas in Communications*, 38(10):2356–2371, 2020.

[17] Tiankui Zhang, Yi Wang, Yuanwei Liu, Wenjun Xu, and Arumugam Nallanathan. Cache-enabling UAV communications: Network deployment and resource allocation. *IEEE Transactions on Wireless Communications*, 19(11):7470–7483, 2020.

[18] Qiqi Ren, Omid Abbasi, Gunes Karabulut Kurt, Halim Yanikomeroglu, and Jian Chen. Caching and computation offloading in high altitude platform station (HAPS) assisted intelligent transportation systems. *IEEE Transactions on Wireless Communications*, 2022.

[19] Faraj Lagum, Irem Bor-Yaliniz, and Halim Yanikomeroglu. Strategic densification with UAV-BSs in cellular networks. *IEEE Wireless Communications Letters*, 7(3):384–387, 2017.

[20] Chao Shen, Tsung-Hui Chang, Jie Gong, Yong Zeng, and Rui Zhang. Multi-UAV interference coordination via joint trajectory and power control. *IEEE Transactions on Signal Processing*, 68:843–858, 2020.

[21] Liang Zhang and Nirwan Ansari. Latency-aware IoT service provisioning in UAV-aided mobile-edge computing networks. *IEEE Internet of Things Journal*, 7(10):10573–10580, 2020.

[22] Juan Liu, Xijun Wang, Bo Bai, and Huaiyu Dai. Age-optimal trajectory planning for UAV-assisted data collection. In *IEEE INFOCOM 2018-IEEE Conference on Computer Communications Workshops (INFOCOM WKSHPS)*, pages 553–558, 2018.

[23] Juan Liu, Peng Tong, Xijun Wang, Bo Bai, and Huaiyu Dai. UAV-aided data collection for information freshness in wireless sensor networks. *IEEE Transactions on Wireless Communications*, 20(4):2368–2382, 2020.

[24] Yong Zeng, Xiaoli Xu, and Rui Zhang. Trajectory design for completion time minimization in UAV-enabled multicasting. *IEEE Transactions on Wireless Communications*, 17(4):2233–2246, 2018.

[25] Zahra Rahimi, Mohammad Javad Sobouti, Reza Ghanbari, Seyed Amin Hosseini Seno, Amir Hossein Mohajerzadeh, Hamed Ahmadi, and Halim Yanikomeroglu. An efficient 3-D positioning approach to minimize required UAVs for IoT network coverage. *IEEE Internet of Things Journal*, 9(1):558–571, 2021.

[26] Yong Zeng and Rui Zhang. Energy-efficient UAV communication with trajectory optimization. *IEEE Transactions on Wireless Communications*, 16(6):3747–3760, 2017.

[27] Yong Zeng, Jie Xu, and Rui Zhang. Energy minimization for wireless communication with rotary-wing UAV. *IEEE Transactions on Wireless Communications*, 18(4):2329–2345, 2019.

[28] Mohammad Taghi Dabiri, Mohsen Rezaee, Vahid Yazdanian, Behrouz Maham, Walid Saad, and Choong Seon Hong. 3D channel characterization and performance analysis of UAV-assisted millimeter wave links. *IEEE Transactions on Wireless Communications*, 20(1):110–125, 2020.

[29] Mohammad Taghi Dabiri, Hossein Safi, Saeedeh Parsaeefard, and Walid Saad. Analytical channel models for millimeter wave UAV networks under hovering fluctuations. *IEEE Transactions on Wireless Communications*, 19(4):2868–2883, 2020.

[30] Javad Sabzehali, Vijay K Shah, Harpreet S Dhillon, and Jeffrey H Reed. 3d placement and orientation of mmwave-based uavs for guaranteed los coverage. *IEEE Wireless Communications Letters*, 10(8):1662–1666, 2021.

[31] Chaoqiong Fan, Changyang She, Hengsheng Zhang, Bin Li, Chenglin Zhao, and Dusit Niyato. Learning to Optimize User Association and Spectrum Allocation with Partial Observation in mmWave-Enabled UAV Networks. *IEEE Transactions on Wireless Communications*, 2022.

[32] Zhenyu Xiao, Hang Dong, Lin Bai, Dapeng Oliver Wu, and Xiang-Gen Xia. Unmanned aerial vehicle base station (UAV-BS) deployment with millimeter-wave beamforming. *IEEE Internet of Things Journal*, 7(2):1336–1349, 2019.

[33] Lipeng Zhu, Jun Zhang, Zhenyu Xiao, Xianbin Cao, Xiang-Gen Xia, and Robert Schober. Millimeter-wave full-duplex UAV relay: Joint positioning, beamforming, and power control. *IEEE Journal on Selected Areas in Communications*, 38(9):2057–2073, 2020.

[34] Hossein Vaezy, Mehdi Salehi Heydar Abad, Ozgur Ercetin, Halim Yanikomeroglu, Mohammad Javad Omidi, and Mohammad Mahdi Naghsh. Beamforming for maximal coverage in mmWave drones: A reinforcement learning approach. *IEEE Communications Letters*, 24(5):1033–1037, 2020.

[35] Zhenyu Xiao, Lipeng Zhu, Yanming Liu, Pengfei Yi, Rui Zhang, Xiang-Gen Xia, and Robert Schober. A survey on millimeter-wave beamforming enabled UAV communications and networking. *IEEE Communications Surveys & Tutorials*, 24(1):557–610, 2021.

[36] Yuanwei Liu, Zhijin Qin, Yunlong Cai, Yue Gao, Geoffrey Ye Li, and Arumugam Nallanathan. UAV communications based on non-orthogonal multiple access. *IEEE Wireless Communications*, 26(1):52–57, 2019.

[37] Jinhui Lu, Yuntian Wang, Tingting Liu, Zhihong Zhuang, Xiaobo Zhou, Feng Shu, and Zhu Han. UAV-enabled uplink non-orthogonal multiple access system: Joint deployment and power control. *IEEE Transactions on Vehicular Technology*, 69(9):10090–10102, 2020.

[38] Ali Arshad Nasir, Hoang Duong Tuan, Trung Q Duong, and H Vincent Poor. UAV-enabled communication using NOMA. *IEEE Transactions on Communications*, 67(7):5126–5138, 2019.

[39] Rui Tang, Julian Cheng, and Zhaoxin Cao. Joint placement design, admission control, and power allocation for NOMA-based UAV systems. *IEEE Wireless Communications Letters*, 9(3):385–388, 2019.

[40] Yu Xu, Tiankui Zhang, Dingcheng Yang, Yuanwei Liu, and Meixia Tao. Joint resource and trajectory optimization for security in UAV-assisted MEC systems. *IEEE Transactions on Communications*, 69(1):573–588, 2020.

[41] Charitha Madapatha, Behrooz Makki, Chao Fang, Oumer Teyeb, Erik Dahlman, Mohamed-Slim Alouini, and Tommy Svensson. On integrated access and backhaul networks: Current status and potentials. *IEEE Open Journal of the Communications Society*, 1:1374–1389, 2020.

[42] Liang Zhang and Nirwan Ansari. A framework for 5G networks with in-band full-duplex enabled drone-mounted base-stations. *IEEE Wireless Communications*, 26(5):121–127, 2019.

[43] Liang Zhang, Qiang Fan, and Nirwan Ansari. 3-D drone-base-station placement with in-band full-duplex communications. *IEEE Communications Letters*, 22(9):1902–1905, 2018.

[44] Liang Zhang and Nirwan Ansari. Approximate algorithms for 3-D placement of IBFD enabled drone-mounted base stations. *IEEE Transactions on Vehicular Technology*, 68(8):7715–7722, 2019.

[45] Liang Zhang and Nirwan Ansari. On the number and 3-D placement of in-band full-duplex enabled drone-mounted base-stations. *IEEE Wireless Communications Letters*, 8(1):221–224, 2018.

[46] Carmen D'Andrea, Adrian Garcia-Rodriguez, Giovanni Geraci, Lorenzo Galati Giordano, and Stefano Buzzi. Cell-free massive MIMO for UAV communications. In *IEEE International Conference on Communications Workshops (ICC Workshops)*, pages 1–6, 2019.

[47] Qingqing Wu, Yong Zeng, and Rui Zhang. Joint trajectory and communication design for multi-UAV enabled wireless networks. *IEEE Transactions on Wireless Communications*, 17(3):2109–2121, 2018.

[48] Fangyu Cui, Yunlong Cai, Zhijin Qin, Minjian Zhao, and Geoffrey Ye Li. Joint trajectory design and power allocation for UAV-enabled non-orthogonal multiple access systems. In *IEEE Global Communications Conference (GLOBECOM)*, pages 1–6, 2018.

[49] Elham Kalantari, Halim Yanikomeroglu, and Abbas Yongacoglu. Wireless networks with cache-enabled and backhaul-limited aerial base stations. *IEEE Transactions on Wireless Communications*, 19(11):7363–7376, 2020.

[50] Mohammad Mozaffari, Walid Saad, Mehdi Bennis, and Mérouane Debbah. Mobile internet of things: Can UAVs provide an energy-efficient mobile architecture? In *IEEE global communications conference (GLOBECOM)*, pages 1–6, 2016.

[51] Mohammad Mozaffari, Walid Saad, Mehdi Bennis, and Mérouane Debbah. Wireless communication using unmanned aerial vehicles (UAVs): Optimal transport theory for hover time optimization. *IEEE Transactions on Wireless Communications*, 16(12):8052–8066, 2017.

[52] Mohammad Mozaffari, Ali Taleb Zadeh Kasgari, Walid Saad, Mehdi Bennis, and Mérouane Debbah. Beyond 5G with UAVs: Foundations of a 3D wireless cellular network. *IEEE Transactions on Wireless Communications*, 18(1):357–372, 2018.

[53] Chen Han, Aijun Liu, Kang An, Gan Zheng, and Xinhai Tong. Distributed UAV Deployment in Hostile Environment: A Game-Theoretic Approach. *IEEE Wireless Communications Letters*, 11(1):126–130, 2021.

[54] Jiaxin Chen, Qihui Wu, Yuhua Xu, Nan Qi, Tao Fang, and DianXiong Liu. Spectrum allocation for task-driven UAV communication networks exploiting game theory. *IEEE Wireless Communications*, 28(4):174–181, 2021.

[55] Mengjie Yi, Xijun Wang, Juan Liu, Yan Zhang, and Bo Bai. Deep reinforcement learning for fresh data collection in UAV-assisted IoT networks. In *IEEE INFOCOM 2020-IEEE Conference on Computer Communications Workshops (INFOCOM WKSHPS)*, pages 716–721. IEEE, 2020.

[56] Xiangjin Zeng, Feipeng Ma, Tingwei Chen, Xuanzhang Chen, and Xijun Wang. Age-optimal UAV trajectory planning for information gathering with energy constraints. In *IEEE/CIC International Conference on Communications in China (ICCC)*, pages 881–886, 2020.

[57] Mengying Sun, Xiaodong Xu, Xiaoqi Qin, and Ping Zhang. AoI-energy-aware UAV-assisted data collection for IoT networks: A deep reinforcement learning method. *IEEE Internet of Things Journal*, 8(24):17275–17289, 2021.

[58] Cheng Zhan, Han Hu, Xiufeng Sui, Zhi Liu, and Dusit Niyato. Completion time and energy optimization in the UAV-enabled mobile-edge computing system. *IEEE Internet of Things Journal*, 7(8):7808–7822, 2020.

[59] Oussama Ghdiri, Wael Jaafar, Safwan Alfattani, Jihene Ben Abderrazak, and Halim Yanikomeroglu. Offline and online UAV-enabled data collection in time-constrained IoT networks. *IEEE Transactions on Green Communications and Networking*, 5(4):1918–1933, 2021.

[60] Ye Hu, Mingzhe Chen, Walid Saad, H Vincent Poor, and Shuguang Cui. Meta-reinforcement learning for trajectory design in wireless UAV networks. In *IEEE Global Communications Conference (Globecom)*, pages 1–6, 2020.

[61] Ali Murat Demirtas, Mehmet Saygin Seyfioglu, Irem Bor-Yaliniz, Bulent Tavli, and Halim Yanikomeroglu. Deep Learning Based Autonomous UAV-BSs for NGWNs: Overview and A Novel Architecture. *IEEE Consumer Electronics Magazine*, 2022.

[62] Yining Wang, Mingzhe Chen, Zhaohui Yang, Tao Luo, and Walid Saad. Deep learning for optimal deployment of UAVs with visible light communications. *IEEE transactions on wireless communications*, 19(11):7049–7063, 2020.

[63] Mingzhe Chen, Walid Saad, and Changchuan Yin. Liquid state machine learning for resource and cache management in LTE-U unmanned aerial vehicle (UAV) networks. *IEEE Transactions on Wireless Communications*, 18(3):1504–1517, 2019.

[64] Yi Liu, Shengli Xie, and Yan Zhang. Cooperative offloading and resource management for UAV-enabled mobile edge computing in power IoT system. *IEEE Transactions on Vehicular Technology*, 69(10):12229–12239, 2020.

[65] Haixia Peng and Xuemin Shen. Multi-agent reinforcement learning based resource management in MEC-and UAV-assisted vehicular networks. *IEEE Journal on Selected Areas in Communications*, 39(1):131–141, 2020.

[66] Kai Li, Wei Ni, Eduardo Tovar, and Abbas Jamalipour. Deep Q-learning based resource management in UAV-assisted wireless powered IoT networks. In *IEEE International Conference on Communications (ICC)*, pages 1–6, 2020.

[67] LLC Gurobi Optimization. Gurobi optimizer reference manual. Retrieved from http://www.gurobi.com, 2021.

[68] Qiang Liu, Honggang Wang, Yantao Sun, and Tingting Han. A Multi-UAVs communication network simulation platform using OPNET modeler. In *IEEE International Conference on Communications (ICC)*, pages 1–6, 2020.

[69] Nan Cheng, Wei Quan, Weisen Shi, Huaqing Wu, Qiang Ye, Haibo Zhou, Weihua Zhuang, Xuemin Shen, and Bo Bai. A comprehensive simulation platform for space-air-ground integrated network. *IEEE Wireless Communications*, 27(1):178–185, 2020.

[70] Gareth J Nunns, Yu-Jia Chen, Deng-Kai Chang, Kai-Min Liao, Fung Po Tso, and Lin Cui. Autonomous flying WiFi access point. In *IEEE Symposium on Computers and Communications (ISCC)*, pages 278–283, 2019.

[71] Bertold Van der Bergh, Alessandro Chiumento, and Sofie Pollin. LTE in the sky: Trading off propagation benefits with interference costs for aerial nodes. *IEEE Communications Magazine*, 54(5):44–50, 2016.

[72] Sathyanarayanan Chandrasekharan, Karina Gomez, Akram Al-Hourani, Sithamparanathan Kandeepan, Tinku Rasheed, Leonardo Goratti, Laurent Reynaud, David Grace, Isabelle Bucaille, Thomas Wirth, et al. Designing and implementing future aerial communication networks. *IEEE Communications Magazine*, 54(5):26–34, 2016.

[73] Rajeev Gangula, Omid Esrafilian, David Gesbert, Cedric Roux, Florian Kaltenberger, and Raymond Knopp. Flying rebots: First results on an autonomous UAV-based LTE relay using open airinterface. In *IEEE 19th International Workshop on Signal Processing Advances in Wireless Communications (SPAWC)*, pages 1–5, 2018.

[74] Weisi Guo, Conor Devine, and Siyi Wang. Performance analysis of micro unmanned airborne communication relays for cellular networks. In *International symposium on communication systems, networks & digital sign (CSNDSP)*, pages 658–663, 2014.

[75] Xiaokang Ye, Xuesong Cai, Xuefeng Yin, José Rodríguez-Piñeiro, Li Tian, and Jianwu Dou. Air-to-ground big-data-assisted channel modeling based on passive sounding in LTE networks. In *IEEE Globecom Workshops (GC Wkshps)*, pages 1–6, 2017.

[76] Wahab Khawaja, Ozgur Ozdemir, and Ismail Guvenc. UAV air-to-ground channel characterization for mmWave systems. In *IEEE 86th Vehicular Technology Conference (VTC-Fall)*, pages 1–5, 2017.

[77] Tricia J Willink, Chris C Squires, Geoffrey WK Colman, and Michael T Muccio. Measurement and characterization of low-altitude air-to-ground MIMO channels. *IEEE Transactions on Vehicular Technology*, 65(4):2637–2648, 2015.

[78] Rafhael Amorim, Huan Nguyen, Jeroen Wigard, István Z Kovács, Troels B Sorensen, and Preben Mogensen. LTE radio measurements above urban

rooftops for aerial communications. In *IEEE Wireless Communications and Networking Conference (WCNC)*, pages 1–6, 2018.

[79] Tianyu Liu, Zaichen Zhang, Hao Jiang, Yurong Qian, Kailin Liu, Jian Dang, and Liang Wu. Measurement-based characterization and modeling for low-altitude UAV air-to-air channels. *IEEE Access*, 7:98832–98840, 2019.

[80] Ning Gao, Yong Zeng, Jian Wang, Di Wu, Chaoyue Zhang, Qingheng Song, Jachen Qian, and Shi Jin. Energy model for UAV communications: Experimental validation and model generalization. *China Communications*, 18(7):253–264, 2021.

[81] Yongs Zeng, Qingqing Wu, and Rui Zhang. Accessing from the sky: A tutorial on UAV communications for 5G and beyond. *Proceedings of the IEEE*, 107(12):2327–2375, 2019.

[82] Mohammad Mozaffari, Walid Saad, Mehdi Bennis, Young-Han Nam, and Mérouane Debbah. A tutorial on UAVs for wireless networks: Applications, challenges, and open problems. *IEEE communications surveys & tutorials*, 21(3):2334–2360, 2019.

[83] Xianbin Cao, Peng Yang, Mohamed Alzenad, Xing Xi, Dapeng Wu, and Halim Yanikomeroglu. Airborne communication networks: A survey. *IEEE Journal on Selected Areas in Communications*, 36(9):1907–1926, 2018.

[84] Laurence A Wolsey and George L Nemhauser. *Integer and combinatorial optimization*, volume 55. John Wiley & Sons, 1999.

[85] David G Luenberger, Yinyu Ye, et al. *Linear and nonlinear programming*, volume 2. Springer, 1984.

[86] Marshall L Fisher. The Lagrangian relaxation method for solving integer programming problems. *Management science*, 27(1):1–18, 1981.

[87] Jean-Louis Goffin. On convergence rates of subgradient optimization methods. *Mathematical programming*, 13(1):329–347, 1977.

[88] Ahmed Ibrahim, Octavia A Dobre, Telex MN Ngatched, and Ana Garcia Armada. Bender's Decomposition for Optimization Design Problems in Communication Networks. *IEEE Network*, 34(3):232–239, 2019.

[89] J BnnoBRs. Partitioning procedures for solving mixed-variables programming problems. *Numerische mathematik*, 4(1):238–252, 1962.

[90] Roy D Yates, Yin Sun, D Richard Brown, Sanjit K Kaul, Eytan Modiano, and Sennur Ulukus. Age of information: An introduction and survey. *IEEE Journal on Selected Areas in Communications*, 39(5):1183–1210, 2021.

[91] Chixiong Mao, Juan Liu, and Lingfu Xie. Multi-UAV aided data collection for age minimization in wireless sensor networks. In *2020 International Conference on Wireless Communications and Signal Processing (WCSP)*, pages 80–85, 2020.

[92] Jingjing Wang, Chunxiao Jiang, Zhu Han, Yong Ren, Robert G Maunder, and Lajos Hanzo. Taking drones to the next level: Cooperative distributed unmanned-aerial-vehicular networks for small and mini drones. *IEEE Vehicular Technology Magazine*, 12(3):73–82, 2017.

[93] Mohamed A Abd-Elmagid and Harpreet S Dhillon. Average peak age-of-information minimization in UAV-assisted IoT networks. *IEEE Transactions on Vehicular Technology*, 68(2):2003–2008, 2018.

[94] Mohamed A Abd-Elmagid, Aidin Ferdowsi, Harpreet S Dhillon, and Walid Saad. Deep reinforcement learning for minimizing age-of-information in UAV-assisted networks. In *IEEE Global Communications Conference (GLOBECOM)*, pages 1–6, 2019.

[95] Shuhang Zhang, Hongliang Zhang, Zhu Han, H Vincent Poor, and Lingyang Song. Age of information in a cellular Internet of UAVs: Sensing and communication trade-off design. *IEEE Transactions on Wireless Communications*, 19(10):6578–6592, 2020.

[96] Mohamed Alzenad, Amr El-Keyi, Faraj Lagum, and Halim Yanikomeroglu. 3-D placement of an unmanned aerial vehicle base station (UAV-BS) for energy-efficient maximal coverage. *IEEE Wireless Communications Letters*, 6(4):434–437, 2017.

[97] Dingcheng Yang, Qingqing Wu, Yong Zeng, and Rui Zhang. Energy tradeoff in ground-to-UAV communication via trajectory design. *IEEE Transactions on Vehicular Technology*, 67(7):6721–6726, 2018.

[98] 3GPP. Study on enhanced LTE support for aerial vehicles. *Technical report (TR) 36.777, 3rd Generation Partnership Project (3GPP)*, V15.0.0, 2017.

[99] Andrea Goldsmith. *Wireless communications*. Cambridge university press, 2005.

[100] Bezalel Gavish and Stephen C Graves. The travelling salesman problem and related problems. 1978.

[101] Antonio López Jaimes, Saúl Zapotecas Martınez, and Carlos A Coello Coello. An introduction to multiobjective optimization techniques. *Optimization in Polymer Processing*, pages 29–57, 2009.

[102] Jingjing Wang, Chunxiao Jiang, Haijun Zhang, Yong Ren, Kwang-Cheng Chen, and Lajos Hanzo. Thirty years of machine learning: The road to Pareto-optimal wireless networks. *IEEE Communications Surveys & Tutorials*, 22(3):1472–1514, 2020.

[103] Thomas L Saaty. A scaling method for priorities in hierarchical structures. *Journal of mathematical psychology*, 15(3):234–281, 1977.

[104] R Timothy Marler and Jasbir S Arora. The weighted sum method for multi-objective optimization: new insights. *Structural and multidisciplinary optimization*, 41:853–862, 2010.

[105] Michael Grant and Stephen Boyd. CVX: Matlab software for disciplined convex programming, version 2.1. Retrieved from http://cvxr.com/cvx, March 2014.

[106] Chiranjib Saha, Mehrnaz Afshang, and Harpreet S Dhillon. 3GPP-inspired HetNet model using Poisson cluster process: Sum-product functionals and downlink coverage. *IEEE Transactions on Communications*, 66(5):2219–2234, 2017.

[107] Vasilis Friderikos. Airborne urban microcells with grasping end effectors: A game changer for 6G networks? In *2021 IEEE International Mediterranean Conference on Communications and Networking (MeditCom)*, pages 336–341. IEEE, 2021.

[108] Xu Liu, Yuqing He, Bo Chen, Yongqiang Hou, Kaiyuan Bi, and Decai Li. A vision-based unmanned aircraft system for autonomous grasp & transport. In *International Conference on Unmanned Aircraft Systems (ICUAS)*, pages 1186–1193. IEEE, 2019.

[109] Mohamed Alzenad, Muhammad Z Shakir, Halim Yanikomeroglu, and Mohamed-Slim Alouini. FSO-based vertical backhaul/fronthaul framework for 5G+ wireless networks. *IEEE Communications Magazine*, 56(1):218–224, 2018.

[110] Mohamed-Amine Lahmeri, Mustafa A Kishk, and Mohamed-Slim Alouini. Charging techniques for UAV-assisted data collection: Is laser power beaming the answer? *IEEE Communications Magazine*, 60(5):50–56, 2022.

[111] Mohamed-Amine Lahmeri, Mustafa A Kishk, and Mohamed-Slim Alouini. Laser-powered UAVs for wireless communication coverage: A large-scale deployment strategy. *IEEE Transactions on Wireless Communications*, 22(1):518–533, 2022.

[112] Mustafa Kishk, Ahmed Bader, and Mohamed-Slim Alouini. Aerial base station deployment in 6G cellular networks using tethered drones: The mobility and endurance tradeoff. *IEEE Vehicular Technology Magazine*, 15(4):103–111, 2020.

[113] Baohua Zhang, Yuanxin Xie, Jun Zhou, Kai Wang, and Zhen Zhang. State-of-the-art robotic grippers, grasping and control strategies, as well as their applications in agricultural robots: A review. *Computers and Electronics in Agriculture*, 177:105694, 2020.

[114] Yunchou Xing and Theodore S Rappaport. Millimeter wave and terahertz urban microcell propagation measurements and models. *IEEE Communications Letters*, 25(12):3755–3759, 2021.

[115] Robert J Kerczewski, Jeffrey D Wilson, and William D Bishop. Frequency spectrum for integration of unmanned aircraft. In *2013 IEEE/AIAA 32nd Digital Avionics Systems Conference (DASC)*, pages 6D5–1. IEEE, 2013.

[116] Fengli Xu, Yong Li, Huandong Wang, Pengyu Zhang, and Depeng Jin. Understanding mobile traffic patterns of large scale cellular towers in urban environment. *IEEE/ACM Transactions on Networking*, 25(2):1147–1161, 2016.

[117] Ashwin Suresh Nedungadi and Martin Saska. Design of an active-reliable grasping mechanism for autonomous unmanned aerial vehicles. In *Modelling and Simulation for Autonomous Systems: 6th International Conference*, pages 162–179. Springer, 2020.

[118] Gunther Auer, Vito Giannini, Claude Desset, Istvan Godor, Per Skillermark, Magnus Olsson, Muhammad Ali Imran, Dario Sabella, Manuel J Gonzalez, Oliver Blume, et al. How much energy is needed to run a wireless network? *IEEE Wireless Communcation*, 18(5):40–49, 2011.

[119] W Nathan Alexander and Jeremiah Whelchel. Flyover Noise of multi-rotor sUAS. In *Inter-Noise and Noise-Con Congress and Conference Proceedings*, volume 259, pages 2548–2558. Institute of Noise Control Engineering, 2019.

[120] S Abeta. 3GPP TR 36.814: Further advancements for E-UTRA physical layer aspects. *the 3rd Generation Partnership Project (3GPP)*, 2017.

[121] Yuan Liao and Vasilis Friderikos. Max-min rate deployment optimization for backhaul-limited robotic aerial 6G small cells. In *IEEE global communications conference (GLOBECOM)*, pages 2963–2968, 2022.

[122] Boris Galkin, Jacek Kibilda, and Luiz A DaSilva. UAVs as mobile infrastructure: Addressing battery lifetime. *IEEE Communications Magazine*, 57(6):132–137, 2019.

[123] Haijie Zhang, Elisha Lerner, Bo Cheng, and Jianguo Zhao. Compliant bistable grippers enable passive perching for micro aerial vehicles. *IEEE/ASME Transactions on Mechatronics*, 26(5):2316–2326, 2020.

[124] Jingjin Wu, Yujing Zhang, Moshe Zukerman, and Edward Kai-Ning Yung. Energy-efficient base-stations sleep-mode techniques in green cellular networks: A survey. *IEEE communications surveys & tutorials*, 17(2):803–826, 2015.

[125] Imran Ashraf, Federico Boccardi, and Lester Ho. Sleep mode techniques for small cell deployments. *IEEE Communications Magazine*, 49(8):72–79, 2011.

[126] Chang Liu, Balasubramaniam Natarajan, and Hongxing Xia. Small cell base station sleep strategies for energy efficiency. *IEEE Transactions on Vehicular Technology*, 65(3):1652–1661, 2015.

[127] Louai Saker, Salah-Eddine Elayoubi, Richard Combes, and Tijani Chahed. Optimal control of wake up mechanisms of femtocells in heterogeneous networks. *IEEE Journal on Selected Areas in Communications*, 30(3):664–672, 2012.

[128] Shijie Cai, Limin Xiao, Haibin Yang, Jing Wang, and Shidong Zhou. A cross-layer optimization of the joint macro-and picocell deployment with sleep mode for green communications. In *2013 22nd Wireless and Optical Communication Conference*, pages 225–230. IEEE, 2013.

[129] Junhong Ye and Ying-Jun Angela Zhang. DRAG: Deep reinforcement learning based base station activation in heterogeneous networks. *IEEE Transactions on Mobile Computing*, 19(9):2076–2087, 2019.

[130] Binnan Zhuang, Dongning Guo, and Michael L Honig. Energy-efficient cell activation, user association, and spectrum allocation in heterogeneous networks. *IEEE Journal on Selected Areas in Communications*, 34(4):823–831, 2016.

[131] Kaiming Shen, Ya-Feng Liu, David Yiwei Ding, and Wei Yu. Flexible multiple base station association and activation for downlink heterogeneous networks. *IEEE Signal Processing Letters*, 24(10):1498–1502, 2017.

[132] Junyao Guo, Yineng Chen, Jinkang Zhu, and Sihai Zhang. Can We Achieve Better Wireless Traffic Prediction Accuracy? *IEEE Communications Magazine*, 59(8):58–63, 2021.

[133] Shuo Wang, Xing Zhang, Jiaxin Zhang, Jian Feng, Wenbo Wang, and Ke Xin. An approach for spatial-temporal traffic modeling in mobile cellular networks. In *2015 27th International Teletraffic Congress*, pages 203–209. IEEE, 2015.

[134] Catherine Forbes, Merran Evans, Nicholas Hastings, and Brian Peacock. *Statistical distributions*. John Wiley & Sons, 2011.

[135] Mikhail A Bragin, Peter B Luh, Joseph H Yan, Nanpeng Yu, and Gary A Stern. Convergence of the surrogate Lagrangian relaxation method. *Journal of Optimization Theory and applications*, 164(1):173–201, 2015.

[136] Aharon Ben-Tal and Arkadi Nemirovski. *Lectures on modern convex optimization: analysis, algorithms, and engineering applications*. SIAM, 2001.

[137] Philip Hall. On representatives of subsets. *Classic Papers in Combinatorics*, pages 58–62, 1987.

[138] Harold W Kuhn. The Hungarian method for the assignment problem. *Naval research logistics quarterly*, 2(1-2):83–97, 1955.

[139] Nguyen Cong Luong, Xiao Lu, Dinh Thai Hoang, Dusit Niyato, and Dong In Kim. Radio resource management in joint radar and communication: A comprehensive survey. *IEEE Communications Surveys & Tutorials*, 23(2):780–814, 2021.

[140] Yongjun Liu, Guisheng Liao, Jingwei Xu, Zhiwei Yang, and Yuhong Zhang. Adaptive OFDM integrated radar and communications waveform design based on information theory. *IEEE Communications Letters*, 21(10):2174–2177, 2017.

[141] Yongjun Liu, Guisheng Liao, and Zhiwei Yang. Robust OFDM integrated radar and communications waveform design based on information theory. *Signal Processing*, 162:317–329, 2019.

[142] Chenguang Shi, Fei Wang, Sana Salous, and Jianjiang Zhou. Low probability of intercept-based optimal OFDM waveform design strategy for an integrated radar and communications system. *IEEE Access*, 6:57689–57699, 2018.

[143] Chenguang Shi, Fei Wang, Sana Salous, and Jianjiang Zhou. Joint subcarrier assignment and power allocation strategy for integrated radar and communications system based on power minimization. *IEEE Sensors Journal*, 19(23):11167–11179, 2019.

[144] Huy T Nguyen, Dinh Thai Hoang, Nguyen Cong Luong, Dusit Niyato, and Dong In Kim. A hierarchical game model for OFDM integrated radar and communication systems. *IEEE Transactions on Vehicular Technology*, 70(5):5077–5082, 2021.

[145] Yanpeng Cui, Zhiyong Feng, Qixun Zhang, Zhiqing Wei, Chenlong Xu, and Ping Zhang. Toward trusted and swift UAV communication: ISAC-Enabled dual identity mapping. *IEEE Wireless Communications*, 30(1):58–66, 2023.

[146] K. Meng *et al.* UAV trajectory and beamforming optimization for integrated periodic sensing and communication. *IEEE Wireless Communications Letters*, 11(6):1211–1215, 2022.

[147] Yunhui Qin, Zhongshan Zhang, Xulong Li, Wei Huangfu, and Haijun Zhang. Deep reinforcement learning based resource allocation and trajectory planning in integrated sensing and communications UAV network. *IEEE Transactions on Wireless Communications*, pages 1–1, 2023.

[148] Abbas Hatoum, Rami Langar, Nadjib Aitsaadi, Raouf Boutaba, and Guy Pujolle. Cluster-based resource management in OFDMA femtocell networks with QoS guarantees. *IEEE Transactions on Vehicular Technology*, 63(5):2378–2391, 2013.

[149] Mate Boban, Apostolos Kousaridas, Konstantinos Manolakis, Josef Eichinger, and Wen Xu. Connected roads of the future: Use cases, requirements, and design considerations for vehicle-to-everything communications. *IEEE vehicular technology magazine*, 13(3):110–123, 2018.

[150] Dongheon Lee, Sheng Zhou, Xiaofeng Zhong, Zhisheng Niu, Xuan Zhou, and Honggang Zhang. Spatial modeling of the traffic density in cellular networks. *IEEE Wireless Communications*, 21(1):80–88, 2014.

[151] Christian Sturm, Thomas Zwick, and Werner Wiesbeck. An OFDM system concept for joint radar and communications operations. In *VTC Spring 2009-IEEE 69th Vehicular Technology Conference*, pages 1–5. IEEE, 2009.

[152] Xuanxuan Tian and Zhaohui Song. On radar and communication integrated system using OFDM signal. In *2017 IEEE Radar Conference (RadarConf)*, pages 0318–0323. IEEE, 2017.

[153] Yibo Zhang, Jingjing Wang, Lanjie Zhang, Yufang Zhang, Qi Li, and Kwang-Cheng Chen. Reliable transmission for NOMA systems with randomly deployed receivers. *IEEE Transactions on Wireless Communications*, 71(2):1179–1192, 2023.

[154] Dimitris Bertsimas and Melvyn Sim. The price of robustness. *Operation Research*, 52(1):35–53, 2004.

[155] Wei-Kun Chen, Ya-Feng Liu, Fan Liu, Yu-Hong Dai, and Zhi-Quan Luo. Towards efficient large-scale network slicing: An LP dynamic rounding-and-refinement approach. *IEEE Transactions on Signal Processing*, 71:615–630, 2023.

[156] Jialu Lun, David Grace, Alister Burr, Yunbo Han, Kari Leppanen, and Tao Cai. Millimetre wave backhaul/fronthaul deployments for ultra-dense outdoor small cells. In *IEEE Wireless Communications and Networking Conference Workshops (WCNCW)*, pages 187–192, 2016.

[157] Nima Palizban, Sebastian Szyszkowicz, and Halim Yanikomeroglu. Automation of millimeter wave network planning for outdoor coverage in dense urban areas using wall-mounted base stations. *IEEE Wireless Communation Letters*, 6(2):206–209, 2017.

[158] Wenjuan Pu, Xiaohui Li, Jiangwei Yuan, and Xu Yang. Traffic-oriented resource allocation for mmWave multi-hop backhaul networks. *IEEE Communications Letters*, 22(11):2330–2333, 2018.

[159] Omid Semiari, Walid Saad, Mehdi Bennis, and Zaher Dawy. Inter-operator resource management for millimeter wave multi-hop backhaul networks. *IEEE Transactions on Wireless Communications*, 16(8):5258–5272, 2017.

[160] Jasmina McMenamy, Adam Narbudowicz, Kyriaki Niotaki, and Irene Macaluso. Hop-constrained mmwave backhaul: Maximising the network flow. *IEEE Wireless Communation Letters*, 9(5):596–600, 2019.

[161] Yong Niu, Weiguang Ding, Hao Wu, Yong Li, Xinlei Chen, Bo Ai, and Zhangdui Zhong. Relay-assisted and QoS aware scheduling to overcome blockage in mmWave backhaul networks. *IEEE transactions on vehicular technology*, 68(2):1733–1744, 2019.

[162] Margarita Gapeyenko, Vitaly Petrov, Dmitri Moltchanov, Sergey Andreev, Nageen Himayat, and Yevgeni Koucheryavy. Flexible and reliable UAV-assisted backhaul operation in 5G mmWave cellular networks. *IEEE Journal on Selected Areas in Communications*, 36(11):2486–2496, 2018.

[163] Ursula Challita and Walid Saad. Network formation in the sky: Unmanned aerial vehicles for multi-hop wireless backhauling. In *IEEE global communications conference (GLOBECOM)*, pages 1–6, 2017.

[164] Chen Qiu, Zhiqing Wei, Zhiyong Feng, and Ping Zhang. Joint resource allocation, placement and user association of multiple UAV-mounted base stations with in-band wireless backhaul. *IEEE Wireless Communications Letters*, 8(6):1575–1578, 2019.

[165] Changsheng You and Rui Zhang. Hybrid offline-online design for UAV-enabled data harvesting in probabilistic LoS channels. *IEEE Transactions on Wireless Communications*, 19(6):3753–3768, 2020.

[166] Changsheng You, Xiaoming Peng, and Rui Zhang. 3D trajectory design for UAV-enabled data harvesting in probabilistic LoS channel. In *2019 IEEE Global Communications Conference (GLOBECOM)*, pages 1–6. IEEE, 2019.

[167] 3GPP. Study on channel model for frequencies from 0.5 to 100 GHz, 2018.

[168] Fengqi You, Pedro M Castro, and Ignacio E Grossmann. Dinkelbach's algorithm as an efficient method to solve a class of MINLP models for large-scale cyclic scheduling problems. *Computers & Chemical Engineering*, 33(11):1879–1889, 2009.

[169] Marco E Lübbecke and Jacques Desrosiers. Selected topics in column generation. *Operations research*, 53(6):1007–1023, 2005.

[170] Thomas H Cormen, Charles E Leiserson, Ronald L Rivest, and Clifford Stein. *Introduction to Algorithms*. MIT Press, 2022.

[171] CAA. The UK Civil Aviation Authority, The Drone and Model Aircraft Code. Retrieved from https://register-drones.caa.co.uk/drone-code/where-you-can-fly, 2022.

[172] Ofcom. Ofcom, Consultation: Spectrum for Unmanned Aircraft Systems (UAS). Retrieved from www.ofcom.org.uk/consultations-and-statements/category-1/spectrum-for-unmanned-aircraft-systems, 2022.

[173] Antonio Filippone. *Flight performance of fixed and rotary wing aircraft*. Elsevier, 2006.

[174] Anthony Robert Southey Bramwell, David Balmford, and George Done. *Bramwell's helicopter dynamics*. Elsevier, 2001.

[175] Mark R Bell. Information theory and radar waveform design. *IEEE Transactions on Information Theory*, 39(5):1578–1597, 1993.

[176] Upamanyu Madhow. *Fundamentals of digital communication*. Cambridge university press, 2008.